Title
Biologically-inspired Microfluidic Platforms and Aptamer-based Nanobiosensors

Author
Cho, Hansang

Publication Date
2010

Biologically-inspired Microfluidic Platforms and Aptamer-based Nanobiosensors

by

Hansang Cho

A dissertation submitted in partial satisfaction of the

requirements for the degree of

Joint Doctor of Philosophy

with University of California, San Francisco

in

Bioengineering

in the

Graduate Division

of the

University of California, Berkeley

Committee in charge:

Professor Luke P. Lee, Chair

Professor Dorian Liepmann

Professor Ming C. Wu

Professor John Kurhanewicz

Fall 2010

Biologically-inspired Microfluidic Platforms and Aptamer-based Nanobiosensors

Hansang Cho

Abstract

Biologically-inspired Microfluidic Platforms and Aptamer-based Nanobiosensors

by

Hansang Cho

Joint Doctor of Philosophy in Bioengineering with

University of California, San Francisco

University of California, Berkeley

Professor Luke P. Lee, Chair

Recent advances in micro/nano- technologies have shown high potentials in the field of quantitative biology, biomedical science, and analytical chemistry. However, micro/nano fluidics still requires multi-layered structures, complex plumbing/tubing, and external equipments for large-scale applications and nanotechnology-based sensors demand high cost. Interestingly, nature has much simpler and more effective solutions. The goal of this dissertation is to develop novel microfluidic platforms and nanobiosensors inspired by biological systems.

In this dissertation, I report the development of a biologically inspired bidirectional fluidic diode motivated by the xylem pores, which allows designing a functional large-scale microfluidic circuit and autonomous fluidic controls without any delegate efforts on fluid regulation. The biologically inspired bidirectional fluidic diode requires only a single-layered structure and a single pressure source to regulate flow in both directions through the entire platform. The operational conditions are precisely estimated based on the fully developed analytical model, which considers the hysteresis of contact angles and effects of fabrication limitations. To demonstrate its many possible applications, I show large-scale, spontaneous droplet-patterning and colonized cell-patterning programmed with the uni- and bi-directional fluidic diodes in the microfludic platform. In addition, inspired by target recognition in nature, an aptamer-based nanoplasmonic sensor, 'aptasensor' is presented by detecting a coagulation protein, human α-thrombin. Also, I present an aptasensor targeting vascular endothelial growth factor-165 (VEGF_{165}), a predominant and effective cancer biomarker for the diagnostics of various solid cancers. The integration of an aptasensor into a microfluidic platform is demonstrated by applying the VEGF_{165} aptasensor to detect secreted VEGF_{165} from breast cancer cells cultured in a microfluidic platform.

I envision that elucidation of mechanisms underlying in biological systems will inspire to create new technologies for the application to precision biology, biotechnology, and medicine. Furthermore, the developed biologically inspired engineering will provide physical insights, analytical models, and useful tools for the better understanding of biological systems.

For my father, who is my lifelong advisor
For my mother, who teaches me patience
For my wife, who gives me endless love and support
For my daughter, who gives us smiles

Table of Contents

Acknowledgements

Among many people whom I would like to thank for their significant roles during my PhD course, I want to thank my wife for offering amazing amounts of support. She supported me as a loving wife, patient mom, diligent housewife as well as my close friend. Without her, I couldn't overcome the most challenging period in my life.

I deeply appreciate my parents, who have showed consistent love and supported me. They are my hometown itself where I can rely. My daughter gave me smiles whenever I was exhausted. Also my aunt, sister and her husband cheered me up.

I want to appreciate my academic advisor, Prof. Luke P. Lee. He showed his impressive mission to research and life and advised me to challenge research strongly along with other committee members, Prof. Dorian Liepmann, Prof. Ming C. Wu, and Prof. John Kurhanewicz. I'd also like to thank Dr. Steve Lane who gave me a warm advice like my grandfather, Prof. Raghu Shinha who advised me like my elder brother, Dr. Jane Bearinger who guided me like my elder sister as well as Dr. Ted Laurence and Dr. Brian Baker who always trusted me. I'd also like to thank Dr. Sebastian Wachsmann-Hogiu and Dr. Cynthia Pagba who showed their kindness.

Thanks to all of my labmates in BioPOETS: Liz Wu, Somin Lee, Yolanda Zhang, David Breslauer, John Waldeisen, Eric Lee, Megan Dueck, Young-Geun Park, Debkishore Mitra, Frankie Myers, Yeonho Choi, SoonGweon Hong, Brendan Turner. Thanks to all of alumni who have been good models for researches: Dr. Jeonggi Seo, Dr. Gang Liu, Dr. Kihun Jeong, Dr. Jaeyeon Kim, Dr. Sunghoon Kwon, Dr. Dino Di Carlro, and Dr. Michel. Thanks to my undergraduate students whom I worked with: Patrick Horng, Edward Ha, Audrey Kimteng, Brian Lee. Among them, Audrey supported me by following whatever I requested with her sincerness and Brian Lee supported me quietly but steadily.

Thanks to my bible study members: Taksoon Lee, Yeonghwan Chang, Taegweon Jee, and Jeewoong Lee.

Finally, I would like to gratefully acknowledge the financial support of Lawrence Scholar Program fellowship (former SEGREF) from Lawrence Livermore National Laboratory, Intel Inc., the Korea Research Foundation Grant funded by the Korea government (MOEHRD), which allowed me to concentrate on my research and successfully finish my doctoral degree.

CHAPTER 1:
INTRODUCTION

1.1 BIOLOGICALLY INSPIRED ENGINEERING

Background

"Human ingenuity may make various inventions, but it will never devise any inventions more beautiful, nor more simple, nor more to the purpose than Nature does; because in her inventions nothing is wanting and nothing is superfluous… Nothing can be found in nature that is not a part of science." (Leonardo da Vinci).

Compared to a short history of human civilization, nature has experimented for billions of years with the principles of physics, chemistry, biology, mechanics, and material science, scaling from nanometers to hundreds of meters.[1] An enormous pool of effective solutions exists within nature, which has always served as a model for humans to confront challenges and improve their lives through evolutional experiments. Humans have invented and engineered novel devices by mimicking the appearance and functions of nature's creatures by adapting the mechanisms in nature and associating the principles of nature to further improve the capability of their devices.[2-5] Major applications of biologically inspired engineering are grouped into materials, structures, mechanics, actuators, and sensors.

1.1.1 Materials

Biologically inspired materials are considered to be alternative solutions for developing innovative engineering materials: biomaterials and adhesives.[6-9] Through evolution, living creatures have converted common raw materials into highly functional resources for their own purposes, with an attempt to produce the materials in resource- and energy-efficient ways. Furthermore, most of the biological materials are made of non-toxic building blocks, which allows for them to be applied in delicate biological environments. However, it is difficult to produce biomaterials homogeneously at a large scale, as well as consistently, due to the variation that exists among generations or individuals. In contrast, when engineered materials can be produced homogeneously and reproducibly on a large scale, but it is complicated to engineer highly functional and biocompatible materials. Therefore, analyzing biomaterials and understanding the principles of such will provide insight into how to design new materials that have both the benefits of biomaterials and engineered materials.

Photosynthetic 3D memory Photosynthesis is to harvest solar energy and then convert it into chemical resources, which systems rely on for life (Fig. 1.1A). Whereas green plants convert light energy into chemical energy by photon-induced charge separation, Halobacterium halobium relies on bacteriorhodopsin (BR) as a photon-driven proton pump. By utilizing the function of BR,[10] photosynthetic memories were developed to read, write, and erase binary data in volumetric cubes of the protein (Fig. 1.1B). Once the functionalities of the photoactive proteins are further optimized, it is expected to apply for protein-based field-effect transistors, artificial retinas, spatial light modulators, photovoltaic fuel cells, and optical holographic processors.

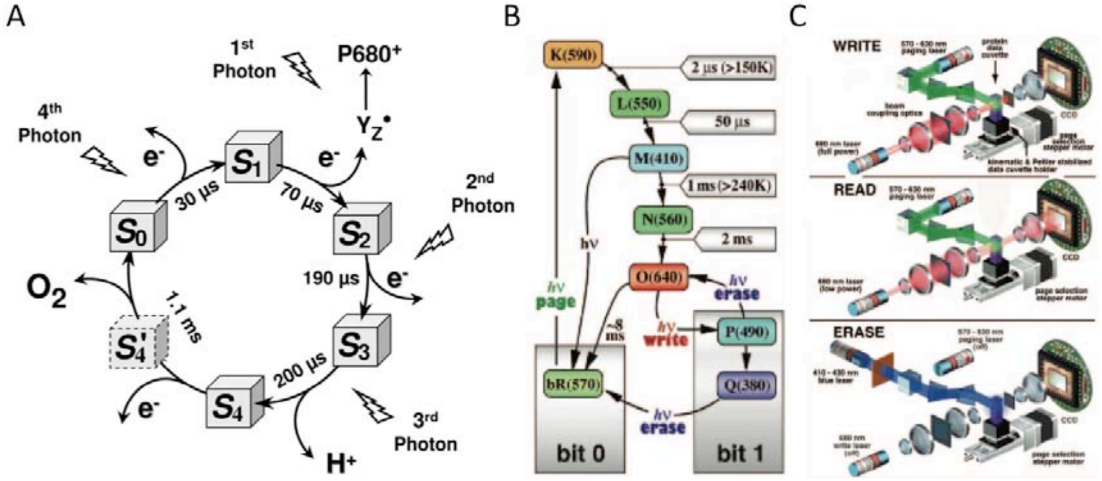

Figure 1.1 Photosynthesis for energy harvesting and memory. (A) Mechanistic model for the formation of photosynthetic oxygen.[11] **(B)** The branched photocycle in BR used for three-dimensional memory device applications (left) and the BR volumetric memory in the operation of 'write', 'read', and 'erase' (right).[10]

Stimuli-Responsive Polymer Nanocomposites Sea cucumbers can change their stiffness promptly with response to the environment. It has been known that cucumbers regulate their stiffness to defend against predators by adjusting the matrix of collagen fibrils (Fig. 1.2A). Inspired by the architecture in sea cucumbers, stimuli-responsive nanocomposite structures were proposed to reinforce a viscoelastic matrix of of fibrillin microfibrils (Fig 1.2B). The matrix made of ethylene oxide–epichlorohydrin 1:1 copolymer (EO-EPI), which has a low modulus and can alter its modulus by the uptake of several chemical stimuli. These "whiskers" provide high stiffness (tensile modulus 143 GPa) at the nanometer scale. In addition to chemical stimulus, EO-EPI/whisker nanocomposites can accommodate nonchemical triggers, such as, optical or electrical stimuli.[12]

Multifunctional coating Mussels have the ability of attachment to virtually all types of inorganic and organic surfaces, including classically adhesion-resistant materials such as poly(tetrafluoroethylene) (PTFE) (Fig. 1.3A).[13] The secret to the attachment capabilities of mussels is amino acid composition proteins, which are abundant in 3,4-dihydroxy-L-phenylalanine (DOPA) and lysine amino acids, providing strong binding force on many substrates. By utilizing the versatile attachment mechanisms found in mussels, a polydopamine modification was utilized to coat various materials such as metal, SAM (self-assembled monolayer), and grafted polymers (Fig. 1.3B). This simple two-step method will provide wide applications including simple ingredients and mild reaction conditions with the applicability to many types of materials of complex shape, and multiple end-uses.

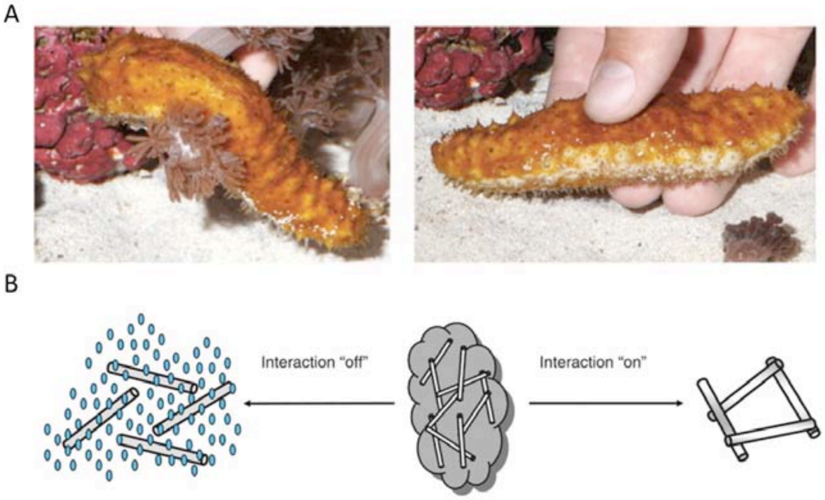

Figure 1.2 See cucumber and stimuli-responsive polymer nanocomposites. (A) Pictures of a sea cucumber in relaxed (left) and stiffened (right) state. **(B)** Schematic representation of the architecture and switching mechanism in the artificial nanocomposites with dynamic mechanical properties corresponding to ‘relaxed’ (left) and ‘stiffened’ state (right).[12]

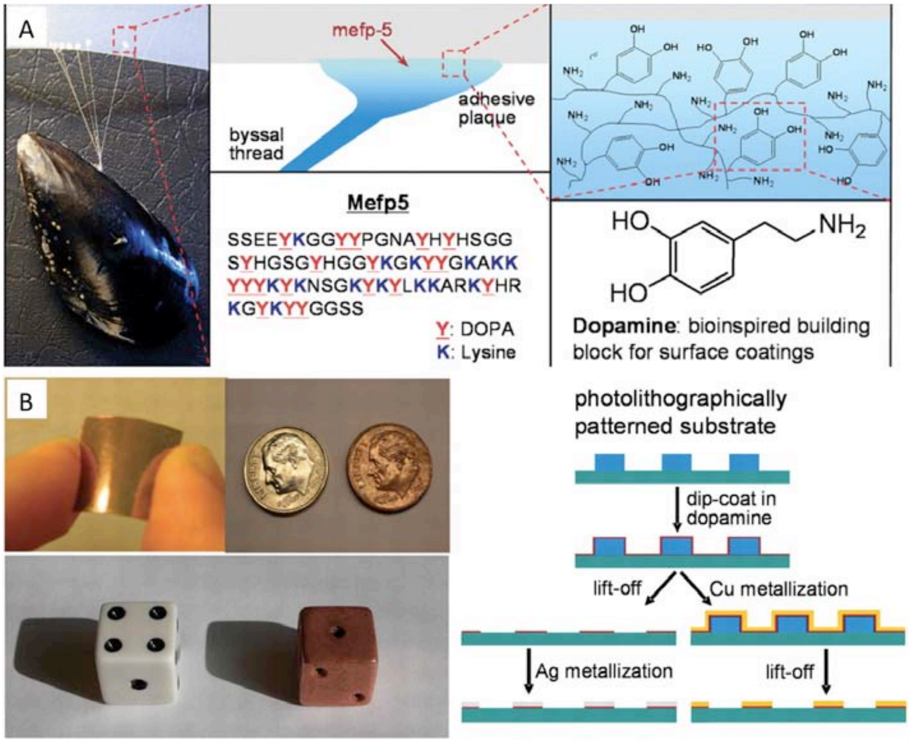

Figure 1.3 Mussel attachment and dopamine coating. (A) Photograph of a mussel attached to commercial PTFE and schematic illustrations of Mefp-5 and a simplified molecular representation of characteristic amine and catechol groups. **(B)** Electroless copper deposition on polydopamine-coated nitrocellulose film, coin, and three-dimensional plastic object.[13]

Super-hydrophopic surface Lotus leaves have nanostructures allowing superhydrophobicity with water contact angles larger than 150° (Fig. 1.4A). Attracted by the mechanism in lotus, various superhydrophobic surfaces were proposed based on nanostructures, solution coating, sol-gel coating, and others. Among them, the porous microsphere/nanofiber composite film (PMNCF) with its structure similar with lotus was prepared from a 7 wt % PS/DMF solution (Fig. 1.4B).[14] The film was covered with numerous microspheres and nanofibers interconnected in a 3D and distributed densely in a large scale. This method is believed to be capable of preparing stable superhydrophobic surfaces on a wide variety of materials.

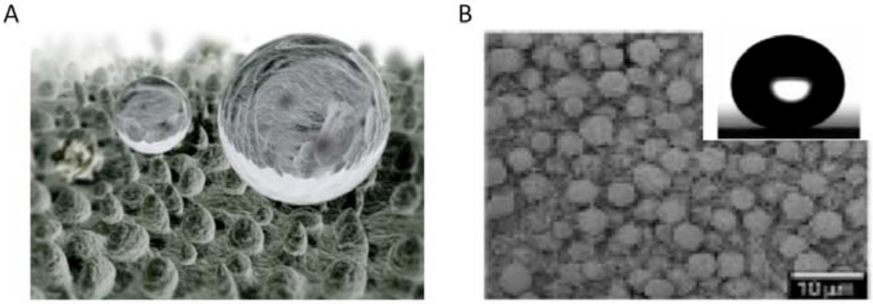

Figure 1.4 Natural and artificial lotus (A) Lotus (http://www.aboutthelotus.com/index.html) **(B)** 3D network structure of PMNCF and water droplet on PMNCF.[14]

Reversible tape A gecko has the capability of climbing on any vertical surfaces and hanging on the ceiling even using a single toe. It has been revealed that gecko induces a strong van der Waals force by countless specialized keratinous aligned microscopic elastic hairs, called setae, splitting into even nanometer-scale spatulae at the end (Fig. 1.5A).[15] From the effort to mimic the nanostructure in a gecko, the strong and reversible tape was developed by fabricating an extraordinary high aspect ratio and exceptional mechanical strength, vertically aligned carbon nanotubes (VA-CNTs, both single-walled and multiwalled), which have the potential for dry adhesive applications (Fig. 1.5B).[16] Carbaon nanotube-based papes would be widely used for firm attachment and relatively weak normal adhesion for easy detachment, which opens many technological applications.

1.1.2 Structures

Photonic structure Many species have evolved structures displaying colouration as a result of diffraction from surface periodicities. The structures are composed of multilayers of alternately high and low refractive index, which induce optical interference. For example, iridescent blue Morpho rhetenor butterflies have photonic structures formed by discrete multilayers of cuticle and air, which have the visibility in a UV range (Fig 1.6A).[17] Inspired by photonic structures in nature, 'M-ink' generated repetitive tuning and fixing of the structures to create structural color at high-resolution. Various multicoloured patterns could be realized by the modulating an external magnetic field modulation and controlling UV exposure spatially (Fig. 1.6B).[18] By utilizing a maskless lithographic technique, the M-ink method is expected to achieve rapid and multilayered patterning.

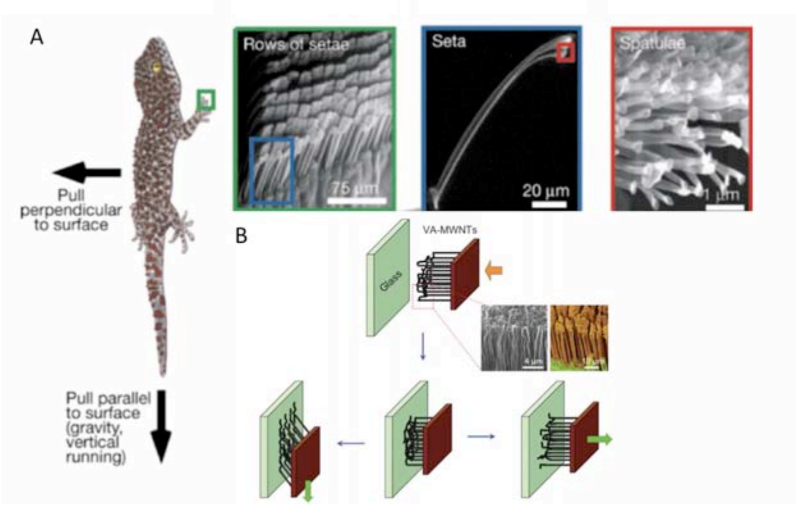

Figure 1.5 Dry adhesive of gecko and VA-MWNT. (A) Gecko setae and apparatus for force measurement.[15] **(B)** Schematic diagrams for the morphological change of VA-MWNT arrays during adhesion measurement.[16]

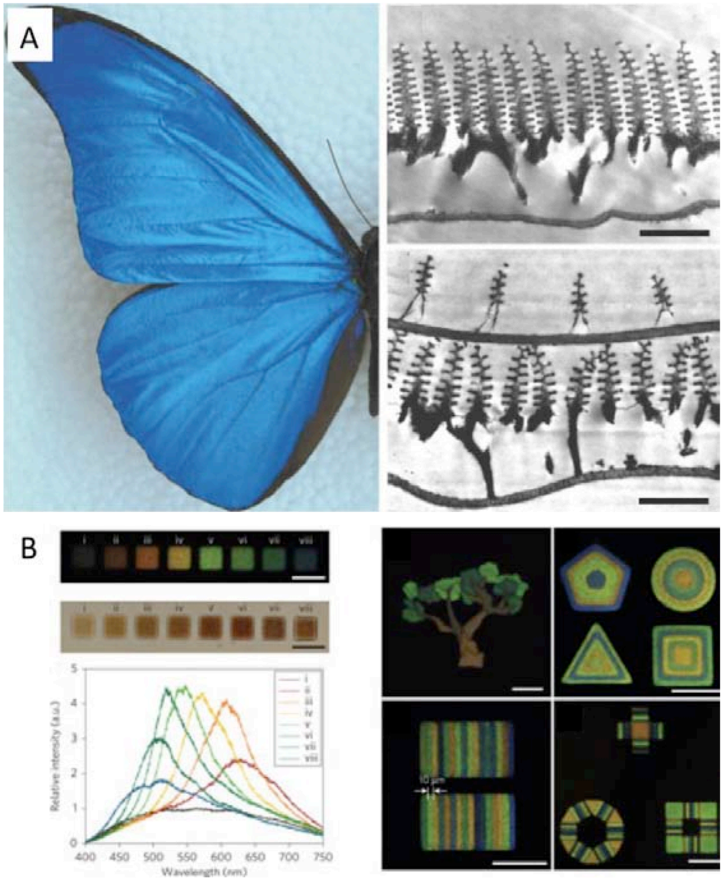

Figure 1.6 Honeycomb as a Strong, Lightweight Structure (A) Real colour image of the blue iridescence from a M. rhetenor wing (left) and transmission electron micrograph (TEM) images showing wing-scale cross-sections of M. rhetenor (right).[17] **(B)** Generation of high-resolution multiple structural colour patterns using M-Ink.[18]

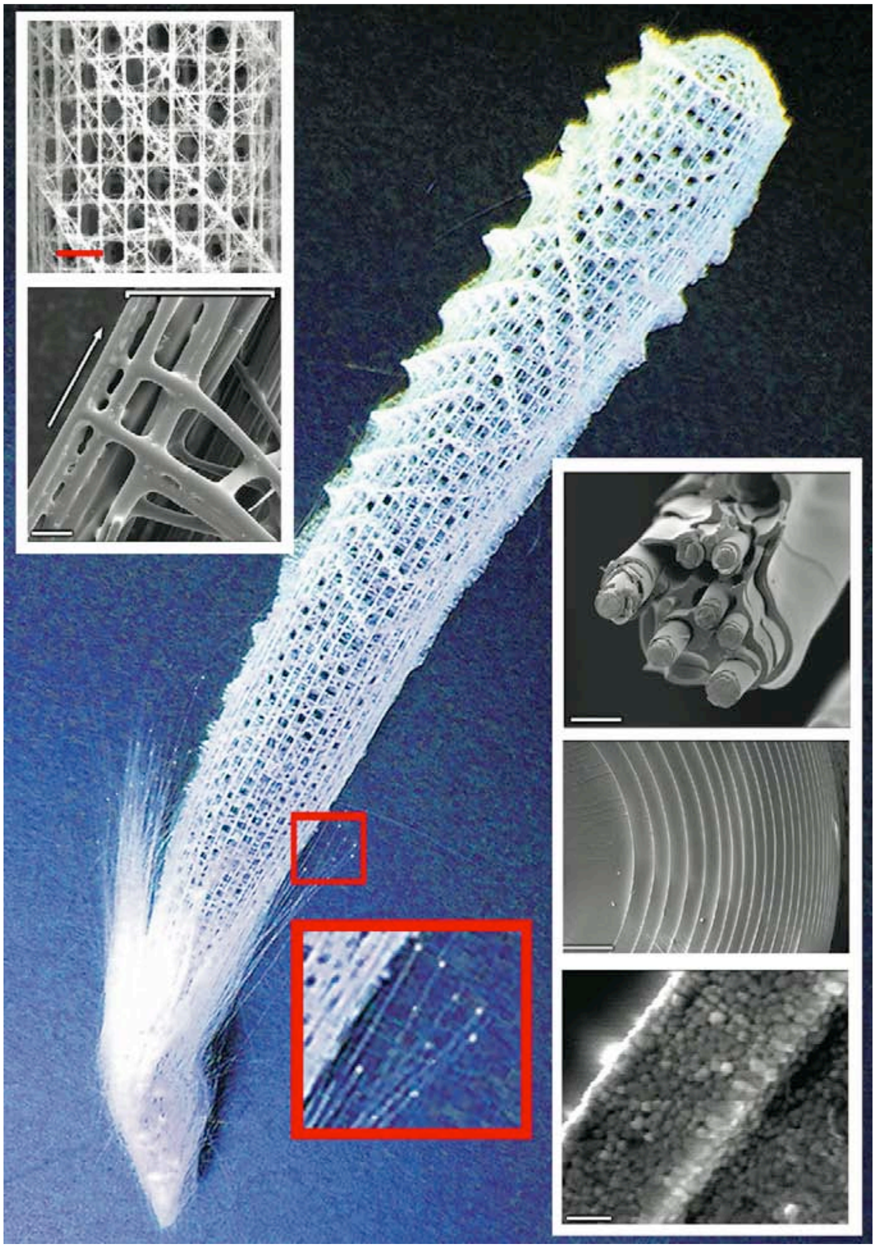

Figure 1.7 Skeleton of Venus's flower-basket, a glass sponge. Glass fibers form a crown at the base of the sponge house, of which optical properties are similar to those of commercial fibers shown in insets on the right column.[2]

Superstrong glass Nature creates superstrong structures made of brittle fully organic, hybrid organic/inorganic, or nearly fully inorganic. Their superstrength is realized through the successive hierarchical assembly of the constituent structural building blocks (Fig 1.7).[2] Nature's ability to improve inherently poor and brittle building materials, such as glass, calcium phosphate, or calcium carbonate, by introducing a molecular-level control of the structure implemented by biomolecules (proteins, polysaccharides) is unmatched in technology. Inspired by that, engineers bundle up small glass fibers rather than a single big fiber. As a result, the final products often confer a remarkable capacity for recovery, self-repair, and fault resistance or tolerance.

Honeycomb Honeycombs is composed of a perfect hexagonal cellular structure, which optimizes the packing shape and save the amount of material (Figure 1.8A).[19] Similarly, the human-made honeycomb structure is regarded as an ideal structure for the construction of control surfaces of an aircraft and it can be applied to fabricate airplane wings, elevators, tails, the floor, and many other parts that need strength and large dimensions while maintaining low weight (Fig. 1.8B).[3] The structural reinforcement is more beneficial than the use of expensive and rare materials.

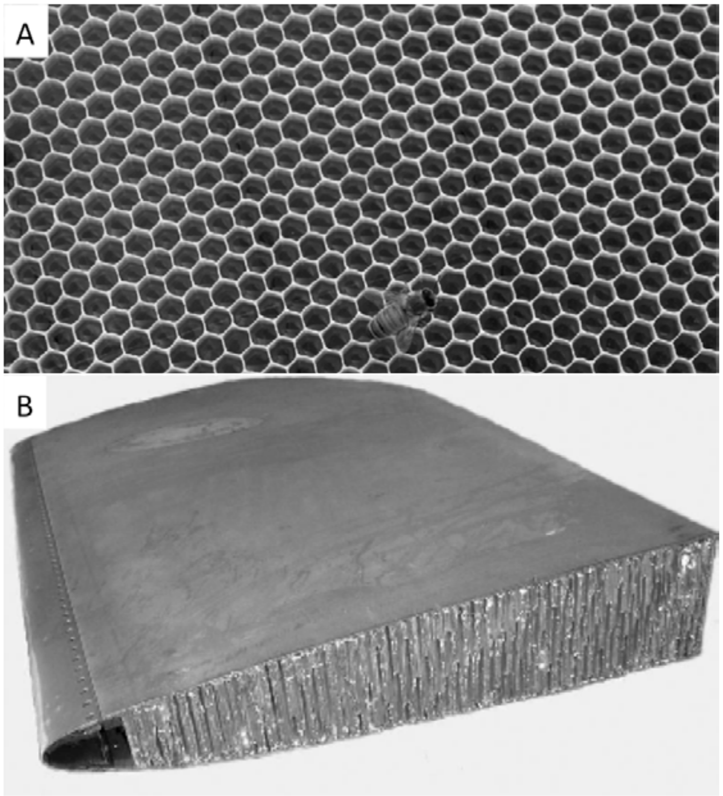

Figure 1.8 Honeycomb as a Strong, Lightweight Structure (A) The honeycomb structure, the simplest and lowest energy) 2D foam.[19] **(B)** A cross-section of a honeycomb structure that plays an important role in the construction of aircraft control surfaces.[3]

Nanocoral Analogous to natural sea corals, stand-alone cellular probe, nanocoral was developed to provide rough surfaces to maximize surface area for efficient capture of light and food particles (Fig. 1.9).[20] The nanocorals consisted of two material: hemispheric substrate made of polystyrene and a thin rough surface made of a gold. The substrate was functionalized for target binding and the thin gold film was for reporting binding mediated with a surface plasmon on the gold.

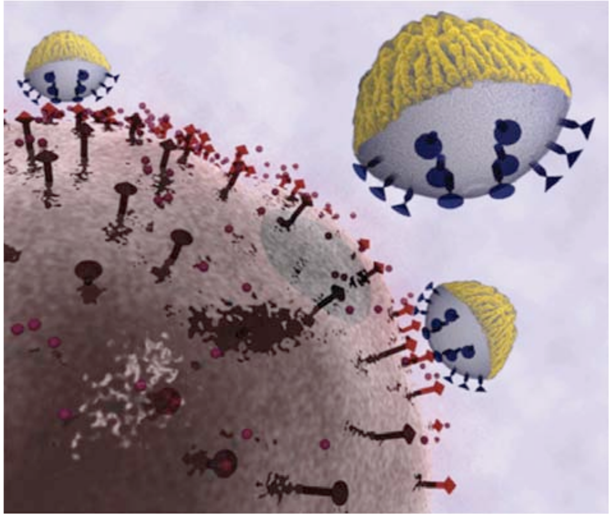

Figure 1.9 Schematic of biologically inspired nanocorals. Multifunctional nanoprobes for targeting, sensing, and drug delivery.[20]

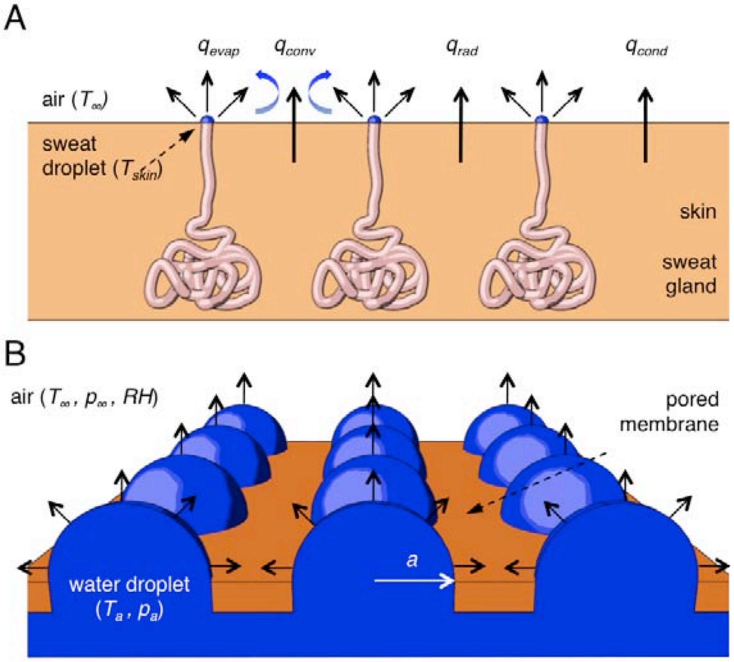

Figure 1.10 Schematic representations show heat dissipation from (A) Heat dissipation from a human skin and **(B)** a porous cooling membrane.[21]

Artificial cooling surface One of the most advanced thermoregulation systems found in nature is the skin system of the human body, which relies on evaporation, the most effective and even available when the environmental temperature exceeds the skin temperature (Fig. 1.10A). The parameters of a droplet-array on a porous membrane were theoretically evaluated to maximize the capability of evaporation on the area-limited surface (Fig. 1.9B).[21] The model considered droplet interaction, which degraded cooling performance and suggested to design the array at the maximum density rather than smaller pore size. The model will provide a guideline for designing artificial cooling membranes for the future.

1.1.3 Mechanics

Moving animals have adapted to complex and variable environments by inventing various locomotion mechanisms: climbing, crawling, swimming, flying, and walking. Animals move based on bones and muscular structures, which behave nonlinearly and relevantly to adapt to undetermined environmental conditions. In addition, the structures are mostly passive, which utilize the inherent properties of materials and are effective in saving energy and materials. Considering these benefits, people can invent engineered machines and robotic systems inspired by or mimicking the locomotion mechanisms, which provide higher adaptability, and performance while minimizing the need for complex control mechanism systems, weight, and energy.[22-25]

Climbing Compared to walking on the ground, climbing requires further power to overcome the gravity. Also, the additional design for grabbing surface is required. These requirements are the strong burden in designing climbing robots. In nature, solutions exist: climbing animals with tails. A flat-tailed house gecko, Cosymbotus platyurus facilitates its tail to balance during not only running on the ground but also climbing rapidly (Fig. 1.11A).[26] The balancing mechanism of tailing is applied to a bio-inspired climbing robot, RiSE (Robot in Scansorial Environment) to respond to the accidental falling (Fig. 1.11B).[27]

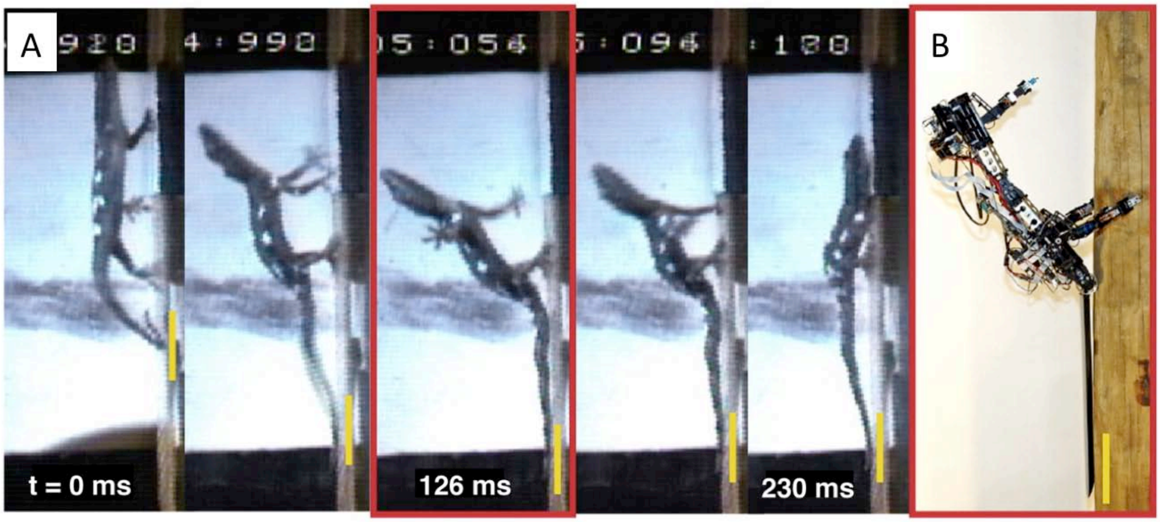

Figure 1.11 Climbing gecko and legged climbing robot. (A) A Gecko uses its tail to avoid overturning while climbing.[26] **(B)** RiSE, a quadrupedal, bio-inspired robot, uses an active tail as an emergency fifth limb to assist in climbing.[27]

Crawling An invertebrate's body is composed of segmented sections and moves by crawling even without using legs. The crawling provides the benefits of the small body volume along with its rigid internal structure. For instance, an inchworm has a sucker-like appendages at the front and back and moves its body by repeating its sucking and releasing (Fig. 1.12A). The inchworm-crawling mechanism was applied to design an inchworm colonoscopic robot, which maneuvers through small intestinal (Fig. 1.12B).[28] The robot could make sharp turns by changing its structure. Furthermore, the robot is expected to operate wirelessly through body skin.

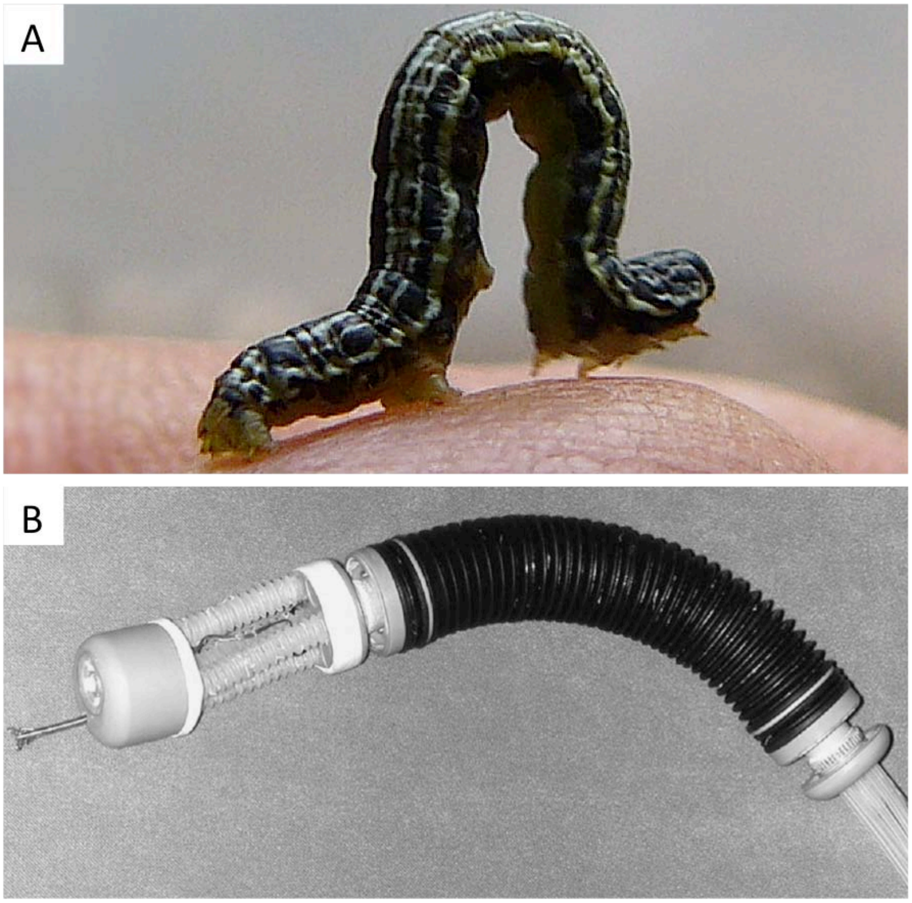

Figure 1.12 Crawling inchworm and a robot (A) A butterfly larva **(B)** An inchworm colonoscopic robot.[28]

Swimming robot
Swimming fish inspired to design fish robot swimming in 3D (Fig. 1.13).[29] The fish robot mimics the undulating motions of a real fish swimming and turning while avoiding obstacles and responding to environmental changes. In the near future, cyber-fish will swim with other living counterparts and may be employed to monitor leakage in oil pipelines and assist underwater vehicles.

Flying robot Flying with flapping wings is advantageous over flying with fixed wings: low speed hovering, sharp turning, and backward flying. Micromechanical flying insect (MFI) was developed by mimicking flies, which create large force without relying on steady-state fluidics and use less power (Fig. 1.14).[30] MFI utilized piezoelectric actuators and flexible thorax structures to provide the needed power density and wing stroke, and carried lithium batteries charged by solar cells. Such tiny robots may serve as a spy robot to inspect suspect facilities.

Figure 1.13 A swimming robot navigating in an acquarium.[29]

Figure 1.14 Micromechanical Flying Insect (MFI).[30]

Walking robot The legs of creatures allow navigating on the ground while supporting their bodies. Along with delicate balancing systems, walking creatures have their own skeletomuscular structures as natural resonant systems to improve their stability during fast locomotion. Particularly, two-legged humanoid walking robot gain more attention compared to other non-humanoid robots due to the capability to maneuver in human environments by ascending, descending stairs, and walking streets (Fig. 1.15). Eventually, humanoid robots may serve humans in the ordinary spaces while closely interacting with humans.

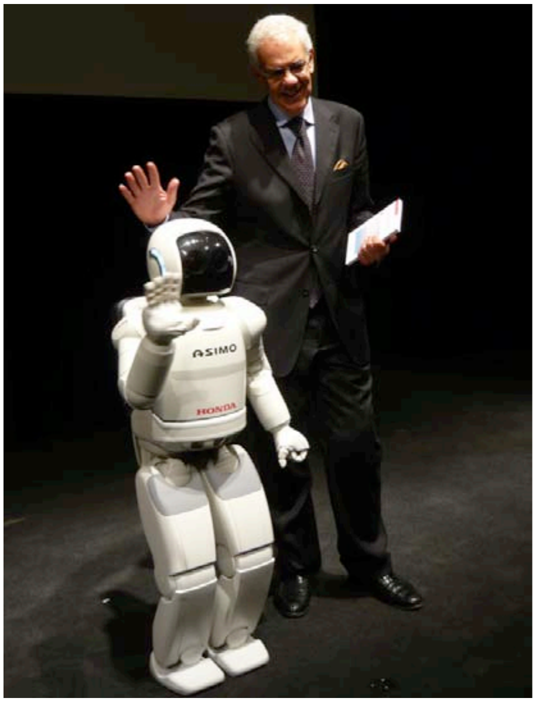

Figure 1.15 A fully independent, walking humanoid robot
(http://asimo.honda.com/EducationMaterials.aspx.)

1.1.4 Actuators

In order to interact with complex environments, biological systems require actuators to respond to the environment or perform functions. Understanding and studying the mechanisms of the biological actuating systems have inspired the development of new artificial actuators operating from nanoscale to macroscale while requiring low power and less materials.[31-34]

DNA actuator DNA has the specificity based on the base pairing, which allows creating complex nanostructures. Besides, the DNA-based nanostructures can be predicted by numerical simulation. The capability of building nanostructure was further exploited in a sequential manner to realize the unidirectional motion, a DNA walker (Fig. 1.16).[35] Certain nucleotide was transferred along oligonucleotide track by repeating enzyme-based cleaving and ligating between neighborin anchorages. This technique is expected to serve as an effective gene transfer at sub-nanometer scale.

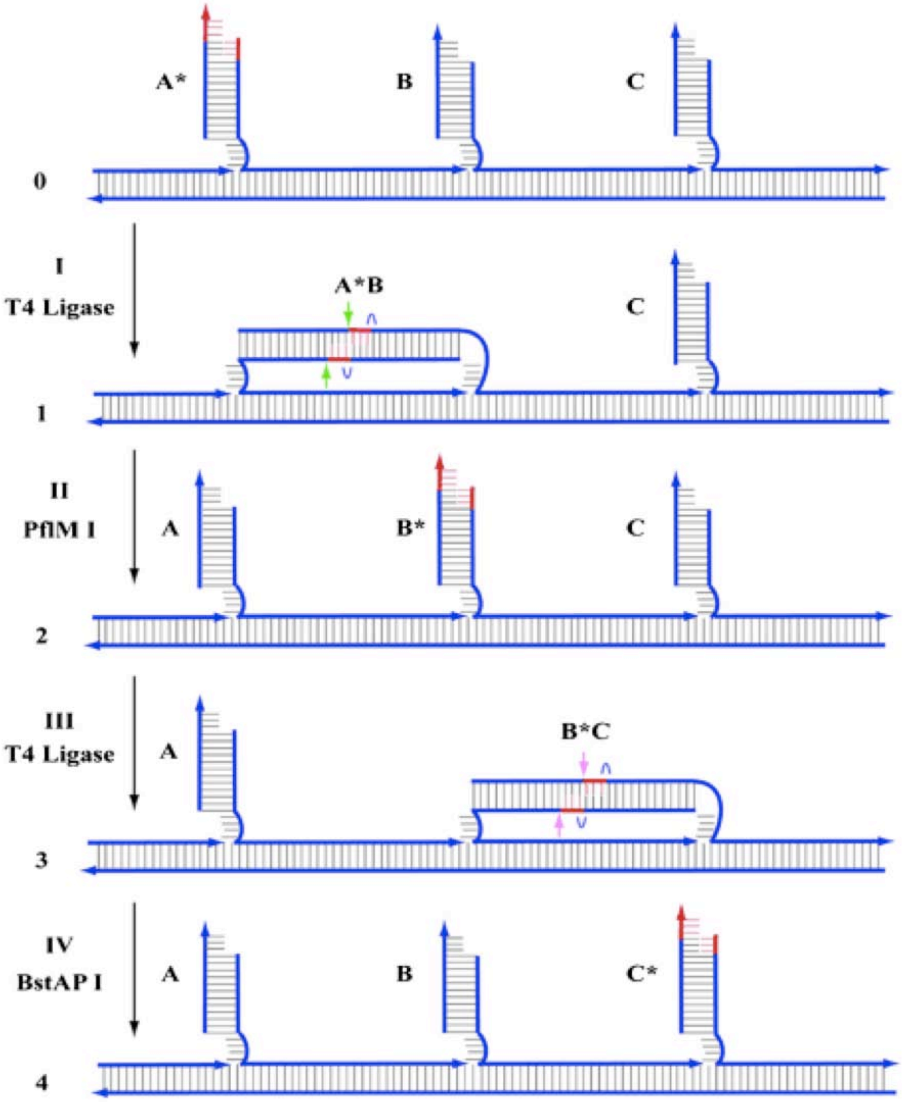

Figure 1.16 An enzyme-assisted DNA walker. The six- nucleotide walker is colored red.[35]

Molecular motor Molecular motors serve to move signaling proteins along microtubules as tracks (Fig. 1.17).[36] The mechanism is to convert chemical energy into mechanical movement through ATP hydrolysis. The hydrolysis induces a conformational change in a globular motor domain, which is further amplified and translated into movement associated with accessory structural motifs. Even though functions of the motors are not clear yet, it is expected to exploit the functions of the molecular motors for the development of nanocargo vehicle in the future.

Bacteria flagellar motor The bacterial flagellar motor is a nanorotor, built from about 20 different kinds of parts. It can rotate clockwise and counterclockwise at speeds around 100 Hz, which provides a thrusting force enough for cells to swim (Fig. 1.18A).[37] Their motors are driven by proton transfer along a transmembrane electrochemical gradient, or proton-motive force. F1 motors were integrated with microfabricated inorganic pedestals and nickel nanopropellers to form a hybrid biotic/abiotic device (Fig. 1.18B).[38] Also, a molecular sorter with kinesin was proposed to move microtubules along separate paths using hydrodynamic and electrical steering forces. The flagellar motor-inspired actuators will serve as nanopumps to concentrate molecules or convert the chemical gradients into chemical energy.

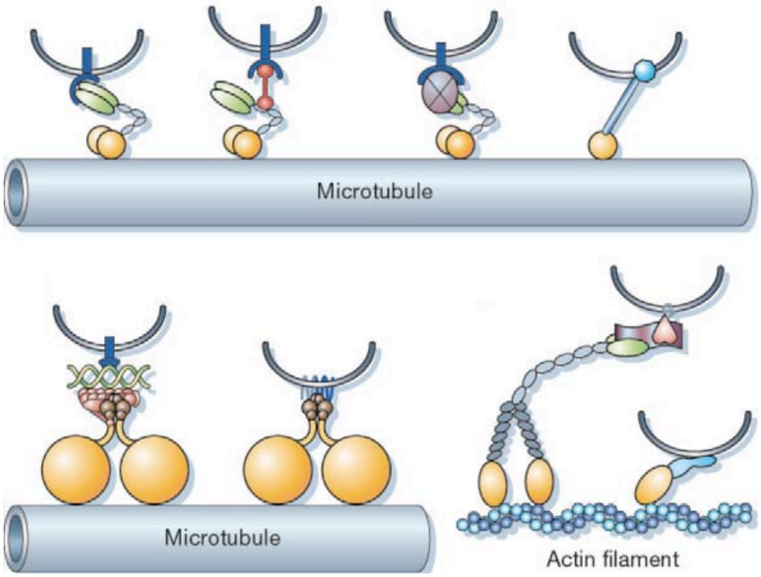

Figure 1.17 Types of motor-cargo linkage. Kinesin (top), dynein, and myosin (bottom), respectively.[36]

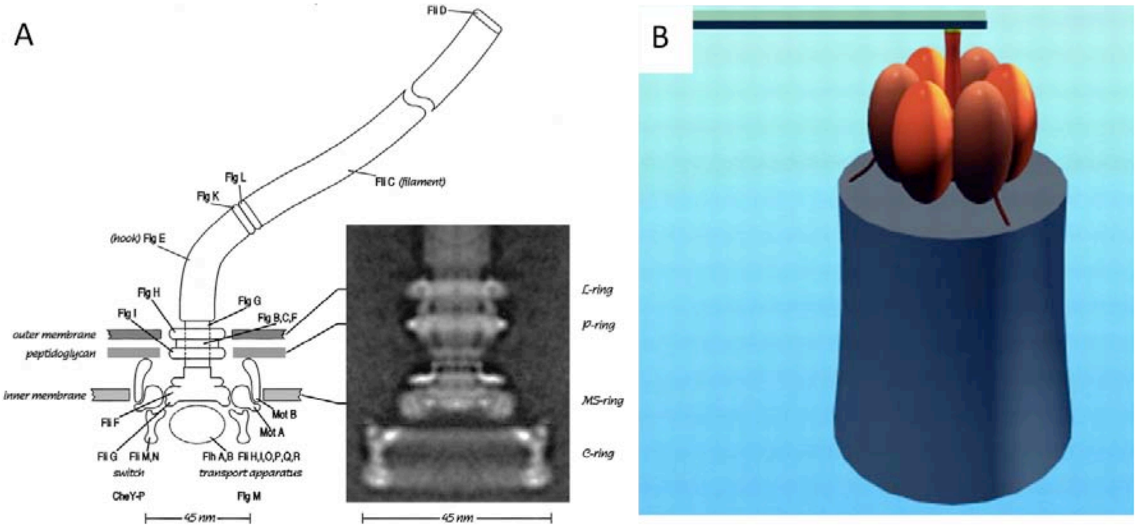

Figure 1.18 Flagellar motors in a bacteria[37] and attached to a nanopropellar[38].

Cell/Tissue actuator Muscle tissue, mechanical actuators serve as the source of force, work, and power in moving creatures. The muscle actuator provides unparalleled efficiency and plasticity and is a practical, responsive, and robust actuator. Among the approaches to engineer functional living muscle actuators, self-organization in developing animals has the design flexibility and the integrability with devices (Fig. 1.19).[39] Each myogenic precursor cell can proliferate to self-organize and combine with substrates, which allows forming hybrid actuators. Furthermore, the hybrid actuator can be realized in a dense array format.

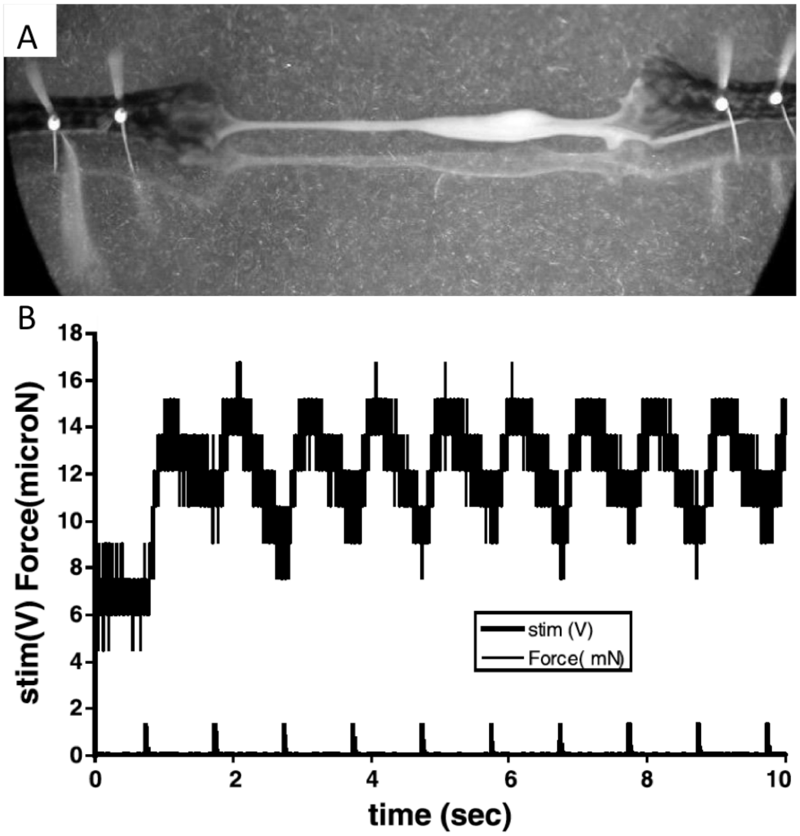

Figure 1.19 Self-organized cardiac muscle actuator. (A) Self-organized cardiac muscle construct, attached to laminin-coated suture anchors. **(B)** Electrically elicited force trace from the cardiac muscle.[39]

Artificial muscle actuator Even though self-organized natural muscle is widely used in all animals, the drive mechanism is complex and persists for short time at a millisecond scale. To overcome the disadvantages of natural muscles, the electro-active polymers (EAP) were developed with a long duration and a large displacement controlled by electrical signaling (Fig. 1.20).[40] EAP was realized by two activation mechanisms: ionic (involving mobility or diffusion of ions) and electronic (driven by electric field or Maxwell Forces). The electronic polymers (electrostrictive, electrostatic, piezoelectric, and ferroelectric) can hold the induced displacement as long as the activation of a DC voltage. EAP-based actuator would be widely used for robotic applications.

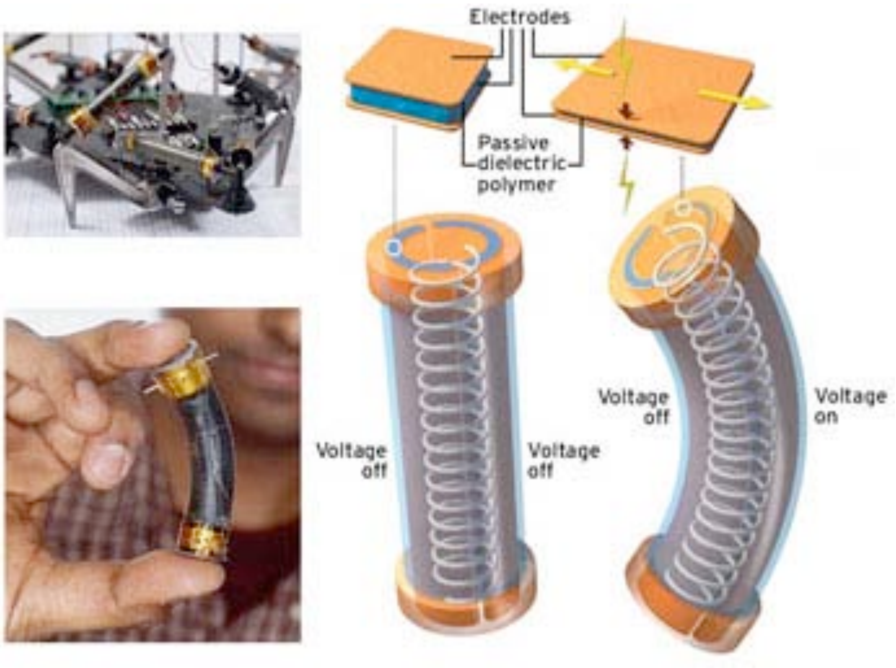

Figure 1.20 Electronic muscle. Artificial muscle is activated by the movement of electrons between passive dielectric polymers.[40]

1.1.5 Sensors

Living creatures have invented enormously various sensory systems (seeing, smelling, tasting, hearing, and feeling) far beyond the human-made systems with respect to high adaptability, low-cost production, ultra sensitivity, and compactness. For example, pit vipers rely on infrared and thermal detecting sensory to find prey and bats utilize ultrasonic wave to locate flying prey in the darkness. Alternatively, the canine has a nose more sensitive than any other human-maid sensors, which can detect drugs, explosives, and human scents. Understanding these ingenious biological designs, as well as, physical, chemical, and biological processes underlying the biological sensory systems could lead to the development of advanced artificial sensor systems.

Artificial compound eye Compounds eyes common in insects are composed of spherically arranged lenses, which collect incident light at a wide-range angle and has the capability of a wider field-of-view than any other human-made lenses. Artificial compound eyes were fabricated with 3D configuration inspired by natural compound eyes, the ommatidia of insects[41] (Fig. 1.21). The fabricated compound eyes could attract a huge interest due to the benefits of wide field of view, and its integrability with conventional silicon based planar devices that does not require expensive and delicate fabrication techniques.

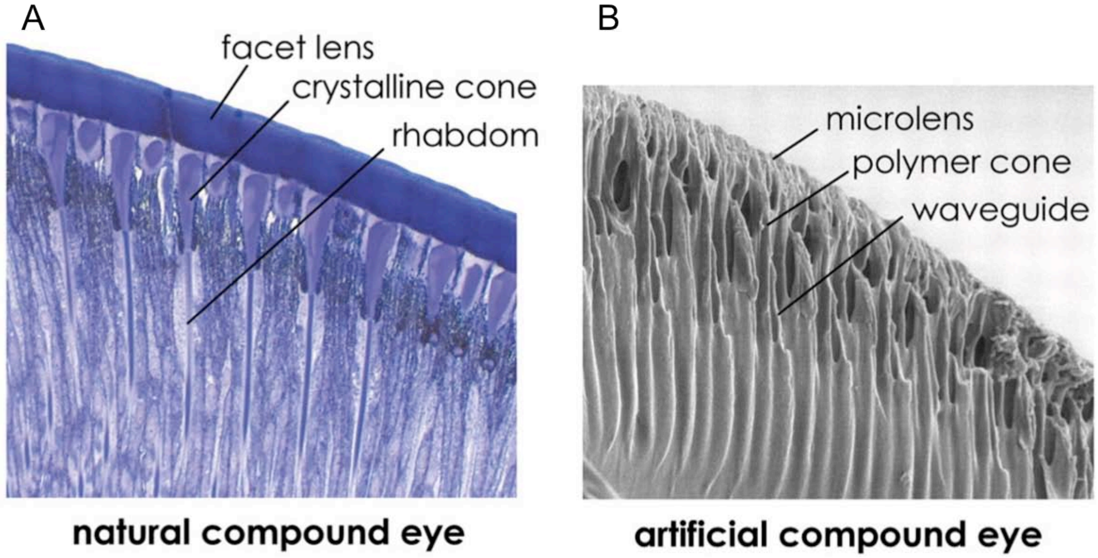

Figure 1.21 Cross-sectional views of compound eyes. (A) An optical micrograph of a honeybee's apposition compound eye.[42] **(B)** A scanning electron micrograph of an artificial compound eye.[41]

Artificial nose The sense of smell is to detect chemicals of airborne molecules.[43] The detail of mechanism is that odorant molecules bind to G-protein-coupled receptors, which activate Na+ channel in sensory neurons (Fig. 1.22A). The action potential is delivered to the brain, which matches signal patterns from different receptors to the previous records for identification of odorants. An electronic nose, so-called, 'ENose' has been developed by understanding how natural noses detect odor molecules and mimicking the sensory mechanism based on the electric conductivity of multiple polymer films specific for different target molecules (Fig. 1.22B). The electric signals from the sensor can be further analyzed by computer algorithms for precise target recognition. The developed electric nose is now used to diagnose food hygiene.

Artificial tongue The sense of taste is to identify dissolved molecules and ions by using clusters of receptor cells in the taste buds (Fig. 1.23A).[44] The taste has two different aspects, in which one is the five basic tastes of the human tongue: sour, salt, bitter, sweet, and umami. Each taste bud cell has receptors, which are transmembrane proteins, that bind to the specific molecules and ions corresponding to five distinctive taste sensations. The other aspect is the descriptive taste, the impression based on the previous experience recorded in the brain. Electronic tongues or taste sensors are, however, developed specifically for classified targets in a food, beverage, water, and process fluids; the results are not directly corresponding to human sensations. Most of the sensing mechanisms are based on electrochemical techniques: potentiometry, voltammetry, and conductometry or optical detection. For example, potentiometry measures the potential of electrodes across an ion-selective membrane with two electrodes (Fig. 1.23B).[45] Different membrane materials specifically respond to different types of targets. These types of devices are widely used for measuring a number of ionic species, the most important being the pH electrode. In order to detect multiple targets or analyze the complex molecules, the sensors are fabricated in an array format and the measured data are further analyzed by computer algorithms for the identification. The sensor arrays are expected to be useful particularly for quality control of products and processes.

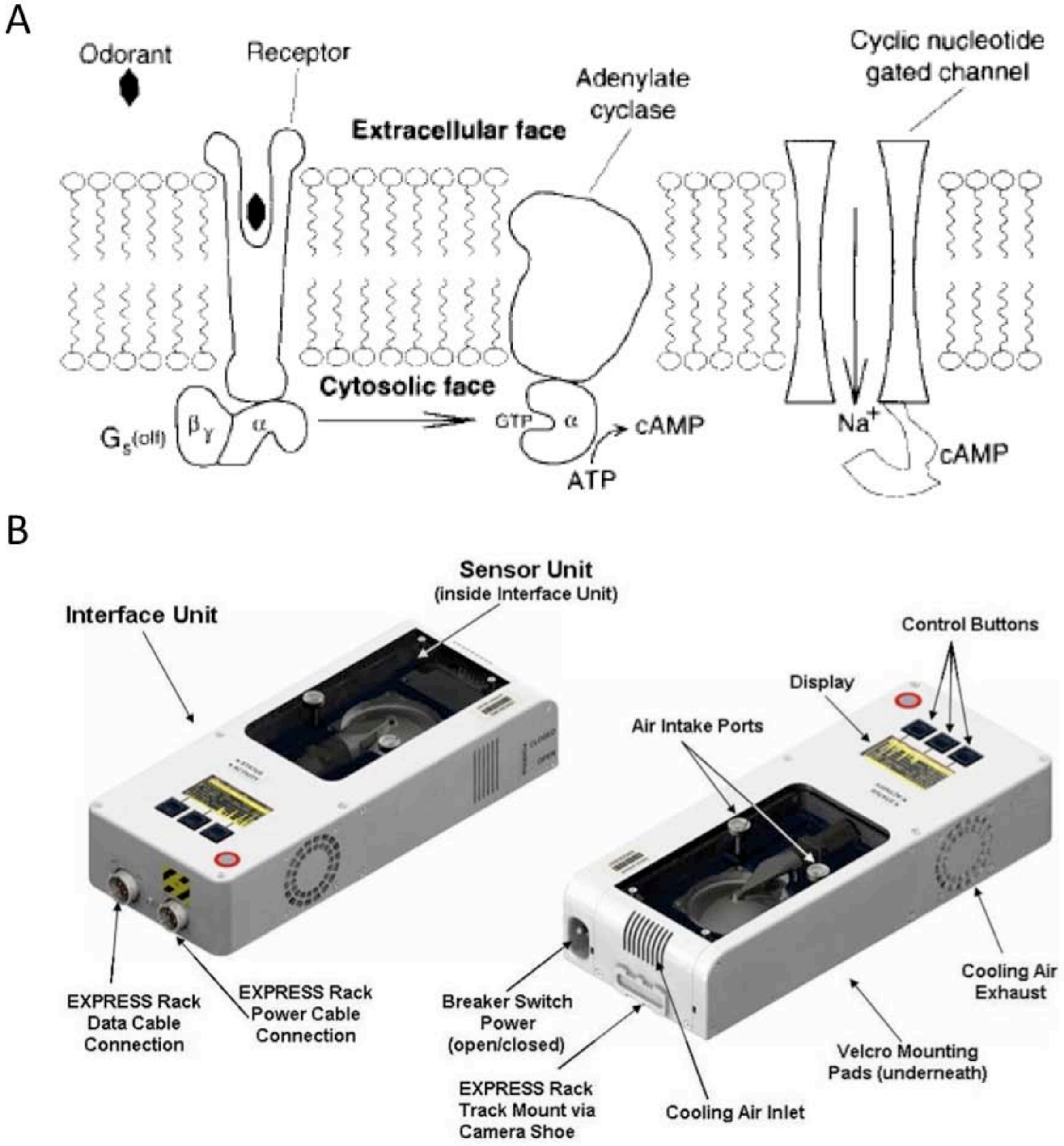

Figure 1.22 A schematic and a photo of nose (A) A schematic shows the smelling process in biological nose.[43] **(B)** A photo shows the configuration of an artificial ENose (Courtesy of JPL Electronic Nose).

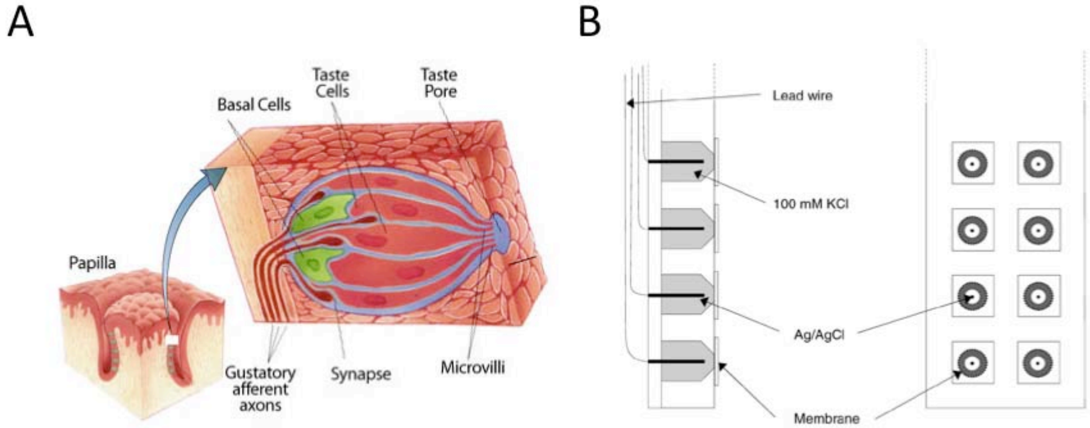

Figure 1.23 Schematic representations of tongues. (A) An anatomic view of a taste bud (http://www.nicks.com.au/index.aspx?link_id=76.1354). **(B)** Cross sectional and top views of an artificial tongue array.[45]

Artificial hair cell A hair cell is one type of a mechanosensor, which translates pressure waves into electric signals that nerves can convey to the brain (Fig. 1.24A).[46,47] Insects and fish use the clusters of hair cells to monitor flowing of air and water, respectively. In mammals, the hair cell is further utilized as a sensory receptor of the auditory system and the vestibular system. The hair cell is composed of bundles of hair-like stereocilia connected by thin filaments called tip-links. The detail of the mechanism is that pressure waves displace the stereocilia, which opens channels in the hair allowing positive ions to flow into the cell, a process called depolarization. The depolarization spreads rapidly through the cell and releases a signaling substance called a neurotransmitter that transmits the signal to the brain. There are two types of artificial hair cell sensors developed in 1D, 2D, or 3D: cantilevers parallel[48] and perpendicular[49] to substrates by replicating the structure and mimicking the functions of a biological haircell[50] (Fig. 1.24B). The mechanism of the artificial hair cells is to measure a viscous force proportional to flow velocity at a micrometer scale by reading voltage changes through strain gauges. The early types were made of brittle silicon, which was replaced by polymer more robust and even applicable to curved surface. The polymer-based hair cells need to be improved to compensate temperature and humidity changes.

Artificial whisker A whisker in various animals and insects is a touch sensor, which senses position, shape, and even surface features of objects to avoid collision of obstacles and to find food (Fig. 1.25A).[51] For example, a cat's whiskers are so sensitive that they can detect the slightest directional change in a breeze. The detail mechanism of encoding signals and identifying texture is still unclear and many models have been proposed to explain how the nervous system analyzes signals from whiskers. Among them, the resonance model describes how animals can identify the texture of surface by contacting their whiskers with the surface, sensing mechanical resonances of whiskers with length variation.[52] A mouse robot could navigate the environment with obstacles using its whiskers without human control (Fig. 1.25B).[53] Motion control that has been inspired by a rodent's whisker might be a simple yet effective idea for robots to explore confined surroundings and scuttle though pipes to perform repair work in the darkness.

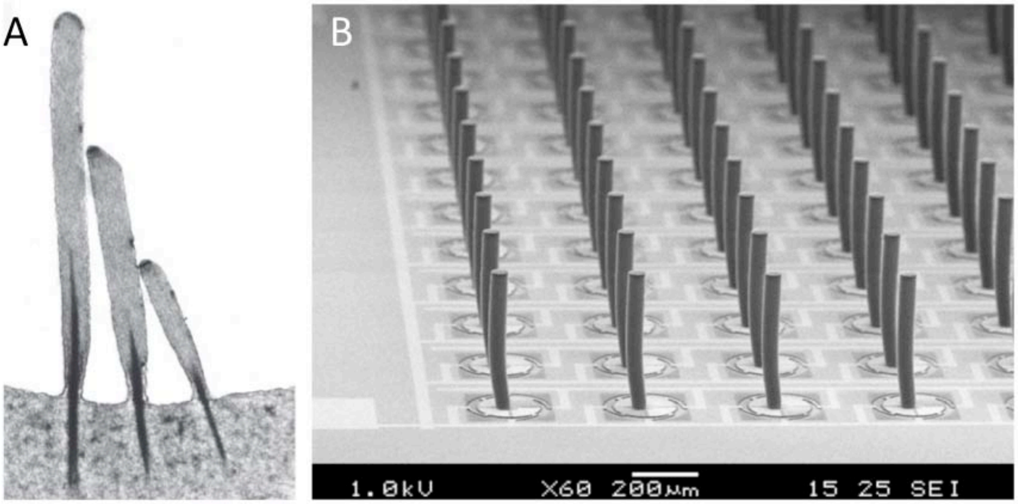

Figure 1.24 Hair cells (A) SEM image (left) and structure and protein composition (right) of auditory hair cells.[47] **(B)** Array of spiral-suspended sensory hairs.[50]

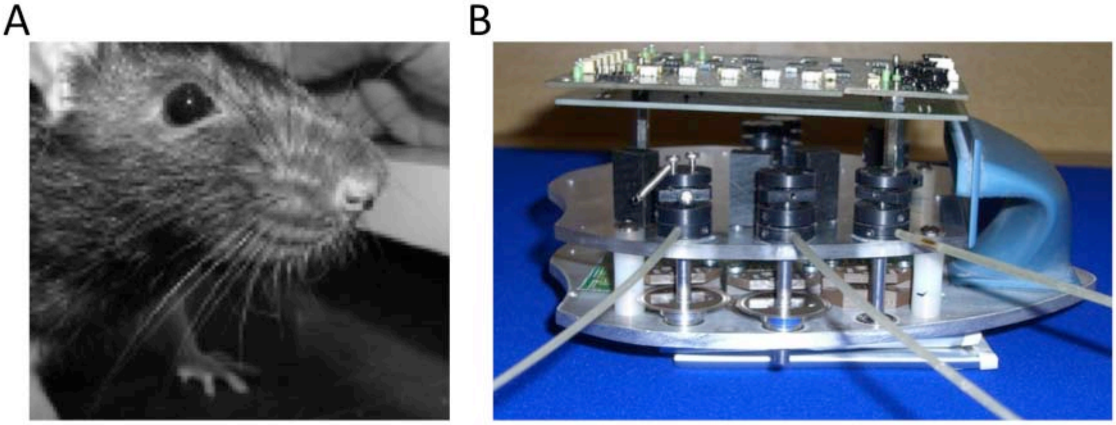

Figure 1.25 Photos of whiskers (A) A rat with whiskers.[52] **(B)** Whiskerbot navigating with artificial whiskers.[53]

1.2 OUTLINE OF THE WORK

In this dissertation, biologically inspired 'microsystem' will be the focused research topic, and the major components. The overall goal of this dissertation is to develop major building blocks, particularly 'microfluidics' and 'nanobiosensors' in microsystems aiming for quantitative biomedicine. Particularly, understanding natural mechanisms and getting an inspiration from nature will aid the development of the microfluidics and nanobiosensor.

Chapter 2 and chapter 3 present the development of a xylem-inspired microfludic diode and its application to cell co-culturing, respectively. Chapter 4 and chapter 5 provide the development of aptamer-based nanobiosensor analogous to antibody-antigen recognition and its application to cancer diagnostics, respectively. In chapter 6, an integrated microfluidics with developed aptamer-based nanobiosensor was applied for the quantification of angiogenesis with cultured breast cancers. Chapter 7 presents the conclusions of these efforts.

References:

(1) Vogel, S., *Cats' Paws and Catapults: Mechanical Worlds of Nature and People,* **1998**, W. W. Norton & Company, New York, 382 pps.
(2) Committee on Biomolecular Materials and Processes, National Research Council, *Inspired by Biology: From Molecules to Materials to Machines,* **2008**, National Academies Press, Washington, DC, 118 pps.
(3) Bar-Cohen, Y., *Biomimetics: Biologically Inspired Technologies*, **2006**, CRC Press, New York, 520 pps.
(4) Forbes, P., *The Gecko's Foot*, **2005**, W. W. Norton & Company, New York, 272 pps.
(5) Benyus, J. M., *Biomimicry: Innovation Inspired by Nature*, **1997**, William Morrow. 288 pps.
(6) Li, C., Pruitt, L., King, K. Nanoindentation Differentiates Tissue-Scale Properties of Native Articular Cartilage, *Journal of Biomedical Materials Research,* **2006**, 78A(4), 729-738.
(7) Dzenis Y. Spinning continuous fibers for nanotechnology, *Science* **2004**, 304, 1917-1919.
(8) Lee, Haeshin, Dellatore, Shara M., Miller, William M., Messersmith, Phillip B. Mussel-Inspired Surface Chemistry for Multifunctional Coatings, *Science,* **2007**, 318, 426-430.
(9) Autumn, K., Liang, Y., Hsieh, T, Zesch, W., Chan, W.-P., T. Kenny, Fearing, R., Full, R.J. Adhesive force of a single gecko foot-hair, *Nature,* **2006**, 405, 681-685.
(10) Hillebrecht, J. R. *et al.*, Optimization of Protein-Based Volumetric Optical Memories and Associative Processors by Using Directed Evolution, *NanoBiotechnology*, **2005**, 1, 141-151
(11) Haumann, M., Liebisch, P., Müller, C., Barra, M., Grabolle, M., Dau, H., Photosynthetic O_2 Formation Tracked by Time-Resolved X-ray Experiments, *Science*, **2005**, 310, 1019 – 1021.
(12) Capadona, J. R., Shanmuganathan, K., Tyler, D. J., Rowan, S. J., Weder, C., Stimuli-Responsive Polymer Nanocomposites Inspired by the Sea Cucumber Dermis, *Science*, **2008**, 319, 1370 – 1374.
(13) Lee, H. and *et al.*, Mussel-Inspired Surface Chemistry for Multifunctional Coatings, *Science*, **2007**, 318, 426 – 430.
(14) Jiang, L., Zhao, Y., Zhai, J., A Lotus-Leaf-like Superhydrophobic Surface: A Porous Microsphere/Nanofiber Composite Film Prepared by Electrohydrodynamics, *Angew. Chem. Int. Ed.,* **2004**, 43, 4338-4341.
(15) Autumn, K., Liang, Y. A., Hsieh, S. T., Zesch, W., Chan, W.-P., Kenny, W. T., Fearing, R. and Full, R. J., Adhesive force of a single gecko foot-hair, *Nature*, **2000**, 405, 681-68.
(16) Qu, L., Dai, L., Stone, M., Xia, Z. and Wang, Z. L., Carbon Nanotube Arrays with Strong Shear Binding-On and Easy Normal Lifting-Off, *Science,* **2008**, 322, 238– 242.
(17) Vukusic, P., Sambles, J. R., Photonic structures in biology, *Nature* **2003**, 424, 852-855.
(18) Kim, H. *et al*, Structural color printing using a magnetically tunable and lithographically fixable photonic crystal, *Nature Photonics* **2009**, 3, 534 – 540.

(19) D. Weaire, Kelvin's foam structure: a commentary, *Philosophical Magazine Letters*, **2008**, 88, 91 – 102.

(20) Wu, L. Y., Ross, B. M., Hong, S. G., Lee, L. P., Bioinspired Nanocorals with Decoupled Cellular Targeting and Sensing Functionality, *Small*, **2010**, 6, 503-507.

(21) Kokalj, T., Cho, H., Jenko, M., Lee, L. P., Biologically inspired porous cooling membrane using arrayed-droplets evaporation, *Appl. Phys. Lett.,* **2010**, 96, 163703-163705.

(22) Yanoviak, S.P., Dudley, R., Kaspari, M. Directed aerial descent in arboreal ants, *Nature,* **2005**, 433, 624-626.

(23) Altshuler, D.L., Dudley, R., McGuire, J.A. Resolution of a paradox: hummingbird flight at high elevation does not come without a cost, *Proc. Nat'l Acad. Sci.,* **2004**, 101(51), 17731-17736.

(24) Jusufi, A., Goldman, D.I., Revzen, S., Full, R.J. Active tails enhance arboreal acrobatics in geckos, *Proc. Nat'l Acad. Sci.,* **2004**, 105(11), 4215–4219.

(25) H. Sato, C. W. Berry, B. E. Casey, G. Lavella, Y. Yao, J. M. VandenBrooks, and M. Maharbiz, A cyborg beetle: Insect flight control through an implantable tetherless microsystem, *21st IEEE Intl. Conf. on Micro Electro Mechanical Systems,* **2008**, 164-16.

(26) Qu, L., Dai, L., Stone, M., Xia, Z., Wang, Z. L., Carbon Nanotube Arrays with Strong Shear Binding-On and Easy Normal Lifting-Off, *Science*, **2008**, 322, 238 – 242.

(27) Habib, M. K., Bioinspiration and Robotics: Walking and Climbing Robots, *I-Tech*, Vienna, Austria, EU, September **2007**, pp. 544.

(28) Kim, B., Lim, H. Y., Park, J. H., Park, J.-O., Inchworm-like Colonoscopic Robot with Hollow Body and Steering Device, *JSME Int. J.*, **2006**, 49, 205-212.

(29) H. Hu, Biologically Inspired Design of Autonomous Robotic Fish at Essex, *Proc. of IEEE on Advances in Cybernetic Systems*, **2006**, 1-8.

(30) Steltz, E., Avadhanula, S., Wood, R. J., and Fearing, R. S., Characterization of the Micromechanical Flying Insect by Optical Position Sensing, *IEEE Int. Conf. on Robotics and Automation*, **2005**.

(31) Wood, R.J., Steltz, E., Fearing, R.S. Nonlinear Performance Limits for High Energy Density Piezoelectric Bending Actuators, *Proc. of IEEE Int. Conf.*, **2005**

(32) Bar-Cohen, Y., *Electroactive Polymer (EAP) Actuators as Artificial Muscles–Reality, Potential and Challenges*, **2001**, SPIE Press, Bellingham, Washington, 671 pps.

(33) Chiou, T.H., Kleinlogel, S., Cronin, T., Caldwell, R., Loeffler, B., Siddiqui, A., Goldizen, A., Marshall, J. Circular polarisation vision in a stomatopod crustacean, *Current Biology* **2008**, 18, 429-434.

(34) Schillebeeckx F., Mey, F. D., Peremans, H. Bio-Inspired Sonar Antennae: enhancing directivity patterns for localization, *Proc. of the 2nd Biennial IEEE/RAS-EMBS Int. Conf. on Biomedical Robotics and Biomechatronics*, **2008**, 366-371.

(35) Yin, P., Yan, H., Daniell, X. G., Turberfield, A. J., Reif, J. H., A Unidirectional DNA Walker That Moves Autonomously along a Track, *Angew. Chem. Int. Ed.*, **2004**, 43, 4906 – 4911.

(36) Schliwa, M., Woehlke, G., Molecular motors, *Nature* **2003**, 422, 759-765.

(37) Berg, H. C., The Rotary Motor of Bacterial Flagella, *Annual Review of Biochemistry*, **2003**, 72, 19-54.

(38) Soong, R. K., Bachand, G. D., Neves, H. P., Olkhovets, A. G., Craighead, H. G., Montemagn, C. D., Powering an Inorganic Nanodevice with a Biomolecular Motor, *Science,* **2000**, 290, 1555 – 1558.

(39) Schneider, B.L., Peduto, G., Aebischer, P. A, self-immunomodulating myoblast cell line for erythropoietin delivery, *Gene Ther.*, **2001**, 8, 58–66.

(40) Chuc, N. H., Koo, J. C., Lee, Y. K., Nam, J. D., Choi, H. R., Artificial Muscle Actuator Based on the Synthetic Elastomer, *Int. J. of Control, Automation, and Systems*, **2008**, 6, 894-903.

(41) Jeong, K.-H., Kim, J., Lee, L. P. Biologically Inspired Artificial Compound Eyes, *Science,* **2006**, 312, 557-561.

(42) Greiner, B., Ribi, W. A., Warrant Retinal and optical adaptations for nocturnal vision in the halictid bee *Megalopta genali,* E. J. *Cell Tissue Res.,* **2004**, 316, 377.

(43) Buck, L., Axel, R., A novel multigene family may encode odorant receptors: a molecular basis for odor recognition, *Cell,* **1991**, 65(1), 175-87.

(44) Nelson, G., Chandrashekar, J., Hoon, M. A., Feng, L., Zhao, G., Ryba, N. J. P., Zuker, C. S., An amino-acid taste receptor, *Nature,* **2002**, 416, 199-202.

(45) Winquist, F., Krantz-Rülcker, C., Lundström, I., Electronic Tongues, *MRS Bulletin/Oct.,* **2004**, 29, 726-731.

(46) Gillespie, P. G., Walker, R. G., Molecular basis of mechanosensory transduction, *Nature* **2001**, 413, 194-202.

(47) Fettiplace, Hackney, R., C. M. The sensory and motor roles of auditory hair cells, *Nature Reviews Neuroscience,* **2006**, 7, 19-29.

(48) Ozaki, Y., Ohyama, T., Yasuda, T., Shimoyama, I., An air flow sensor modeled on wind receptor hairs of insects, *Proc. MEMS,* **2000**, 531-536.

(49) Chen, J., Fan, Z., Engel, J., Liu, C., Towards Modular Integrated Sensors: The Development of Artificial. Haircell Sensors Using Efficient Fabrication Methods, *Proc. IEEE/RSJ,* **2003b**, 2341-2346.

(50) Dijkstra, M., Baar, J. J. V., Wiegerink, R. J., Lammerink, T. S. J., Boer, J. H. D., Krijnen, G. J. M. Artificial sensory hairs based on the flow sensitive receptor hairs of crickets, *J. Micromech. Microeng.,* **2005**, 15, S132–S138.

(51) Heller MA, Texture perception in sighted and blind observers, *Percept Psychophys,* **1989**, 45, 49–54.

(52) Wolfe, J., Hill, D. N., Pahlavan, S., Drew, P. J., Kleinfeld, D., Feldman, D. E., Texture Coding in the Rat Whisker System: Slip-Stick Versus Differential Resonance, *PLoS Biology,* **2008**

(53) Pearson, M. J., Pipe, A. G., Melhuish, C., Mitchinson, B., Prescott, T. J., Whiskerbot: A Robotic Active Touch System Modeled on the Rat Whisker Sensory System, *Adaptive Behavior,* **2007**, 15, 3, 223-240.

CHAPTER 2: BIOLOGICALLY INSPIRED MICROFLUIDIC DIODE

Currently, engineered fluidic diodes are limited to narrow applications due to the requisition of their multi-layered structures, complex connections, and external control equipments. Interestingly, nature is abundant in resources for inspiration that can provide innovative solutions for many technological barriers. Here we show a bidirectional fluidic diode regulating flow in both directions, which is particularly inspired by understanding how xylem pores maintain water transport in plants. The functions are completely estimated based on an analytical model, which considers the hysteresis of contact angles and rounded diodes intrinsic to fabrication limits. Advantageously, it performs in a single-layered structure and requires only a single pressure source for the operation. Furthermore, we demonstrate large-scale and self-regulated droplet and cell patterning in microfludic platforms assembled with the fluidic diodes. We believe that the elucidation of xylem embolism regulation allows functional large-scale microfluidic circuits and autonomous fluidic controls for applications in biosciences and analytical chemistry.

2.1 INTRODUCTION

Motivation Nature provides an abundant source of inspiration to foster innovation as well as challenge us to elucidate them in greater depth. The systematic study and abstraction of functional design from nature generate novel solutions for technological barriers and appreciation of the beauty of nature.[1-6] For example, an understanding of the transport mechanism of sap, which plays a critical function in plant systems, can provide us new insights for autonomous fluidic control systems. Particularly, plant systems establish effective signaling among plant cells via plasmodesmata[7, 8] and maintain successful water transport in xylems via pit pores[9, 10]. In detail, plasmodesmata are known to traffic proteins and various forms of RNA dilated by the binding of ‘gate-open’ proteins, and compartmented xylems maintain water transport even in the presence of gas embolism (or ‘xylem embolism’) by utilizing the physics of surface tension at the xylem pores.

Water regulation in xylems Understanding the mechanism behind the regulation of xylem embolism in plants might solve current bottlenecks in developing functional large-scale microfluidic circuits and autonomous fluidic controls[11] (Fig. 2.1). Specifically, water that flows through xylem conduits becomes meta-stable under excess negative pressure during dehydration in the daytime. When water pressure in xylem conduits is below a cavitation pressure, gas bubbles form in the xylem conduits and grow further to fill the conduits with gas, a process known as xylem embolism, which can potentially inhibit xylem function.[12-14] However, plant systems maintain the water transport through the neighboring xylem conduits with the aid of surface tension that contains the gas within its conduit. In other words, the created gas bubble is isolated within the xylem conduit by surface tension that holds (or “pins”) the water-gas interface (or “meniscus”) at the pores on the inter-conduit pit membranes, which help to prevent the movement of the meniscus from a gas-filled conduit to a water-filled one.[15, 16] Finally, under stable xylem pressure, it has been hypothesized that the embolism is repaired—that is, the gas-embolized conduits become re-filled with water—by additional power sources, including meniscus-restoration by surface tension on hydrophilic xylems,[17] pressure increase in water-filled conduits by osmosis,[18] or pressure decrease in gas-filled conduits as phloem and living cells secrete osmoticum,[19] or bubble dissolution.[20, 21] While the principle mechanism of water transport is still arguable, we know that an intricate network of xylem vessels facilitates the transport of water within plants.

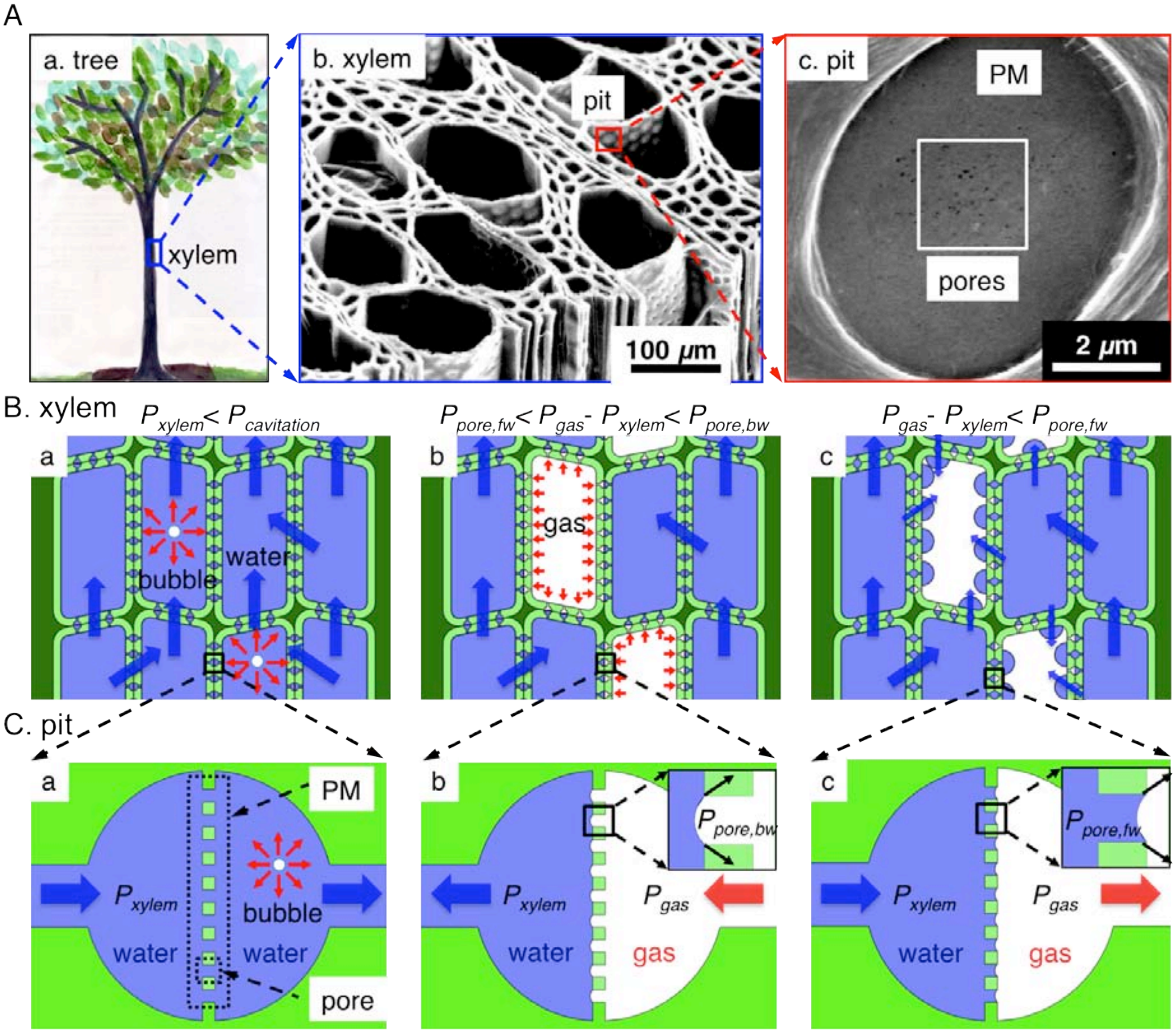

Figure 2.1 Xylem embolism regulation by pores on inter-conduit membranes in xylems. **(A)** A painting and SEM images show a tree (a), xylem conduits in its trunk (b),[22] and a pit membrane on the xylem wall (c) including homogeneously distributed pores on the pit membrane (PM).[23] **(B-C)** Schematic representations illustrate the status of initial bubble generation (a), fully expanded bubbles embolizing xylem conduits (b), and embolism recovery (c) in the view of xylem conduits (B) and the pit (C).

Diode Analogous to xylem Photos and a schematic diagram of the flow rate-pressure (*Q-ΔP*) characteristic curve of a bi-directional biologically inspired fluidic diode are illustrated (Fig. 2.2). Interestingly, the *Q-ΔP* characteristic of a bidirectional fluidic diode shows similar behavior to the current-voltage (*I-V*) characteristic curve of Josephson tunneling junction excluding the superconducting current. A characteristic curve and photos of a bi-directional bidirectional fluidic diode is analogous to a xylem pore (Fig. 2.2 C).

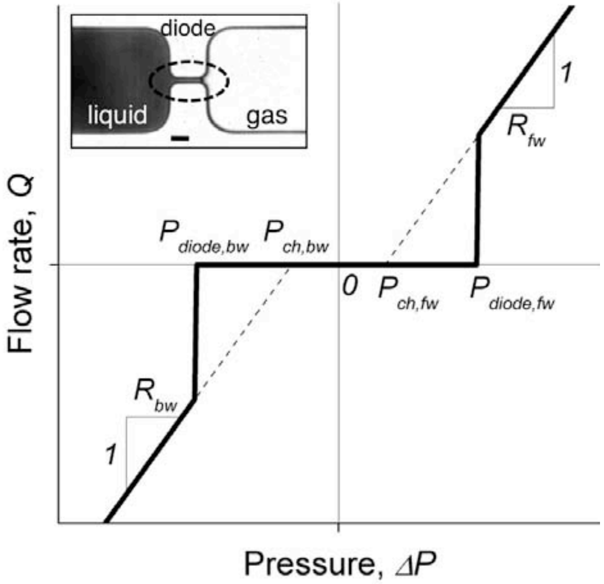

Figure 2.2 Biologically inspired bidirectional fluidic diode. A characteristic curve and photos detail a bidirectional fluidic diode. Inset presents zoomed-in views of the diode. A scale bar is 5 μm.

2.2 PRINCIPLES

Hydraulic Resistance We employ the model of Stokes flow with low Reynolds number (*Re* < 0.3), no external force, and incompressible Newtonian fluid, which reduces the Navier-Stokes equation to: $0 = -\nabla P + \mu \nabla^2 u$, where P is pressure (Pa), μ is dynamic viscosity (Pa.s), and $u = u_x(y,z)$ is velocity of fluid (m.s^{-1}) (Fig. 2.3). Flow velocity in a straight channel is transformed into a two-dimensional Fourier series of a square channel under no slip boundary conditions:

$$u_x\left(y,z\right) = \sum_{n\ odd}^{\infty} \sum_{m\ odd}^{\infty} \left\{ u_{nm}\left(x\right) \times \sin\left(n\frac{\pi}{w_1} y\right) \times \sin\left(m\frac{\pi}{h} z\right) \right\}, \tag{2.1}$$

where $\nabla P(x) = (P_g - P_l)/(L_o + x)$, h is height (m), w_1 is width of the straight channel (m), $u_{nm}(x) = -16\nabla P(x)\Big/\left(\pi^4 \mu \times n \times m \times \left((n/w_1)^2 + (m/h)^2\right)\right)$, L_o is liquid length before bursting (m), P_l is liquid pressure (Pa), and P_g is gas pressure (Pa). A flow rate, Q, is obtained by multiplying the cross-sectional area (= $w_1 \times h$) with the mean flow velocity, $\bar{u} = \left(\int_0^{\Delta L}\int_0^{h}\int_0^{w_1} u_x(y,z)\,dydzdx\right)\Big/(\Delta L \times h \times w_1)$, to get for forward and backward flows, respectively:

$$Q_{fw} = \Delta P \times (64 w_1 \times h \times NM)\Big/\left(\pi^6 \mu \times (L_o + \Delta L/2)\right) \equiv \Delta P/R_{ch,fw}, \tag{2.2}$$

$$Q_{bw} = \Delta P \times (64 w_1 \times h \times NM)\Big/\left(\pi^6 \mu \times (L_o - \Delta L/2)\right) \equiv \Delta P/R_{ch,bw}, \tag{2.3}$$

where $\Delta P = P_l - P_g$, ΔL is the change in the liquid length after bursting (m), $NM = \sum_{n\ odd}^{\infty}\sum_{m\ odd}^{\infty}\left[1\Big/\left\{(n \times m)^2 \times \left((n/w_1)^2 + (m/h)^2\right)\right\}\right]$ is the index for a rectangular channel.

Therefore, the hydraulic resistances of a rectangular straight channel in forward and backward directions are:

$$R_{ch,fw} = \pi^6 \mu \times (L_o + \Delta L_o/2)/(64 w_1 \times h \times NM), \tag{2.4}$$

$$R_{ch,bw} = \pi^6 \mu \times (L_o - \Delta L_o/2)/(64 w_1 \times h \times NM). \tag{2.5}$$

A microfluidic diode and a limiting valve (LV) are modeled as a sharply-edged and a rounded rectanglualr slit in a Stokes region, respectively. As a result, the hydraulic resistance of the diode and the limiting valves are[24]:

$$R_{diode} = -4\pi\mu \times \kappa\Big/\left(w_o^2 \times h \times \ln\left(\cos(\kappa\pi/2)\right)\right), \tag{2.6}$$

$$R_{LV} = -4\pi\mu \times \kappa \times C_{LV}\Big/\left(w_o^2 \times h \times \ln\left(\cos(\kappa\pi/2)\right)\right), \tag{2.7}$$

where $\kappa = w_o/w_1$ is the fraction of the opened area, w_o is opened width (m) at the diode (or the saftety valve), and C_{LV} is a correction factor for the limiting valve. Therefore, the total hydraulic resistances for forward and backword directions are equal to the resistances of a forward straight channel and single fluidic diode in serial and resistances of a backward straight channel and three limiting valves in serial, respectively, equated as:

$$R_{fw} = \pi^6 \mu \times (L_o + \Delta L_o/2)/(64 w_1 \times h \times NM) - 4\pi\mu \times \kappa\Big/\left(w_o^2 \times h \times \ln\left(\cos(\kappa\pi/2)\right)\right), \tag{2.8}$$

$$R_{rw} = \pi^6 \mu \times (L_o - \Delta L_o/2)/(64 w_1 \times h \times NM) - 12\pi\mu \times \kappa \times C_{LV}\Big/\left(w_o^2 \times h \times \ln\left(\cos(\kappa\pi/2)\right)\right). \tag{2.9}$$

The constants are provided in Table 2.1.

Pressure on the Meniscus After bursting, pressure is exerted on a meniscus opposite to flow direction along the straight channel. The pressure includes a static term, surface tension at the meniscus along the straight channel, and a dynamic term, P_{dyn} which compensates the modeling error caused by the assumption of Stokes flow at the meniscus:

$$P_{st,fw} = -\sigma \cdot \left(2\cos\theta_{ca,PDMS} / w_1 + \left(\cos\theta_{ca,PDMS} + \cos\theta_{ca,FOTS}\right) / h\right) + P_{dyn}, \tag{2.10}$$

$$P_{st,bw} = -\sigma \cdot \left(2\cos\theta_{cr,PDMS} / w_1 + \left(\cos\theta_{cr,PDMS} + \cos\theta_{cr,FOTS}\right) / h\right) + P_{dyn}, \tag{2.11}$$

where σ is surface tension of the liquid (N.m^{-1}), θ_{ca} and θ_{cr} are advancing and receding contact angles (°), respectively, on PDMS or FOTS-coated glass surfaces, and P_{dyn} is the dynamic pressure that compensates for the modeling error. The constants are provided in Table 2.1.

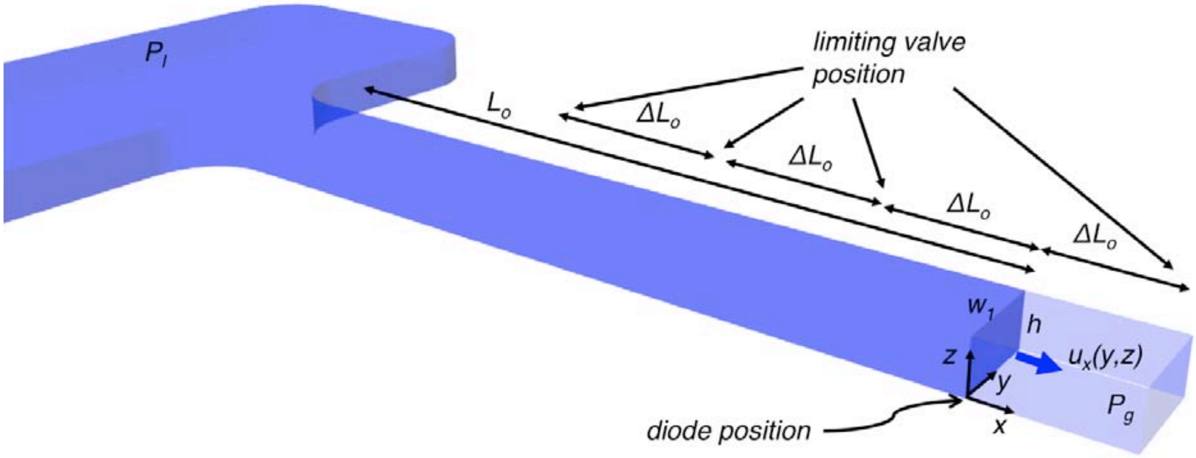

Figure 2.3 Geometry of a straight channel. Before bursting, liquid initially fills a large inlet reservoir and a long rectangular straight channel of width (w_1), height (h), and length (L_o). After bursting, the meniscus moves forward or backward with the change of length (ΔL_o). The limiting valves are designed to limit the movement of meniscus within the range during repeated experiments for systematic characterization.

Table 2.1 List of parameters in the bidirectional fluidic diode model with symbols, definitions, and values employed.

Symbol	Definition	Value
Constants		
σ	surface tension of a dye at 20 °C (N.m^{-1})	0.045
μ	dynamic viscosity of a dye at 20 °C (Pa.s)	1.002e-3
h	diode height (m)	6.1e-6
L_o	liquid length before bursting (m)	3e-3
ΔL_o	change in the liquid length after bursting (m)	1e-3
r_e	radius of curvature at a rounded edge of a diode (m)	1.4~5.6e-6

$\theta_{ca,PDMS}$ $/\theta_{cr,PDMS}$	advancing/receding contact angles of dye on a PDMS surface at 20 °C (°)	105/84
$\theta_{ca,FOTS}$ $/\theta_{cr,FOTS}$	advancing/receding contact angles of dye on a FOTS-glass surface at 20 °C (°)	93/66
C_{LV}	correction factor for flow resistance of a limiting valve	0.5 ~ 1.2
P_{dyn}	pressure compensating modeling error (kPa)	-2.6 ~ 10
Input Variables		
w_o	width of a diode	
w_1	width of a straight channel	
β	edge angle of a diode	
Output Variables		
θ^*_{mf}	forward meniscus angle for bursting, $\left(=\min(\theta^*_{ef}+\theta_{ca,PDMS},\pi)\right)$	
θ^*_{mb}	backward meniscus angle for bursting, $\left(=\min(\pi+\theta^*_{eb}-\theta_{cr,PDMS},\pi)\right)$	
w^*_f	forward diode width for bursting, $\left(=w_o+2r_e\cdot\left(1-\cos\left(\theta^*_{ef}\right)\right)\right)$	
w^*_b	backward diode width for bursting, $\left(=w_o+2r_e\cdot\left(1-\cos\left(\theta^*_{eb}\right)\right)\right)$	
$\theta^*_{ef}/\theta^*_{eb}$	forward/backward angle increments for busting at rounded edges	
$P_{FPS,fw}$ $/P_{FPS,bw}$	forward/backward bursting pressures of a diode	
$P_{st,fw}$ $/P_{st,bw}$	forward/backward resistant pressures along straight channels	
P_l/P_g	pressures of liquid/gas	
ΔP	operational pressure, $\left(=P_l-P_g\right)$	
$R_{ch,fw}$	hydraulic resistance along a stratight channel for forward direction, $\left(=\pi^6\mu\times\left(L_o+\Delta L_o/2\right)/\left(64w_1\times h\times NM\right)\right)$	
$R_{ch,bw}$	hydraulic resistance along a stratight channel for backward direction, $\left(=\pi^6\mu\times\left(L_o-\Delta L_o/2\right)/\left(64w_1\times h\times NM\right)\right)$	
R_{FPS}	hydraulic resistance of a diode, $\left(=-4\pi\mu\times\kappa/\left(w_o^2\times h\times\ln\left(\cos\left(\kappa\pi/2\right)\right)\right)\right)$	
R_{LV}	hydraulic resistance of a limiting valve, $\left(=C_R\times R_{FPS}\right)$	
R_{fw}	total hydraulic resistances for forward direction, $\left(=R_{ch,fw}+R_{diode}\right)$	
R_{bw}	total hydraulic resistances for backward direction, $\left(=R_{ch,fw}+3R_{LV}\right)$	

Xylem Pressure Related to Embolism The critical pressures related to xylem embolism are the pressures inducing embolism spreading and repair. Gas embolism spreads into adjacent xylems when the pressure difference across a pit membrane, ΔP ($= P_{xylem} - P_{gas}$), exceeds the backward bursting pressure at xylem pore, $P_{pore,bw}$, which is characterized as:

$$\Delta P \leq P_{pore,bw} = -4\sigma \cdot \cos\theta_{mr} / D_p, \tag{2.12}$$

where D_p is pore diameter (m), $\theta_{mr} = \min(\pi + \beta - \theta_{ca}, \pi)$ (°), β is pore edge angle (°), and θ_{ca} is contact angle (°) on a xylem surface, which is measured to be always less than 90°. Meanwhile, water returns back into an embolized xylem conduit when the pressure difference is restored over a surface tension on the pit aperture, P_{ap}, which is characterized as:

$$\Delta P \geq P_{ap} = -4\sigma \cdot \cos\theta_{ca} / D_{ap}, \tag{2.13}$$

where D_{ap} is diameter of a pit aperture (m). The values of the constants are provided in Table 2.

Hydraulic Resistance of a Pit The flow through a pit is assumed to be in a Stokes region due to the low Reynolds number. The hydraulic resistance of a pit membrane, R_{PM}, regarded as a thin membrane with a hexagonal array of pores, is modeled as[24]:

$$R_{PM} = 24\mu \big/ \left(N_p \times D_p^3\right) \times f(\kappa), \tag{2.14}$$

where N_p is the number of pores on the pit membrane, $\kappa = D_p / D_{ap}$, and $f(\kappa) = 1 - 0.880\kappa^{1.5} - 0.103\kappa^{2.5} - 0.056\kappa^{3.5} - 0.036\kappa^{4.5}$.

The hydraluic resistance of a pit aperture, R_{ap} regarded as a single circular pore of finite length, L_{ap}, is modeled as[24, 25]:

$$R_{ap} = \left(128\mu \times L_{ap}\right) \big/ \left(\pi D_{ap}^4\right) + 24\mu / D_{ap}^3. \tag{2.15}$$

Therefore, the total resistance of a pit is equal to R_{PM} and R_{ap} in series:

$$R_{pit} = R_{PM} + 2R_{ap}. \tag{2.16}$$

The values of the constants are provided in Table 2.2.

Table 2.2 List of parameters in the xylem model with symbols, definitions, and values employed.

Symbol	Definition	Value
Constants		
σ	surface tension of water at 20 °C ($N.m^{-1}$)	0.072
μ	dynamic viscosity of water at 20 °C (Pa.s)	1.002e-3
N_p	number of pores on a pit membrane	100
D_{ap}	diameter of a pit aperture (m)	1.6e-6
L_{ap}	length of a pit aperture (m)	2e-6
β	pore angle of a pit (°)	30
Input Variables		
D_p	pore diameter on a pit membrane	
θ_{ca}	static contact angle of a water on a pit surface	
Output Variables		
$P_{pore,bw}$	backward bursting pressures at pores	
P_{ap}	surface tension on a pit aperture	
P_{xylem} $/P_{gas}$	pressures of xylem/gas	
ΔP	pressure difference at the interface of water and gas, $\left(= P_{xylem} - P_{gas}\right)$	
R_{PM}	hydraulic resistance of a pit membrane	
R_{ap}	hydraluic resistance of a pit aperture	
R_{pit}	hydraulic resistance of a pit, $\left(= R_{PM} + 2R_{ap}\right)$	

2.3. DESIGN

Design of fluidic diode As xylem pores prevent the movement of the meniscus within a critical xylem pressure range, the bidirectional fluidic diodes prevent liquid from flowing within a critical pressure range and then allow flow proportional to the applied pressure above the critical pressures in forward and backward directions (Fig. 2.4). The preventing mechanism is the pinning of a meniscus at the Bidirectional fluidic diode edge via surface tension by dropping the liquid contact angle below a critical contact angle required for movement (forward: an advancing contact angle, θ_{ca}; or backward: a receding contact angle, θ_{cr}) by the amount of the edge angle of the bidirectional fluidic diode, β. The meniscus remains pinned until the meniscus angle (forward: θ_{mf}, or backward: θ_{mb}) surpasses the critical contact angle (when $\theta_{mf} \geq \beta + \theta_{ca,PDMS}$ for forward, or $\theta_{mb} \geq \beta + \pi - \theta_{cr,PDMS}$ for backward) or the pinning force reaches its maximum value (when $\theta_{mf} \geq \pi$ for forward, or $\theta_{mb} \geq \pi$ for backward).[26] An increase in the meniscus angle results in a decrease in curvature radius, which consequently causes an increase in the surface tension pinning the meniscus at the edge of diodes. Therefore, the bidirectional fluidic diode can regulate flow via surface tension by the structural properties.

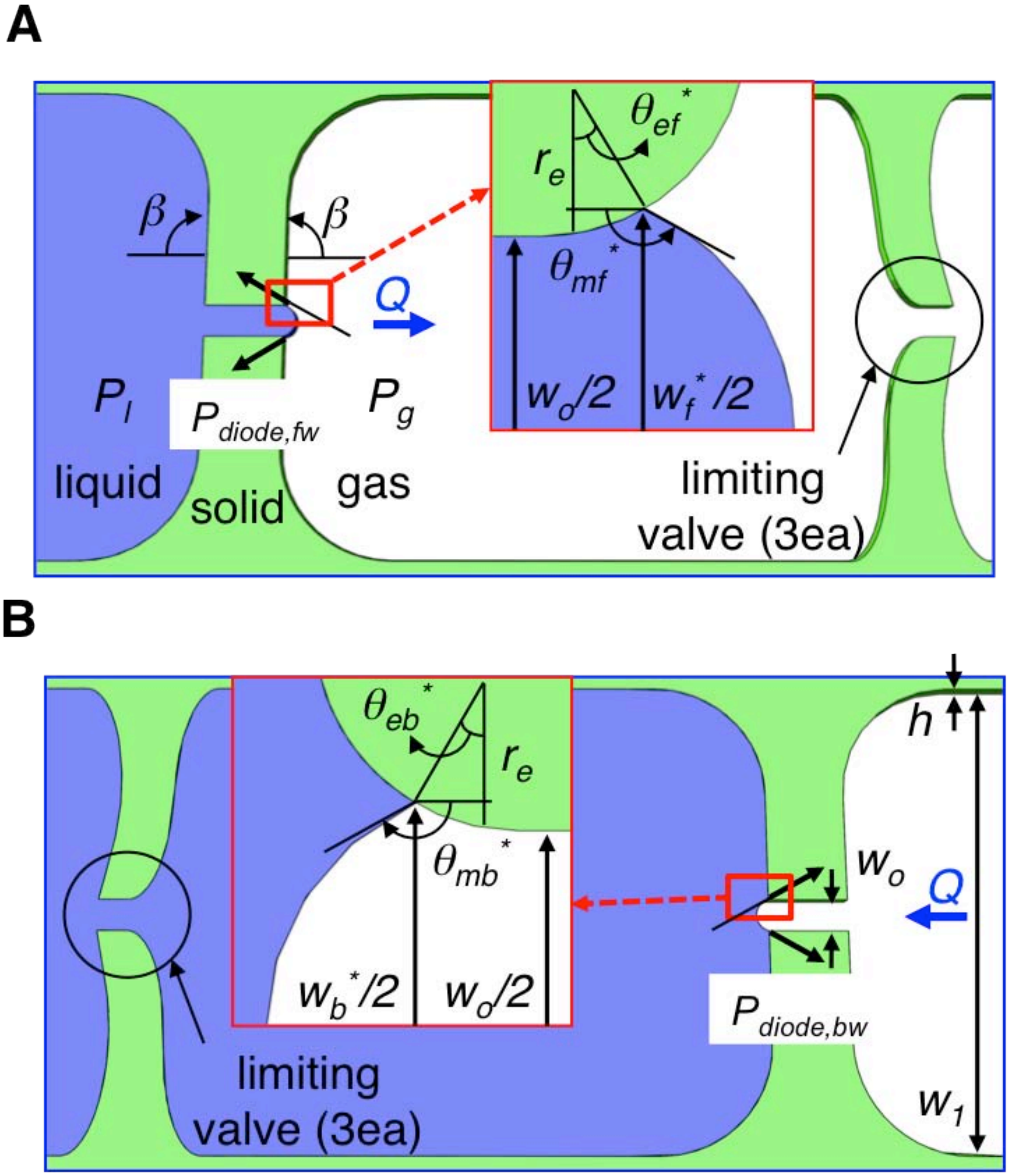

Figure 2.4 Schematic representations describe a bidirectional fluidic diode operating in forward (A) and backward (B) directions.

Pinning The behaviors of bidirectional fluidic diodes are analyzed before and after bursting, separately. Before the bursting, the meniscus is in a static equilibrium condition and the applied "operational" pressure, ΔP (the difference between liquid pressure, P_l, and gas pressure, P_g), needs to overcome the pinning surface tension:

$P_{diode,fw} = -\sigma \times \left(2\cos\theta^*_{mf} \big/ w^*_f + \left(\cos\theta_{ca,PDMS} + \cos\theta_{ca,glass}\right)\big/ h\right)$ for forward or $P_{diode,bw} = -\sigma \times \left(2\cos\left(\pi - \theta^*_{mb}\right)\big/ w^*_b + \left(\cos\theta_{cr,PDMS} + \cos\theta_{cr,glass}\right)\big/ h\right)$ for backward flowing. σ is the surface tension (J.m^{-1}), h is the diode height (m), θ^*_{mf} and θ^*_{mb} are the meniscus angles (°) on the surface of a polydimethylsiloxane (PDMS) replica at the moment of forward and backward bursting, respectively, and w^*_f and w^*_b are the meniscus widths (m) at the moment of forward and backward bursting, respectively.

Flowing After bursting, liquid is assumed in a Stokes flow region due to a low Reynolds number (maximum Re < 0.3 from experiments), the flow rates of the diodes are equated as:

$$Q = \begin{cases} \left(\Delta P - P_{ch,fw}\right)\big/ R_{fw} & \left(if\ \Delta P > P_{diode,fw}\right) \\ 0 & \left(if\ P_{diode,fw} \geq \Delta P \geq P_{diode,bw}\right), \\ \left(\Delta P - P_{ch,bw}\right)\big/ R_{bw} & \left(if\ P_{diode,bw} > \Delta P\right) \end{cases} \tag{2.17}$$

where $R_{fw} = R_{ch,fw} + R_{diode}$ and $R_{bw} = R_{ch,bw} + 3R_{LV}$ are the total flow resistances in forward and backward directions, and $R_{ch,fw}$, $R_{ch,bw}$, R_{diode}, and R_{LV} are the flow resistances of the straight channel in forward and backward directions, a bidirectional fluidic diode, and a limiting valve, respectively. Contrary to the forward flow that passes single diode, the backward flow encounters three limiting valves that create a higher resistance in the backward direction. When the diode bursts, it is unlikely for the liquid around the meniscus to be considered within the Stokes flow region and, therefore, it is compensated by including the surface tension exerted on the meniscus flowing along the straight channel (forward: $P_{ch,fw}$ or backward: $P_{ch,bw}$). The values of the constants are provided in Table 2.1.

Meniscus angle On one hand, ideally sharp-edged bidirectional fluidic diode burst when the meniscus angle, θ^*_{mf}, reaches the lower value of either $\beta + \theta_{ca,PDMS}$ or π (denoted as "$\min(\beta + \theta_{ca,PDMS},\ \pi)$"), or when θ^*_{mb} reaches $\min(\pi + \beta - \theta_{cr,PDMS},\ \pi)$, for a forward or backward direction, respectively. Both meniscus widths, w^*_f and w^*_b, are the same as the diode width, w_o. On the other hand, a fabricated round-edged bidirectional fluidic diode with a radius of curvature r_e, bursts when the meniscus contact angle θ^*_{mf}, is $\min(\theta^*_{ef} + \theta_{ca,PDMS},\ \pi)$ or θ^*_{mb} is $\min(\pi + \theta^*_{eb} - \theta_{cr,PDMS},\ \pi)$, which is smaller than that of an ideally sharp-edged diode (since $\theta^*_{ef} \leq \beta$ and $\theta^*_{eb} \leq \beta$). The meniscus width at a fabricated round diode become wider and is defined as: $w^*_f = w_o + 2r_e \times \left(1 - \cos\left(\theta^*_{ef}\right)\right)$ or $w^*_b = w_o + 2r_e \times \left(1 - \cos\left(\theta^*_{eb}\right)\right)$, for a forward or backward direction, respectively.

Design of two diodes The fluidic diodes are differentiated as either uni-directional or bi-directional diodes depending on the edge angle of the diodes (Fig. 2.5, A and B, respectively), which determine the bursting pressures at either side of the diodes and, thus, control the flow direction under certain operational pressures. For example, uni-directional bidirectional fluidic diodes burst at lower operational pressure in a certain direction because it is designed with a dull edged-structure on one side, which creates a low bursting pressure in that one direction; whereas, bi-directional diodes holds the meniscus in both directions under the same high bursting pressure.

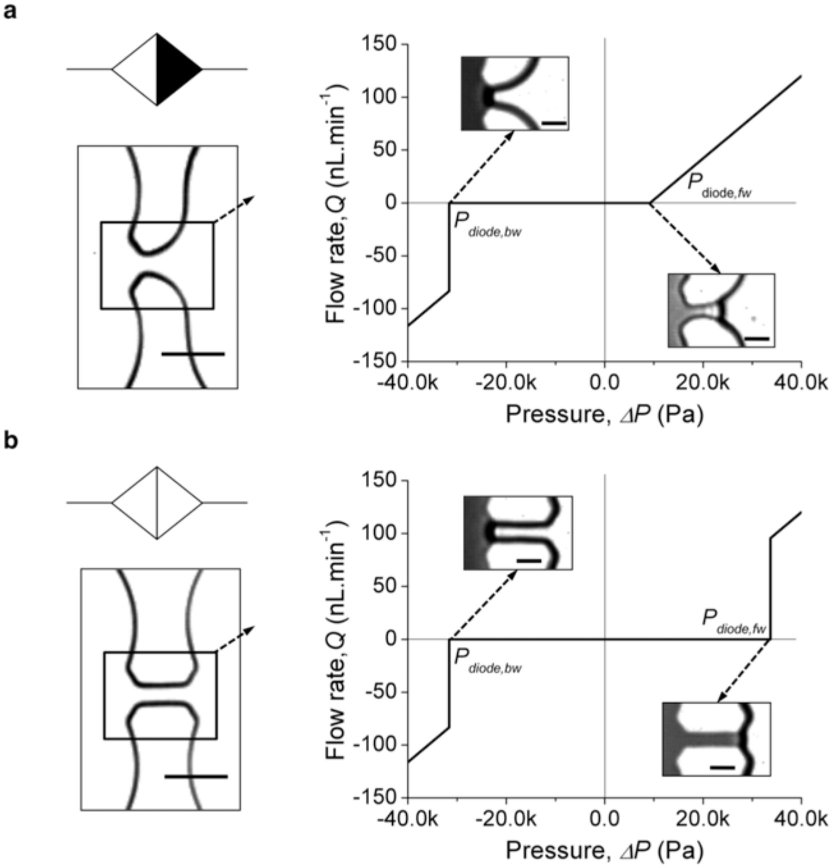

Figure 2.5 Photos and characteristic curves of uni-directional (A) and bi-directional (B) bidirectional fluidic diodes are shown. The uni-directional diode provides a high bursting pressure only in a backward direction where a sharp edge is designed and the bi-directional diode provides the high bursting pressure in both directions. Scale bars are 5 μm.

Device Fabrication A negative photoresist, SU-8 2000.5 (MicroChem, Newton, MA), was spin-coated at 3000 rpm for 30 seconds to create a 500 nm thickness on a piranha-cleaned 4” silicon wafer and patterned using standard lithography (Karl Suss MA6 Mask Aligner, SUSS Microtech, Waterbury, VT) with UV light (365 nm, 5.4 mJ.cm^{-2}, 90 % recommend exposure energy) in ‘hard contact mode’ to reduce the diffraction effect (Fig. 2.6A). The patterned wafer was dry-etched by a deep reactive ion etching (DRIE) process using an anisotropic plasma etching system (Multiplex ICP, Surface Technology Systems, Newport, UK) in a low frequency mode (33%

duty cycle, 15 ms period, 2 minutes) to fabricate a silicon structure with 6.1 μm thickness (Fig. 2.6B). The photoresist was removed through an ashing process using an isotropic plasma etching system (PE-II A, Technics West Inc., Danville, CA) by O_2 at a flow rate of 51.1 sccm (300 W, 7 minutes) (Fig. 2.6C). To avoid the PDMS replica from sticking to the silicon surface, the surface was coated with a FOTS monolayer (fluorinated organosilane) using a molecular vapor deposition system (MVD 100, Applied MicroStructures, San Jose, CA) (Fig. 2.6D). As a result, permanently reusable silicon mold was fabricated (Fig. 2.6E). A mixture of a base and a curing agent with a 10:1 weight ratio (SYLGARD 184 A/B, Dowcorning, Midland, MI) was poured onto the silicon mold (Fig. 2.6F). This was cured for 1 hour at room temperature under vacuum to remove bubbles and, subsequently, cured again for 2 days in ambient pressure at room temperature, 20°C. A cured PDMS replica was peeled off from the mold (Fig. 2.6G) and punched for inlet and outlet connections (Fig. 2.6H).

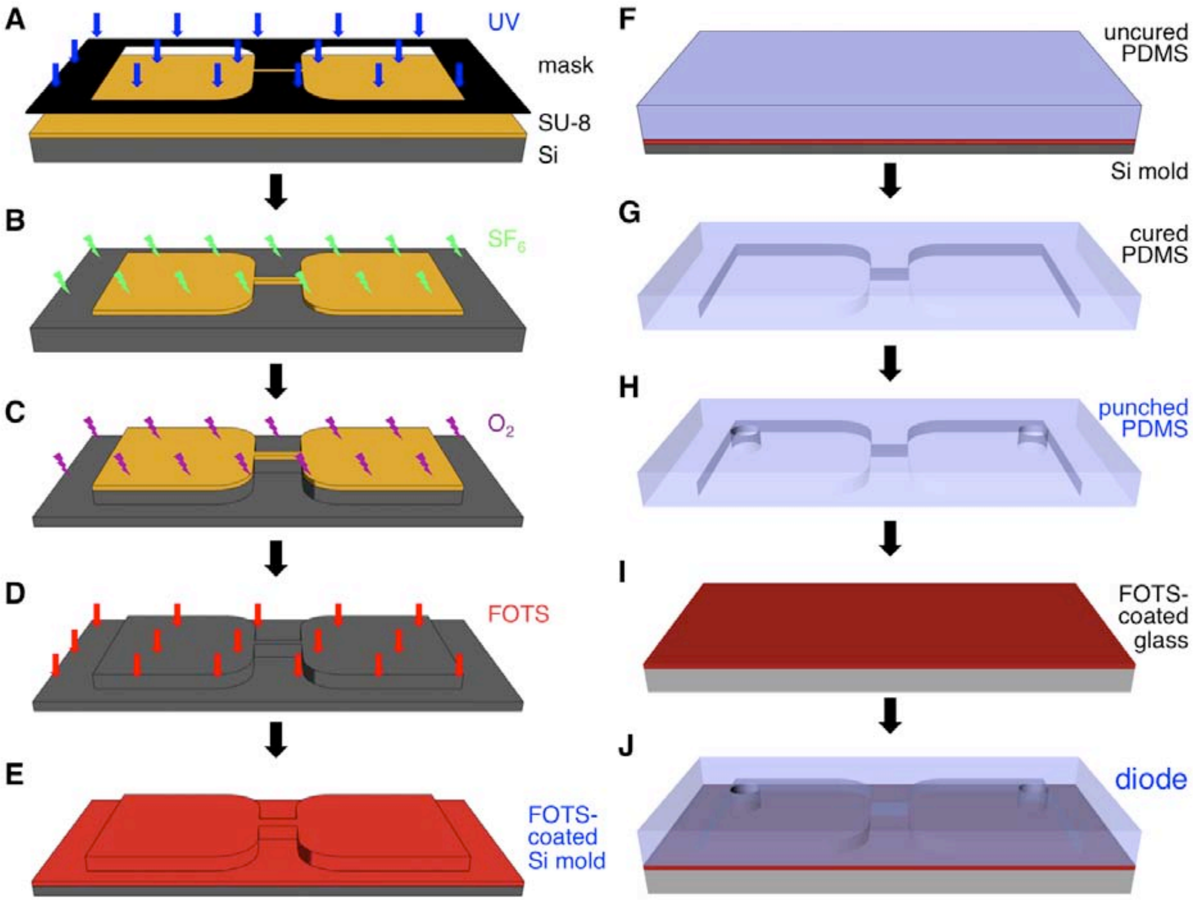

Figure 2.6 Fabrication steps for the bidirectional fluidic diode. **(A)** A thin SU-8 (0.5 μm thickness) is patterned on a 4” silicon water by standard lithography. **(B)** The wafer is etched with DRIE to form the features of the mold. **(C)** SU-8 mask is removed by oxygen plasma ashing. **(D-E)** The wafer mold is coated via vapor with FOTS to avoid PDMS from sticking to the mold. **(F-H)** A PDMS replica is fabricated through mold replication and hole punching. **(I)** A glass slide is coated via vapor with FOTS to create a hydrophobic condition. **(J)** Both the PDMS replica and the FOTS-coated glass are treated with UVO and are contacted for bonding.

A piranha-cleaned glass surface was coated with a FOTS monolayer to create a hydrophobic surface (Fig. 2.6I). For bonding, both of the PDMS replica and the FOTS-coated-glass surfaces were exposed to UV/Ozone treatment (UVO Cleaner Model 42, Jelight, Irvine, CA) for 3 minutes. After contacting them, the bonded devices were incubated in an oven at 60 °C for more than 4 days to fully recover the hydrophobic surfaces (Fig. 2.6J).

Experimental setup Characterization of the bidirectional fluidic diode and demonstration of lettering were conducted with an integrated experimental setup: a pressure/vacuum pump, a temperature-compensated pressure sensor, a high-speed CCD camera, a color CCD camera, and a microscope. The pump could provide regulated pressure difference from 0.7 MPa to -0.1 MPa (PV830, Pneumatic PicoPump, WPI Ltd., Stevenage, UK). The supplied pressure was accurately measured at a resolution of 50 Pa using the sensor (15 PSI-D1-4V-MINI, All Sensor, Morgan Hill, CA) fixed right next to the outlet reservoir. The HS-CCD camera (HS-CCD, TroubleShooter, Fastec Imaging, San Diego, CA) took a series of images to create movies (frame rate up to 1000 Hz), and the counting of frame numbers was used for flow-rate calculation. The normal-speed color CCD camera (QColor3, Olympus America Inc., Center Valley, PA) took color images for letter patterning in two colors.

Experimental Protocol The bidirectional fluidic diodes were characterized by monitoring the meniscus of a color dye that was filtered by a syringe filter (PALL Acrodisc 32mm, 0.2 μm Supor Membrane, PALL Life Science, Port Washington, NY) and diluted by 2 times in deionized water. The characterization of the diodes was assessed in forward and backward flow directions by applying negative and positive pressure difference to an outlet reservoir, respectively. Firs, 5 μL of dye was dropped into an inlet reservoir via pipette, and then a weak negative pressure difference of -5.8 kPa was applied to the outlet reservoir to pull the liquid dye through the arrayed straight channels until the meniscus in each channel was pinned at the diodes. To obtain characterization values (bursting pressure and flow rate) for the forward directional flow, negative pressure was gradually applied to create positive pressure difference ranging from 0 to 40 kPa by increments of 0.5 kPa. Likewise, to obtain characterization values for the backward directional flow, positive pressure was gradually applied to create negative pressure difference ranging from 0 to -40 kPa by increments of 0.5 kPa. After each increment of applied pressure, in which the dye-meniscus "burst" through the diode, the pressure sensor reads this bursting pressure. During this process when the meniscus burst through the diodes and flowed through the straight channel, the HS-CCD records a series of images at 125 frames per second. In following, instant pressure was applied in the opposing direction for meniscus realignment to the diode. The flow velocity was calculated by counting the number of frames for the meniscus to flow 1mm along the straight channel following the diode. To quantitatively evaluate the bursting pressure of the bidirectional fluidic diode, we varied diode width (w_o) from 1.7 to 9.0 μm while fixing the diode angle at 110°. The PDMS replica showed that the replicated diode width was smaller than that of a silicon mold due to the shrinkage of PDMS during the curing process. As predicted, higher bursting pressures were obtained for diodes having smaller width, ranging from 10 to 35 kPa, with a bursting flow rate of 25 to 100 nL.min^{-1} in the forward direction, and -10 to -35 kPa, with a bursting flow rate of 0 to -50 nL.min^{-1} in the backward direction. Also, the flow rates increased linearly with applied operational pressure after bursting.

2.4 CHARACTERIZATION

Experimental Validation To validate the analytical model on diodes, we compared the numerical and experimental bursting pressures at the diodes and flow rates in the following straight channel, while varying the input variables: width (Fig. 2.7) and edge angle (Fig. 2.8) of diodes, and the straight channel width (Fig. 2.9).

As predicted, higher bursting pressures were obtained for diodes having smaller width, ranging from 10 to 35 kPa, with a bursting flow rate of 25 to 100 nL.min^{-1} in the forward direction, and -10 to -35 kPa, with a bursting flow rate of 0 to -50 nL.min^{-1} in the backward direction (Fig. 2.7).

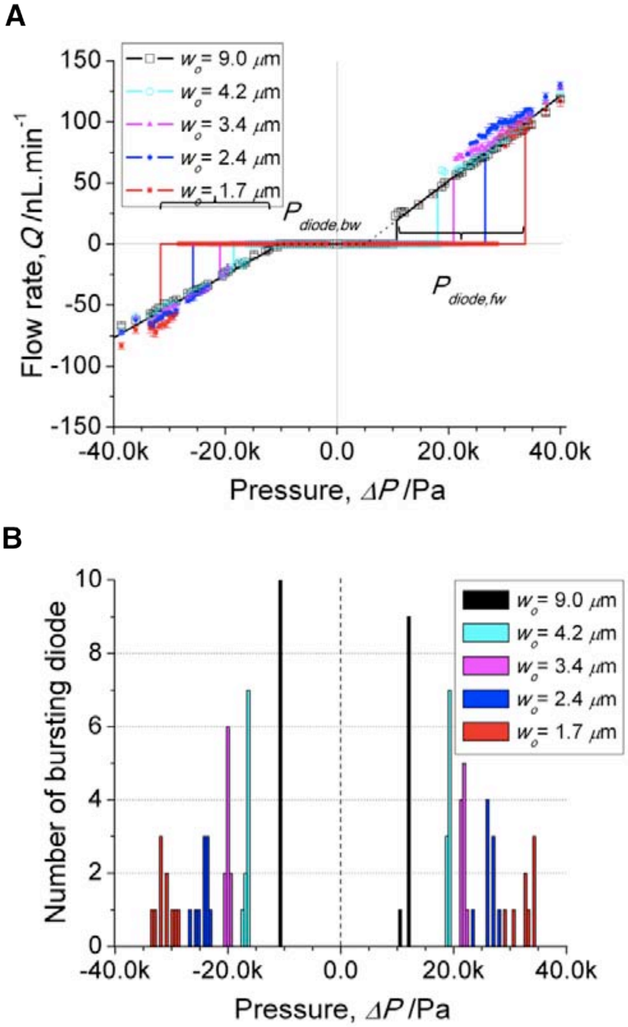

Figure 2.7 With variation of diode width (w_o), estimated bursting pressures and flow rates are represented in lines (A), and experimental results are plotted with averaged values and corresponding standard deviations (A). Narrow distribution of the bursting pressures is observed by presenting the number of bursting diodes at the minimum bursting pressures in bar graphs (B).

To further assess the bursting pressure of the bidirectional fluidic diode, we also varied the diode angle (β) from 30 to 110° while fixing the diode width at 1.7 μm (Fig. 2.8). The PDMS replica showed that the fabricated diodes had rounded edges caused by a diffraction effect during the standard lithography process. As estimated, higher bursting pressures were obtained for sharper diodes, ranging from 20 to 35 kPa, with a bursting flow rate of 30 to 100 nL.min^{-1}, in the forward direction and -20 to -35 kPa, with a bursting flow rate of -25 to -75 nL.min^{-1}, in the backward direction.

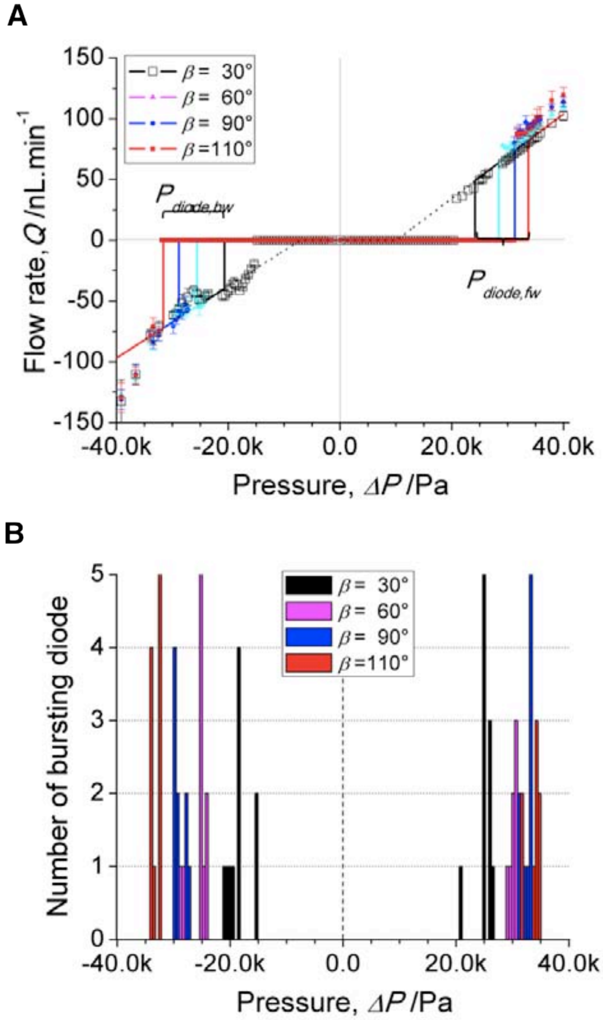

Figure 2.8 With variation of diode angle (β), estimated bursting pressures and flow rates are represented in lines (A), and experimental results are plotted with averaged values and corresponding standard deviations (A). Narrow distribution of the bursting pressures is observed by presenting the number of bursting diodes at the minimum bursting pressures in bar graphs (B).

To characterize the flow rate of liquid after it bursts at the bidirectional fluidic diodes, we varied the straight channel widths (w_1) from 10 to 50 μm to vary the resistances while fixing the diode angle at 110° and diode width at 1.7 μm (Fig. 2.9). As expected, the flow rates increased (or resistance decreased) with increasing channel width, ranging from 25 to 150 nL.min^{-1} and -15 to -120 nL.min^{-1} under operational pressures of 30 to 40 and -30 to -40 kPa, respectively. Also, surface tension on the straight channel decreased with increasing channel width.

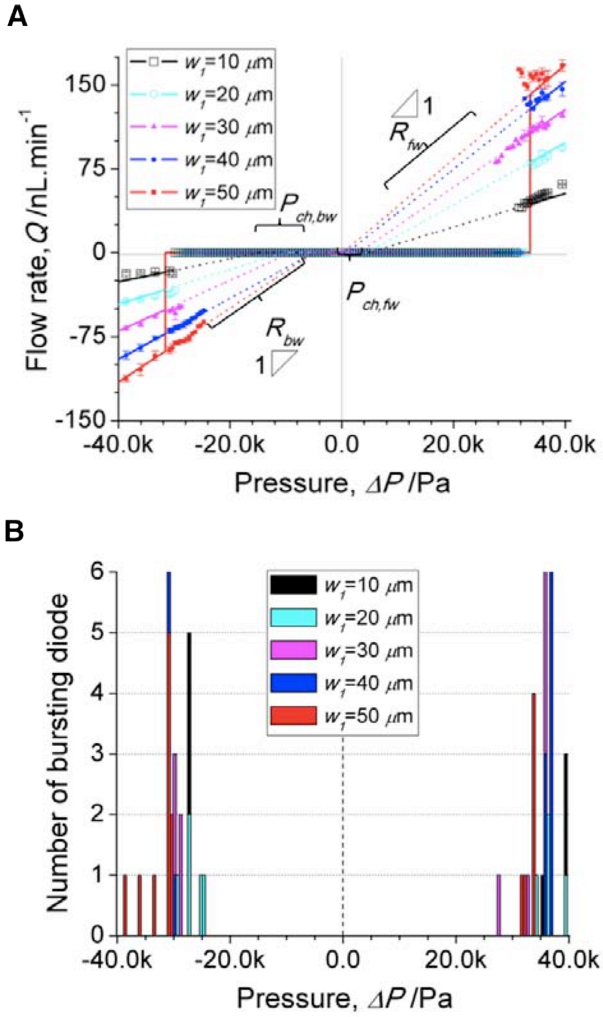

Figure 2.9 With variation of channel width (w_1), estimated bursting pressures and flow rates are represented in lines (A), and experimental results are plotted with averaged values and corresponding standard deviations (A). Narrow distribution of the bursting pressures is observed by presenting the number of bursting diodes at the minimum bursting pressures in bar graphs (B).

Analysis of xylems The proposed model was further applied to understand xylem embolism, and the calculated values were compared with measured values in real plant systems (Fig. 2.10). Bursting pressures and flow rates for embolism spreading and repair were calculated while varying the contact angle (Fig. 2.10 A) and pore diameter (Fig. 2.10 B), using previously measured dimensions.[15, 17, 25, 27, 28] The calculated gas-seeding pressure, a bursting pressure for embolism spreading, ranged from -2.8 to -2.6 MPa, and the pressure during the refilling process, ranged from -0.13 to -0.10 MPa, which were comparably similar to the experimentally measured pressures (-11.3 to -0.2 MPa for seeding pressure and -0.3 to -0.1 MPa for refilling pressure[15, 17]). Additionally, McElone *et. al.* reported that trees with xylella fastidiosa (Xf), a xylem-infecting bacterial pathogen that enlarged the pore size by three times, had 3.7 times higher embolism than in healthy trees.[28] According to our analytical model, the bursting pressure of an Xf-infected plant having 3 times larger pores (diameter of 900 nm; contact angle of 48°) was calculated to be

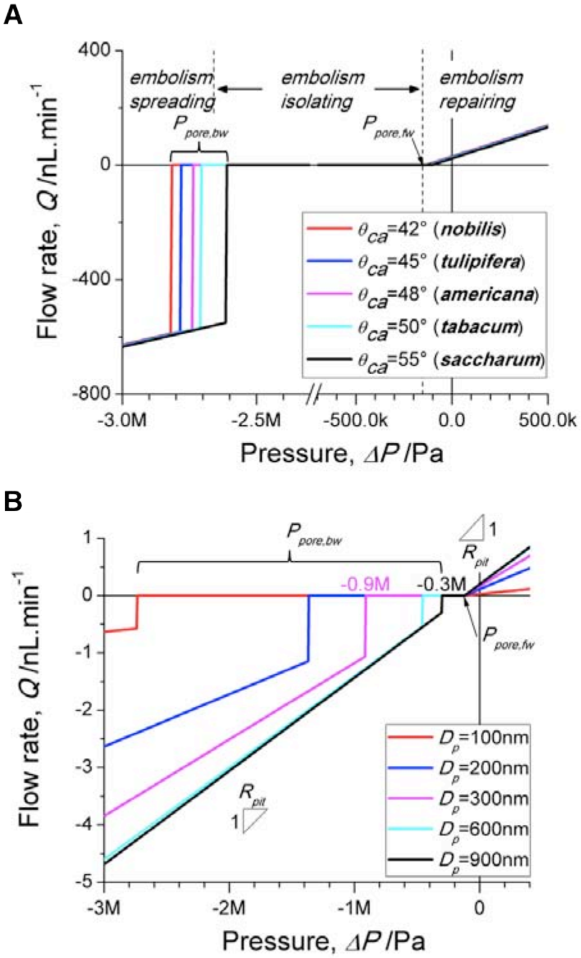

Figure 2.10 Estimated water pressure during embolism progression based on the mathematical model. The mathematical model of the bidirectional fluidic diode is applied to estimate the pressure difference across a pit membrane, as well as the flow rate through the membrane, while varying static contact angle (A) and pore diameter (B). Embolism spreading is avoided until xylem pressure reaches down to negative pressures, ranging from -2.8 to -2.6 MPa, while embolism repair is expected to occur spontaneously above a negative pressure, ranging from -0.13 to -0.10 MPa, with the variation of contact angle from 42 to 55° at pore diameter of 100 nm. Embolism spreading is expected to be three times higher (or, in other words, occurs at three times weaker negative pressure) in Xf-infected plants that have larger pores (D_p= 900 nm) than healthy plants (D_p= 300 nm), which corresponds to the experimental observation.

lower than that of healthy plants (diameter of 300 nm; contact angle of 48°) by about 3 times, which agreed quite closely with the actual measurements. The values of the constants used for the numerical calculation is summarized in Table 2.2.

Lettering Using the microfluidic circuit of bidirectional fluidic diode arrays, we accomplished a self-patterning fluidic network. We designed a droplet chamber equipped with eight different microfluidic diodes on each side, in which each type of diodes regulated the flow direction. Ultimately, we designed a microfluidic circuit composed of the arrayed droplet chambers that utilized the designed uni- and bi-directional diodes to form self-patterned letters.[29]

The lettering involves two steps: liquid-filling with forward flow and liquid-removal with backward flow. Firstly, under a positive operational pressure ($\Delta P = P_l - P_g > 0$), liquid filled the chambers in the forward direction by passing through uni-directional diodes with low forward bursting pressure. However, the meniscus was pinned at bi-directional diodes, as well as at uni-directional diodes with a high forward bursting pressure (Fig. 2.11, A - C, b). Secondly, under a negative operational pressure ($\Delta P = P_l - P_g < 0$), only the meniscus at the uni-directional diodes with low backward bursting pressure were released and flowed in the reverse direction, resulting in the removal of liquid in unselected chambers (Fig. 2.11, A – C, c). However, the meniscus pinned at the bi-directional diodes, as well as uni-directional diodes with a high backward bursting pressure, maintained their pinning status in “selected” chambers, ultimately resulting in the patterning of droplets in selective, “letter-forming” chambers (Fig. 2.11, A – C, d). These steps were illustrated in zoomed-in schematic representations (Fig. 2.11A), zoomed-in views of photos (Fig. 2.11B), and zoomed-out views of photos (Fig. 2.11C). In addition, the lettering was done with two different color dyes, demonstrating multiplex patterning (Fig. 2.11D). Moreover, it may be important to note that meniscus-pinning failed under an excessive positive operational pressure that exceeded the high bursting pressure of all bidirectional fluidic diode types.

Aging effect Furthermore, we evaluated the effect of contact angle change over time on bursting pressures.[30] The dramatic decrease in contact angle on a FOTS-coated glass surface was observed right after UV/Ozone treatment, and the angle increased (or “recovered”) steadily over time after the treatment (Fig. 2.12). Right after the treatment, the contact angle with water became less than 10° from the original 90°, requiring more than 4 days for a full recovery. Under higher temperature, the angle recovery was faster and the saturated angle was higher. As a result, the diodes with a shorter recovery time had a lower bursting pressure. For consistency in experimental conditions, all devices were stored in a 60 °C oven for more than 4 days before experimentation to confirm fully recovered surface conditions. The surface tension of a dye was measured using a tentiometer (Sigma 701, KSV Instruments Oy, Helsinki, Finland).

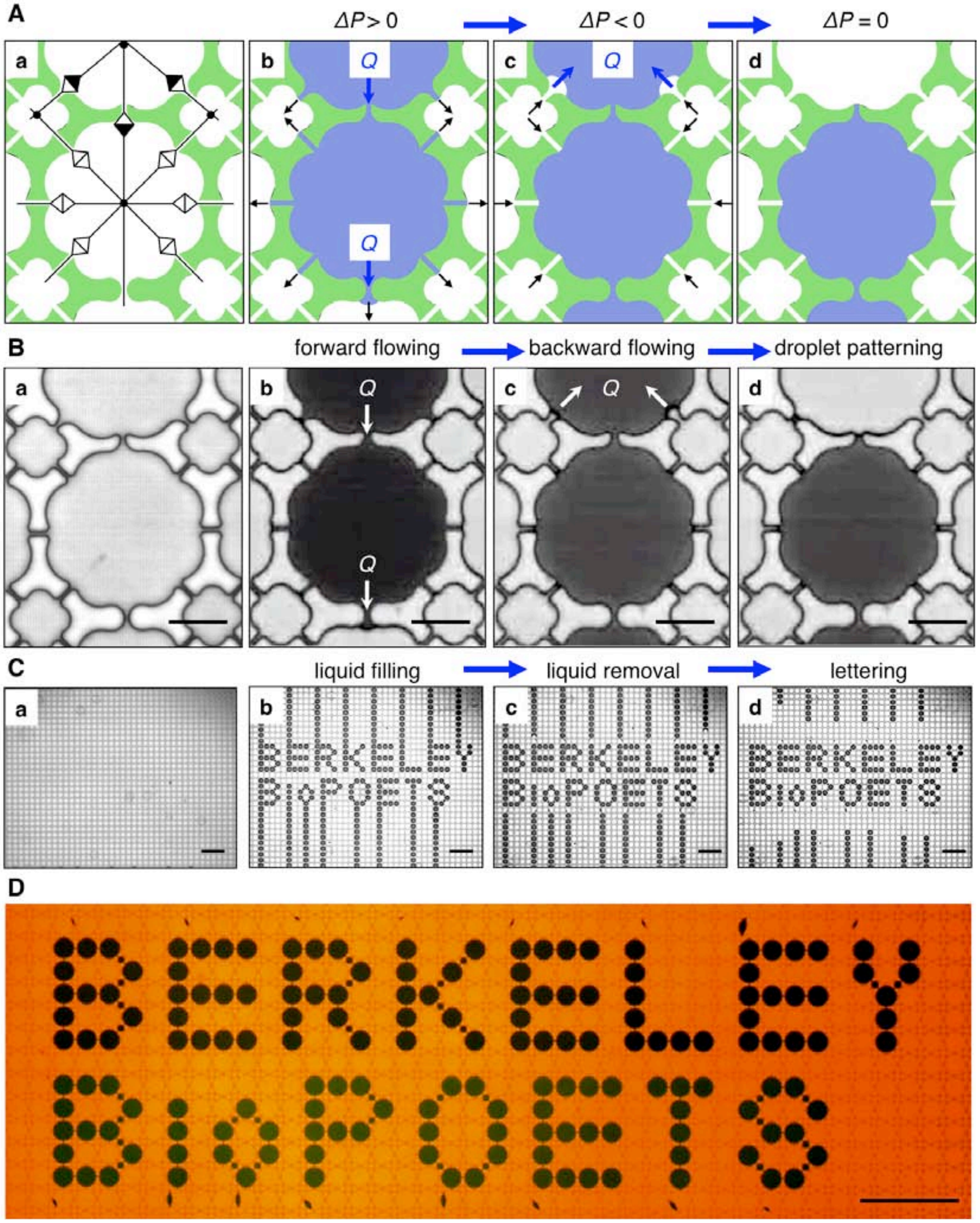

Figure 2.11 Self-patterning fluidic network by uni- and bi-directional fluidic diodes. (A - C) Each letter chamber is designed with eight different bidirectional fluidic diodes, making the letter chambers equivalent to an electric circuit with eight electric diodes (a). Lettering is accomplished through two steps: forward flow to fill letter chambers under a positive-operational pressure (b) and backward flow to remove liquid from unselected chambers under negative-operational pressure (c), ultimately achieving droplet patterning to form letters (d), as seen in the schematics (A), and photos of zoomed-in (B) and zoomed-out views of arrayed letter chambers (C). **(D)** A photo shows letters composed of droplets in two different colors of blue (upper row) and green (lower row). Scale bars are 30 μm (B) and 300 μm (C and D), respectively.

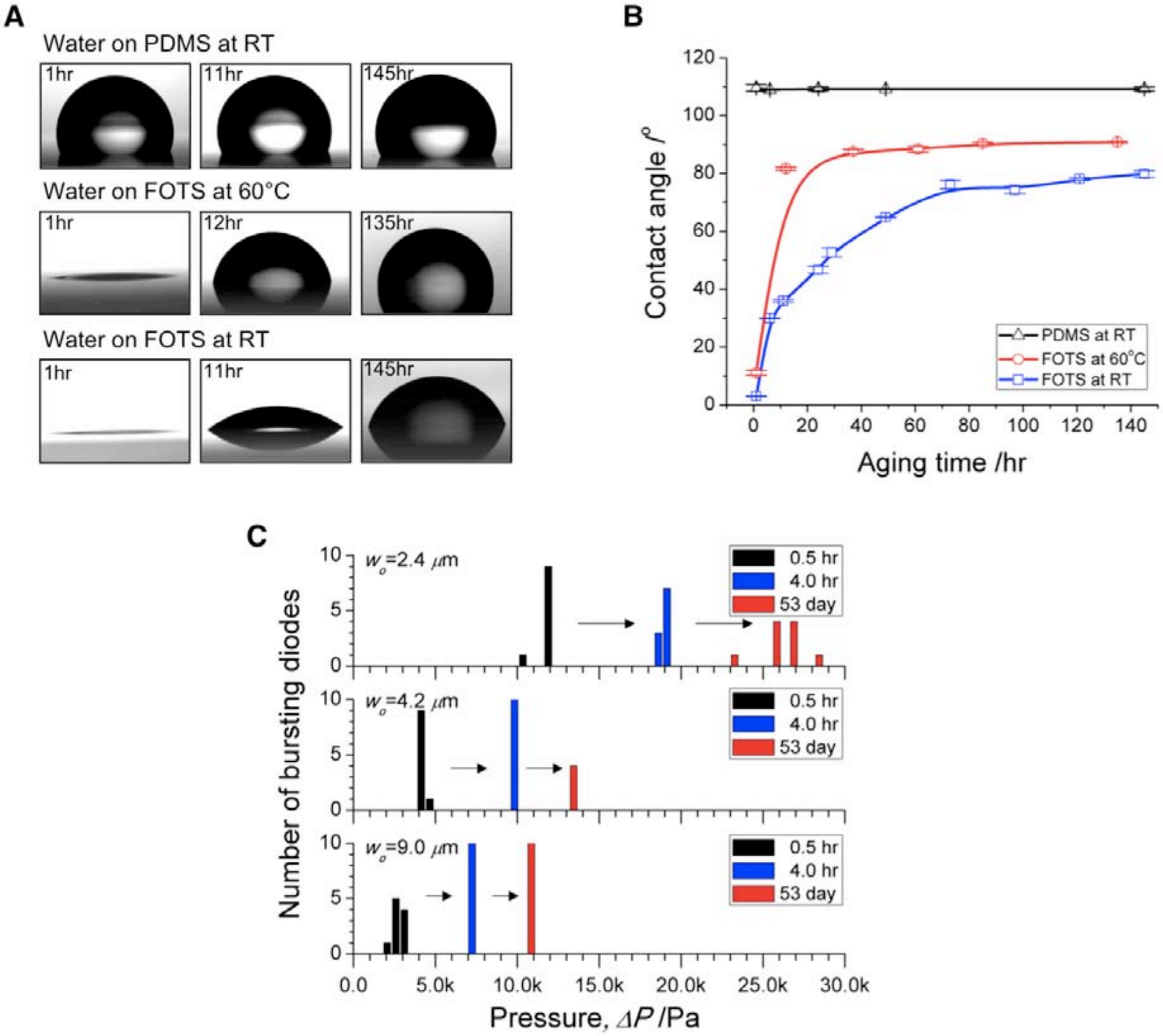

Figure 2.12 Characterization on contact angle recovery of a FOTS-coated glass and PDMS surfaces with time after UVO treatment. (A) Photos show static contact angles of water droplets on PDMS and FOTS-coated glass surfaces treated with UVO for 3 minutes, followed by an aging process at room temperature (20 °C) and in an oven (60 °C). **(B)** The curves show that the contact angle recovers with time and saturates after more than 4 days of aging time in all cases, in which faster and higher recovery is observed at higher temperature on FOTS-coated glass surfaces. **(C)** The bursting pressure of a dye increases with time, as represented by the increase in contact angles.

Reservoir effect Also, we assessed the effect of an outlet reservoir deflection on flow rates. The reservoir deflection was observed in the outlet under a strong positive operational pressure (more than 20 kPa). Due to the increase in resistance caused by the reservoir deflection, the flow rate was observed to gradually decrease, losing its linear relationship with the applied operational pressure (Fig. 2.13). After the experiments, the measured flow rates were adjusted to compensate the effect from the reservoir deflection that occurred at strong positive operational pressures.

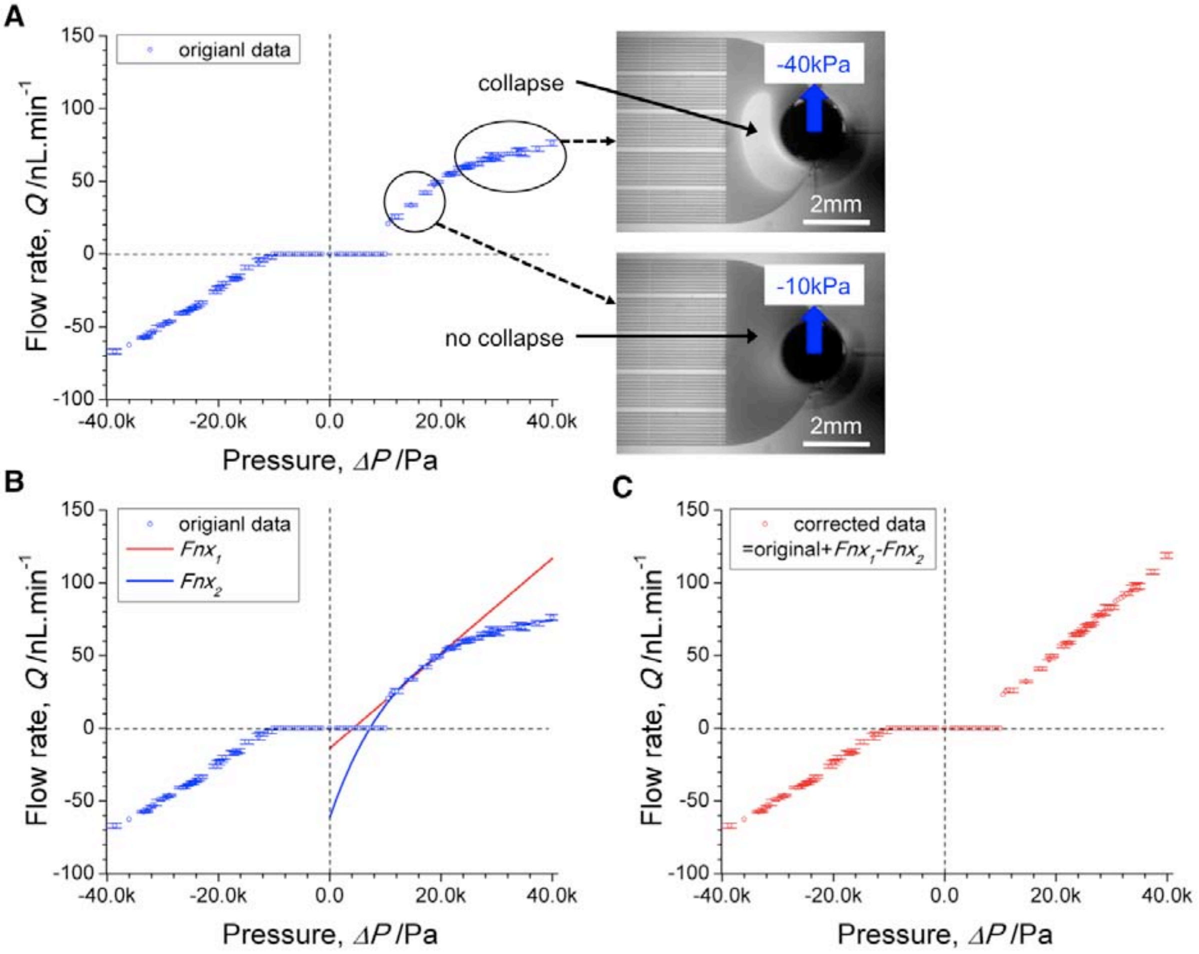

Figure 2.13 Compensating the effect of a collapsed outlet reservoir. (A) Collapse outlet reservoir and low flow rates are observed when strong negative vacuum is applied to a soft PDMS reservoir. **(B)** A straight line (*Fnx1*) and an exponential curve (*Fnx1*) are created by fitting the measured original data ranging from 10 to 20 kPa and 10 to 40 kPa, respectively. **(C)** The original data are compensated by adding to it the difference between *Fnx1* and *Fnx2*.

Characterizations of the bidirectional fluidic diode The dimensions of the diodes were measured by analyzing their bright field images. Images of a mask (Fig. 2.14A) and a PDMS replica (Fig. 2.14D) were taken using a transmitted microscope with a magnification lens of 100X (CP-ACHROMAT, N/A. 1.25, Oil iris, ZEISS, Germany). Images of a photoresist pattern (Fig. 2.14B) and a silicon mold (Fig. 2.14C) were taken using an inverted microscope with a magnification lens of 100X (CF-Plan, N/A 0.90, Nikon Instrument Inc., Melville, NY). The height of diodes in a PDMS replica was assumed to be the same as that of the silicon mold, which was measured by a mechanical, stylus-based step profiler (Alpha-Step IQ Surface Profiler, KLA Tencor, Milpitas, CA).

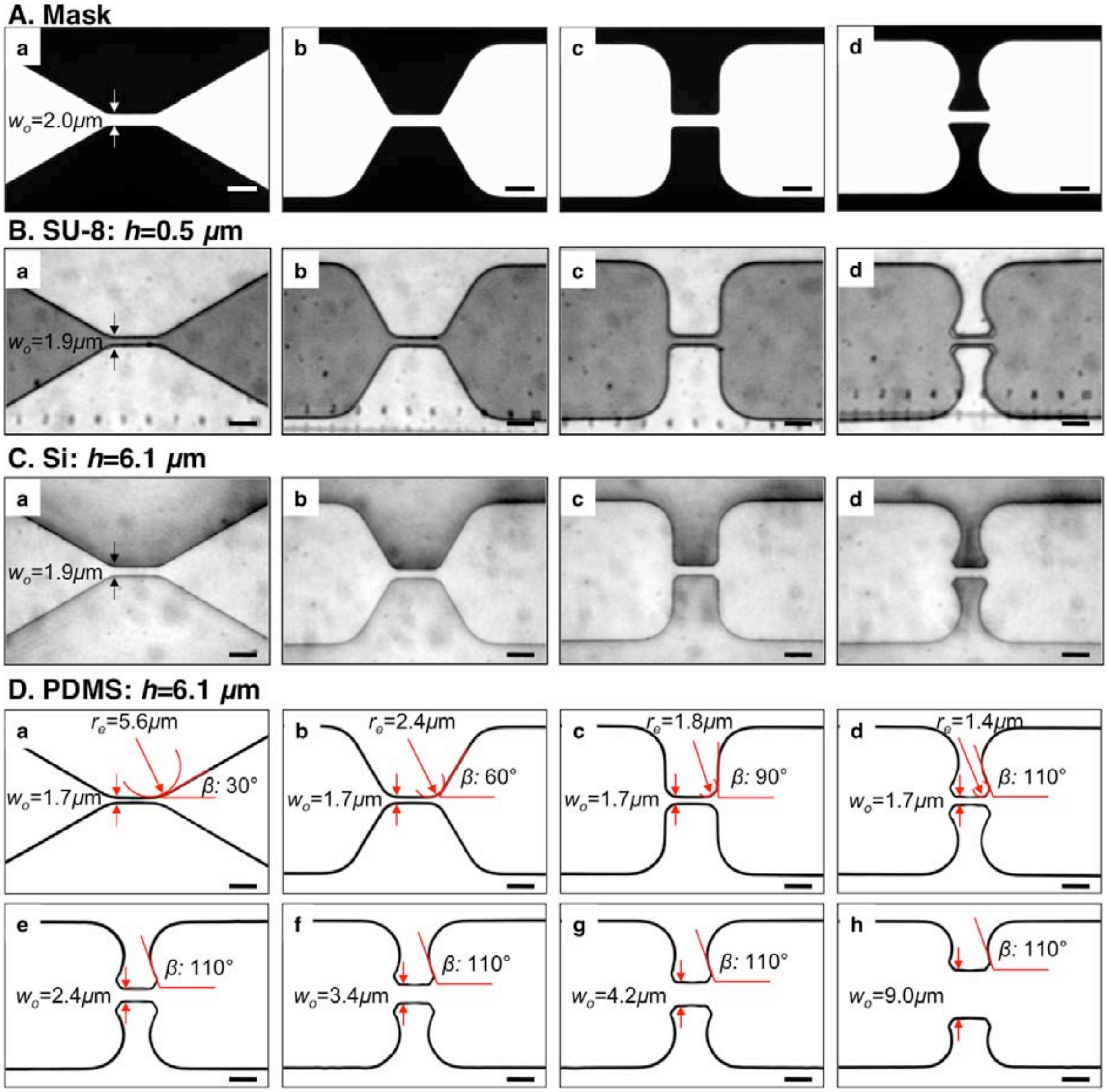

Figure 2.14 Characterizations of bidirectional fluidic diode. Photos show the diode in a mask (A), a negative photoresist, SU-8 (B), an etched silicon mold (C), and a PDMS replica (D) with variation of (a-d) angle and (e-h) width of the diodes. Rounded corners are observed in the SU-8 pattern most likely due to the diffraction effect during fabrication at the sharp corners. Diode width, 'w_o', in the PDMS replica is smaller than that in the mask most likely due to PDMS shrinkage. Scale bars are 5 μm.

Surface Energy Characterizations by Contact Angle Measurements The contact angles were measured using a contact angle measurement system (DSA10-Mk2, KRÜSS GmbH, Hamburg, Germany) with a 'height-width fitting' method. Dynamic (advancing and receding) contact angles of a liquid dye were measured by capturing images of droplets at 25 frames per second while adding and removing liquid, respectively (Fig. 2.15).

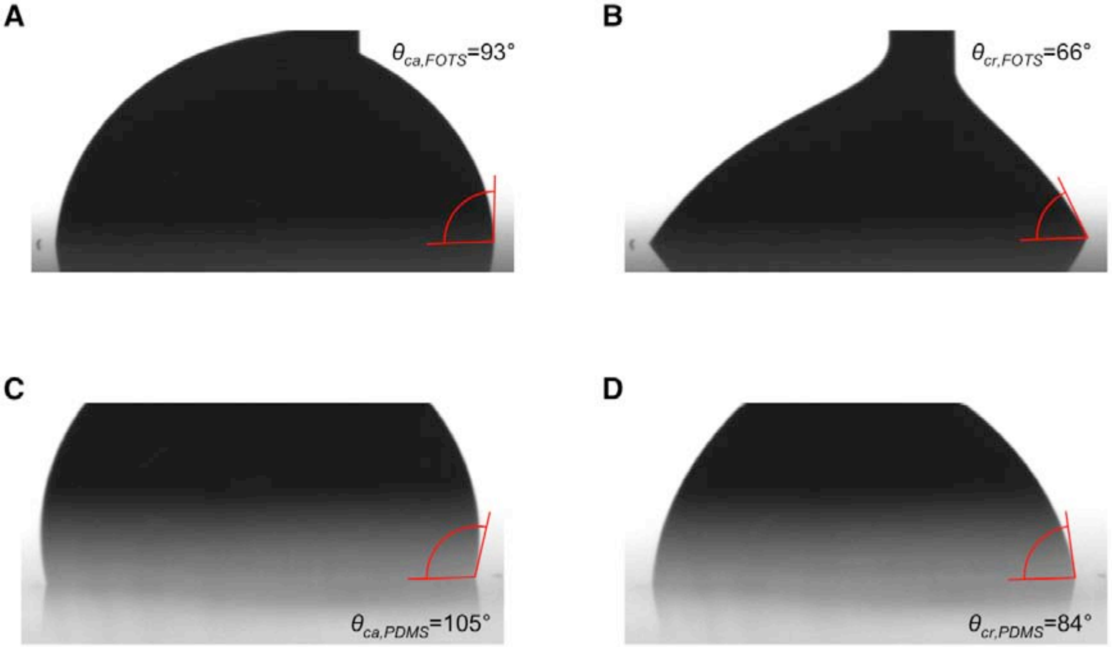

Figure 2.15 Measurement of dynamic contact angles of dye on FOTS-coated glass and PDMS surfaces. Photos show advancing (A and C) and receding (B and D) contact angles of dye on FOTS-coated glass surfaces (A and B) and PDMS surfaces (C and D) aged in an oven (60 °C) for more than 4 days after 3 minutes of UVO treatment.

2.5 CONCLUSIONS

The understanding of water flow through xylem pores on an inter-conduit pit membrane in xylems has inspired the development of bidirectional fluidic diodes that could uni- or bi-directionally regulate liquid flow upon structural design. The constructed analytical model could provide a guideline for the design of microfluidic circuits, as well as a method to understand the mechanism behind water transport in plants. The utility of the single-layered bidirectional fluidic diodes was successfully demonstrated by selective patterning in the well-organized arrayed microfluidic network. Furthermore, the novel bidirectional fluidic diodes would allow creating autonomous fluidic circuit controls in biotechnology and medicine.

References:

(1) Boncheva, M., Gracias, D. H., Jacobs, H. O., Whitesides, G. M., Biomimetic self-assembly of a functional asymmetrical electronic device, *Proceedings of the National Academy of Sciences of the United States of America* **2002**, 99 (8), 4937-4940.

(2) Lee, L. P., Szema, R., Inspirations from Biological Optics for Advanced Photonic Systems, *Science* **2005**, 310, 1148-1150.

(3) Jeong, K.-H., Kim, J., Lee, L. P., Biologically Inspired Artificial Compound Eyes, *Science* **2006**, 312 (5773), 557-561.

(4) Parker, A. R., Townley, H. E., Biomimetics of photonic nanostructures, *Nat. Nano*. **2007**, 2 (6), 347-353.

(5) Lee, H., Dellatore, S. M., Miller, W. M., Messersmith, P. B., Mussel-Inspired Surface Chemistry for Multifunctional Coatings, *Science* **2007**, 318, 426-430.

(6) Ingber, D., From Molecular Cell Engineering to Biologically Inspired Engineering, *Cellular and Molecular Bioengineering* **2008**, 1, 51-57.

(7) Pokroy, B., Epstein, A. K., Persson-Gulda, M. C. M., Aizenberg, J., Fabrication of Bioinspired Actuated Nanostructures with Arbitrary Geometry and Stiffness, *Adv. Mater.* **2009**, 21, 463-469.

(8) Lucas, W. J., Lee, J.-Y., Plasmodesmata as a supracellular control network in plant, *Nat. Rev. Mol. Cell. Biol.* **2004**, 5, 712-726.

(9) Molz, F. J., Kerns, D. V., Peterson, C. M., Dane, J. H., A Circuit Analog Model for Studying Quantitative Water Relations of Plant Tissues, *Plant Physiol.* **1979**, 64, 712-716.

(10) Pickard, W. F., The ascent of sap in plants, *Progress in Biophysics and Molecular Biology* **1982**, 37, 181-229.

(11) Holbrook, N. M., Burns, M. J., Field, C.B., Negative Xylem Pressures in Plants: A Test of the Balancing Pressure Technique, *Science* **1995**, 270 (5239), 1193-1194.

(12) Sperry, J. S., Tyree, M. T., Mechanism of Water Stress-Induced Xylem Embolism, *Plant Physiol.* **1988**, 88 (3), 581-587.

(13) Tyree, M. T., Sperry, J. S., Vulnerability of Xylem to Cavitation and Embolism, *Annual Review of Plant Physiology and Plant Molecular Biology* **1989**, 40 (1), 19-36.

(14) Hölttä, T., Vesala, T., Nikinmaa, E., A model of bubble growth leading to xylem conduit embolism, *Journal of Theoretical Biology* **2007**, 249 (1), 111-123.

(15) Sperry, J. S., Hacke, U. G., Analysis of circular bordered pit function I. Angiosperm vessels with homogenous pit membranes, *Am. J. Bot.* **2004**, 91 (3), 369-385.

(16) Hacke, U. G., Sperry, J. S., Pittermann, J., Analysis of circular bordered pit function II. Gymnosperm tracheids with torus-margo pit membranes, Am. J. Bot. 2004, 91 (3), 386-400.

(17) Zwieniecki, M. A., Holbrook, N. M., Bordered Pit Structure and Vessel Wall Surface Properties, Implications for Embolism Repair, *Plant Physiol.* **2000**, 123 (3), 1015-1020.

(18) Vesala, T., Holtta, T., Peramaki, M., Nikinmaa, E., Refilling of a Hydraulically Isolated Embolized Xylem Vessel: Model Calculations, *Ann. Bot.* **2003**, 91 (4), 419-428.

(19) Holbrook, N.M., Zwieniecki, M.A., Embolism Repair and Xylem Tension: Do We Need a Miracle?, *Plant Physiol.* **1999**, 120 (1), 7-10.

(20) Yang, S., Tyree, M. T., A theoretical model of hydraulic conductivity recovery from embolism with comparison to experimental data on Acer saccharum, *Plant, Cell and Environment* **1992**, 15 (6), 633-643.

(21) Holbrook, N. M., Ahrens, E. T., Burns, M. J., Zwieniecki, M. A., In Vivo Observation of Cavitation and Embolism Repair Using Magnetic Resonance Imaging, *Plant Physiol.* **2001**, 126 (1), 27-31.

(22) Côté, W. A. J., Day, A. C., Vestured pits—fine structure and apparent relationship with warts, *Technical Association of the Pulp and Paper Industry* **1962**, 45, 906–910.

(23) Choat, B., Brodie, T. W., Cobb, A. R., Zwieniecki, M. A., Holbrook, N. M., Direct measurements of intervessel pit membrane hydraulic resistance in two angiosperm tree species, *Am. J. Bot.* **2006**, 93 (7), 993-1000.

(24) Tio, K.-K., Sadhal, S. S., Boundary conditions for stokes flows near a porous membrane, *Applied Scientific Research* **1994**, 52, 1-20.

(25) Sperry, J. S., Hacke, U. G., Analysis of circular bordered pit function I. Angiosperm vessels with homogenous pit membranes, *Am. J. Bot.* **2004**, 91, 369-385.

(26) Cho, H., Kim, H.-Y., Kang, J. Y., Kim, T. S., How the capillary burst microvalve works, *Journal of Colloid and Interface Science* **2007**, 306 (2), 379-385.

(27) Petty, J. A., The Aspiration of Bordered Pits in Conifer Wood, *Proceedings of the Royal Society of London. Series B. Biological Sciences* **1972**, 181 (1065), 395-406.

(28) McElrone, A. J., Jackson, S., Habdas, P., Hydraulic disruption and passive migration by a bacterial pathogen in oak tree xylem, *J. Exp. Bot.* **2008**, 59 (10), 2649-2657.

(29) Huang, C. P. *et al.*, Engineering microscale cellular niches for three-dimensional multicellular co-cultures, *Lab on a Chip* **2009**, 9 (12), 1740-1748.

CHAPTER 3:
BIOLOGICALLY-INSPIRED 3D CO-CULTURING MICROFLUIDIC ARRAY: RECONSTRUCTING CANCER ANGIOGENESIS

A three-dimensional (3D) and co-culturing platform reconstructs *in vivo* cancer environment: clustered tumor cells adjacent to a 3D microvessel network for the study of angiogenesis triggered by insufficient nutrients and mediated with over-expressed growth factors. Cellular co-patterning is realized with pre-designed fluidic diodes, which can guide gel solutions in a large scale only requiring a single pump but no complicated tubing. Immediately after the patterning, cells are fixed in 3D gel solution by gelating in a culturing incubator at 37 °C for 30 minutes. The 3D co-patterning involves three steps: introducing gel solutions with tumor cells and endothelial cells to the platform, localizing tumor cells as designed by the fluidic diodes and fixating them in temperature-activated polymerized gel, and filling gaps with extra-cellular matrices. The concept of this co-patterning is verified by patterning multi-colored dyes representing different types of cells. The platform is applied to pattern breast cancer cells and human endothelial cells and shows the successful proliferation of each cell line by co-culturing them for 6 days. The platform has the capability of the systematic study by varying the inter-cellular distance, the size of clustered tumors, and the amount of nutrients in the culturing media in thousands of chambers. We envision that the developed co-culturing array will allow us to investigate the VEGF-mediated endothelial neovasculation in a systematic and efficient way.

3.1 INTRODUCTION

It is regarded that different physiological environments may trigger different cellular processes with respect to tumor biology, cell adhesion, migration, morphogenesis, and gene expression. Whereas malignant epithelial cells maintain their phenotypes while forming disorganized colonies within a 3D reconstituted basement membrane, the malignant phenotype was not shown in a two-dimensional (2D) culturing environment.[1] Also, the ability to elude pharmacological treatment was demonstrated by changing the migratory pattern of cancer cells from mesenchymal (spindle-shaped cells) to amoeboid (ellipsoid-shaped cells).[2] Culturing environment, in addition, can affect on cellular adhesion and migration mechanisms.[3] For instance, fibroblasts migration showed different shapes and distributions depending on adhesion proteins on a 2D substrate and composition of 3D extra-cellular matrix (ECM).[4] Moreover, it was shown that the ECM triggered different gene expression levels by affecting the 3D chromatin structure.[5] Furthermore, cell-to-cell communication is an essential physiological parameter for multicellular organisms. The billions of cells of a human or an oak tree must communicate in order to develop from a fertilized egg and then survive and reproduce in turn.

3.2 PRINCIPLES

Cell 3D culturing Even though cells are forming 3D environment inside living bodies, researchers are growing cells on 'petri dish' 2D environment *in vitro*. Contrary to spherical clustering or polarization formation in 3D, cells spread on the 2D surface, resulting in the significantly different morphology (Fig. 3.1). Therefore, it would be essential to provide 3D culturing *ex vivo* environment to predict physiologically relevant cellular responses of real organisms.

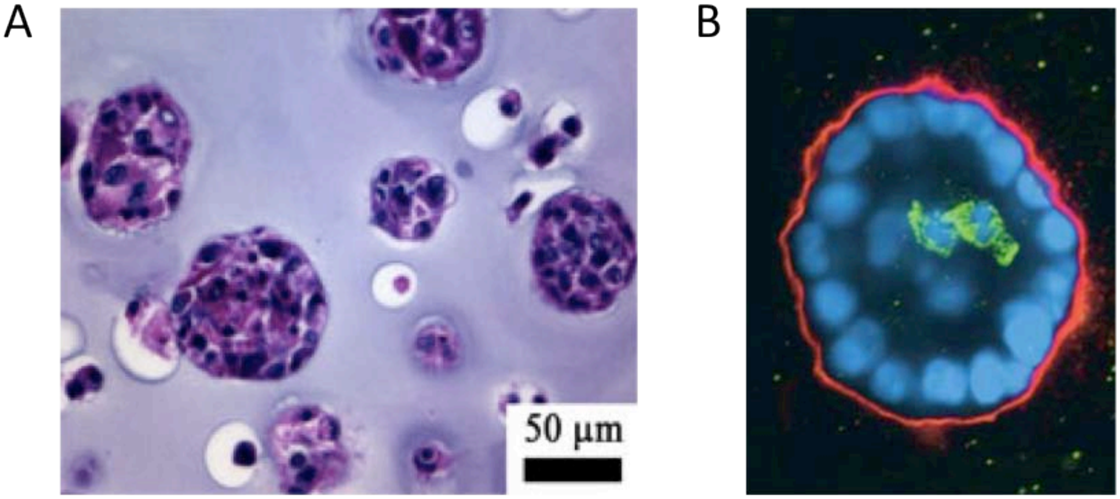

Figure 3.1 3D cell culturing *in vivo*. Fluorescent images of MDA-MD-231 cells grown in Extracel™-X hydrogel (A) and polarized mammary epithelial cell acini of 3-D cell culture (B)[6,7]. The cells in the center (green immunofluorescence) are undergoing normal programmed cell death (apoptosis) to form a hollow space.

Cell co-culturing Cell to cell communication is one of the major environments driving differentiation and development of cancer cells and stem cells. For example, throughout the entire process of cancer progression, malignant tumor cells induce neovascularization of endothelial cells by secreting stimulatory growth factors and cytokines; meanwhile the locally activated microenvironment of the host tissue (both cellular and extracellular elements) can be an active participant for proliferation and invasion of tumor cells (Fig. 3.2).[8] Invasion occurs within a tumour–host microenvironment, where stroma and tumour cells exchange enzymes and cytokines that modify the local extracellular matrix, stimulate migration, and promote proliferation and survival. Therefore, cell co-culturing is required to provide the physiological environment for cell communication.

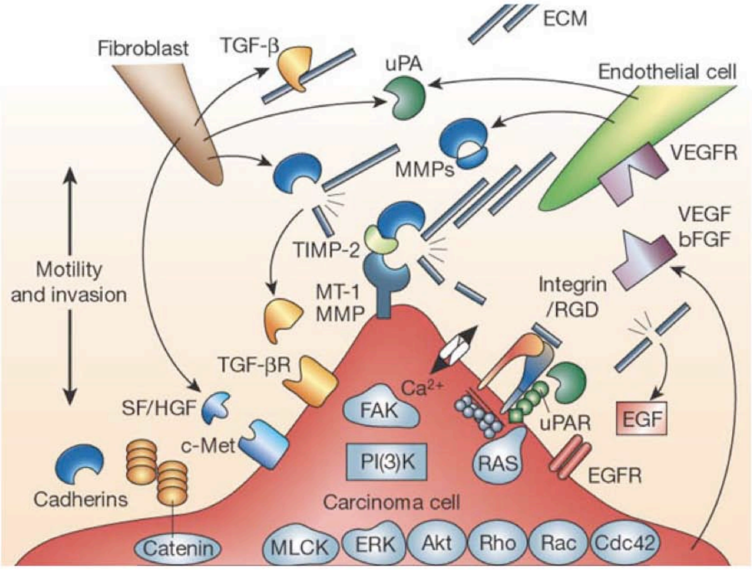

Figure 3.2 Cell communications *in vivo*. A tumour cell cross-talks with surrounding endothelial cells and fibroblast mediated with growth factors of VEGF and bFGF, as well as, latent enzymes including MMPs and uPA in the progression of angiogenesis.[8]

Neovasculation of endothelial cells mediated by VEGF from tumor cells Cell communication between localized tumor cells and a microvessel network is of importance in the progression of tumor growth. In particular, angiogenesis is controlled by the interactions between clustered tumor cells and surrounding endothelium mediated with growth factors in 3D microenvironments (Fig. 3.3).

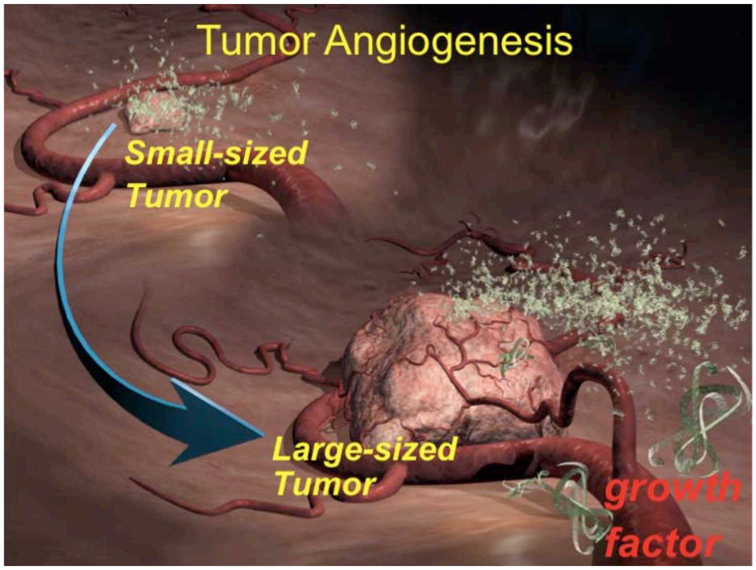

Figure 3.3 Scheme of tumor angiogenesis *in vivo*. (Courtesy of Genentech Inc.)

3.3 DESIGN

Reconstructed cancer angiogenesis *in vitro* The 3D co-culturing platform mimics *in vivo* cancer environment: clustered tumor cells localized and adjacent to a microvessel network formed of endothelial cells (Fig. 3.4)[9-17]. The angiogenesis is triggered by the condition of insufficient nutrients, which induces over-expression of growth factors, particularly $VEGF_{165}$. Mediate by VEGF, endothelial cells grow and elongate toward the VEGF source, clustered cancer cells. The platform is provided with thousands of chambers with the variations of inter-cellular distances, the size of clustered tumors, and the amount of nutrients in the culturing media.

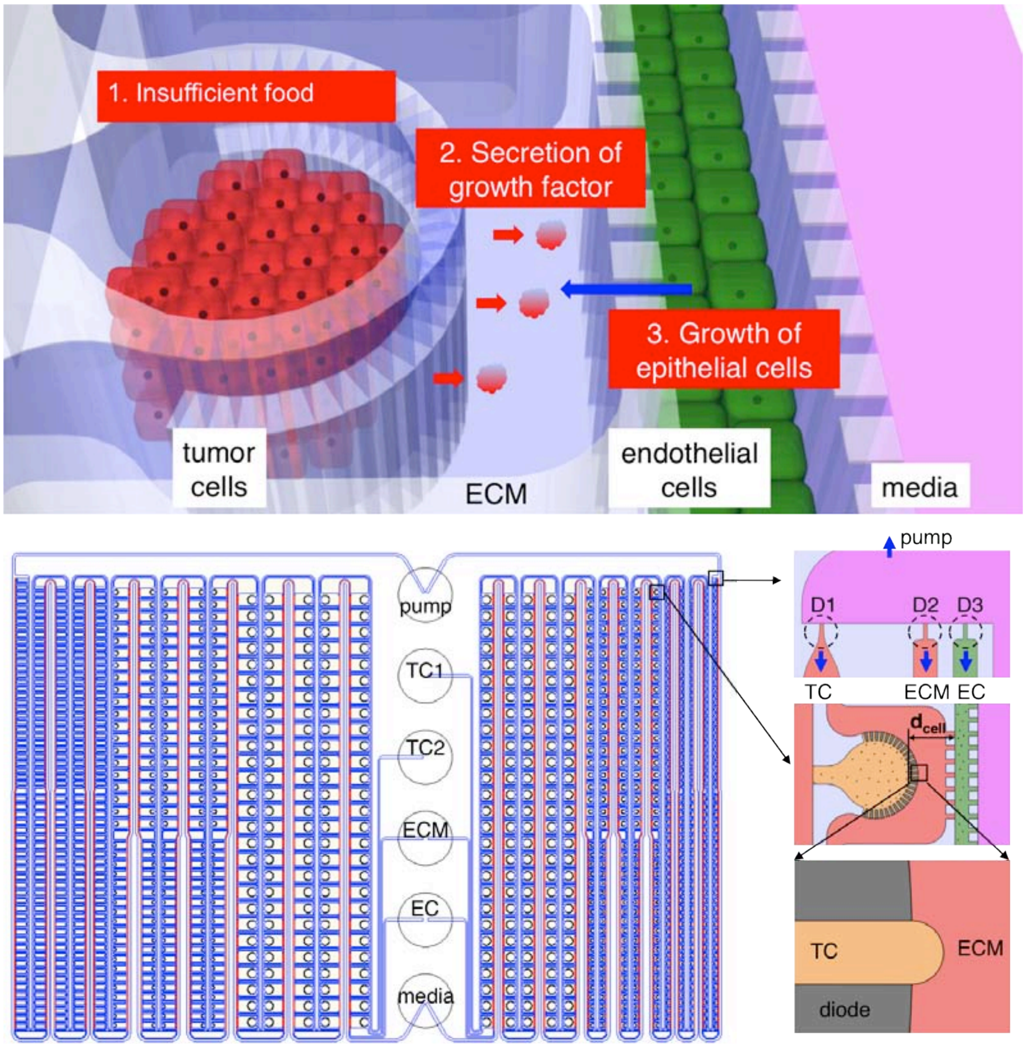

Figure 3.4 Schematic representations of a localized cancer environment for cancer angiogenesis. Tumor cells, endothelial cells, and extra cellular matrix (ECM) are co-patterned to mimic a microvascular network (upper). Deficiency of nutrition or oxygen triggers the angiogenetic pathway over-expressing growth factors and inducing neovasculation toward tumor cells secreting growth factors. The cancer environment is provided in an over-thousands array, which is regulated by a single pump and uni-/bidirectional diodes (lower).

Procedures of cell co-patterning The co-patterning involves three steps: introducing gel solutions with tumor cells and endothelial cells to the platform (Fig. 3.5A), localizing tumor cells as programmed by the fluidic diodes and fixating them in temperature-activated polymerized gel (Fig. 3.5B), and filling gaps with extra-cellular matrices (Fig. 3.5C). Patterned cells in 3D are fixed inside the collagen gels polymerized by heating at 37°C within half an hour and media is perfused (Fig. 3.5D). The diode status for the platform operation is summarized in Table 3.1.

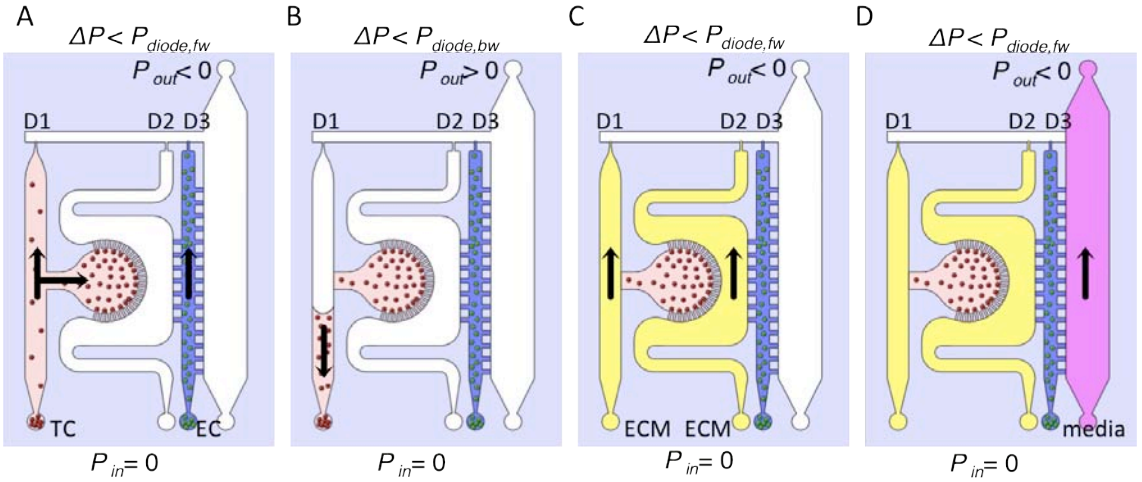

Figure 3.5 Schematic representations of procedure for co-patterning. Co-patterning is realized in three steps: cell introduction (A), cell localization and fixation (B), and ECM filling (C). After patterning, media is perfusd for cell growing (D).

Table 3.1 Summary on the platform operation.

	Operation	Pumping	D1	D2	D3
Stage 1	Cell introduction	ΔP<0	Forward Off	N/A	Forward Off
Stage 2	Cancer cell isolation	ΔP>0	Backward On	N/A	Backward Off
Stage 3	ECM filling	ΔP<0	Forward Off	Forward Off	Forward Off
Stage 4	Media perfusion	ΔP<0	Forward Off	Forward Off	Forward Off

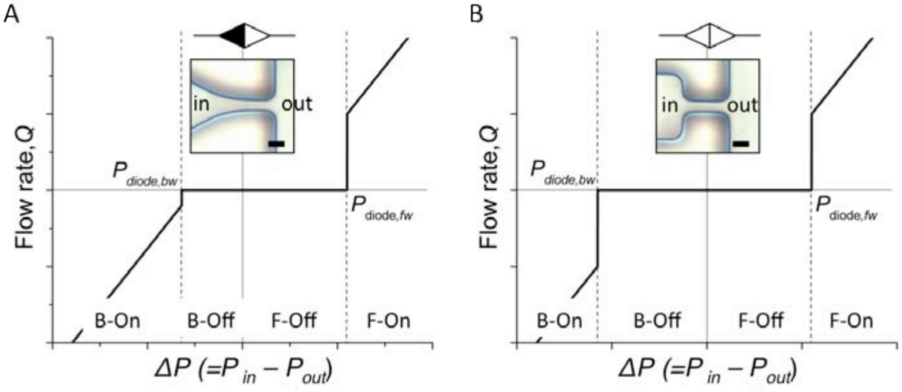

Figure 3.6 Characteristics of microfluidic diodes. Pressure-flow rate curves are provided for uni- (A) and bidirectional diodes (B). Scale bars are 10 μm.

Flow regulation using fluidic diodes The cell co-patterning is regulated using uni- and bidirectional fluidic diodes, which can regulate gel flowing in a large scale relying on the structural design (Fig. 3.6 and Table 3.2).

Table 3.2 Summary on the diode operation.

Unidirectional diode				
Status	Forward Off	Forward On	Backward Off	Backward On
Symbol	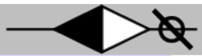		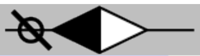	
Description	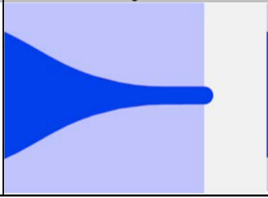	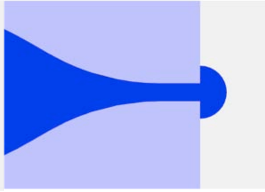	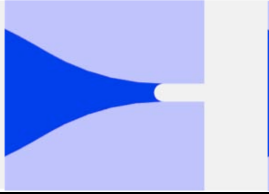	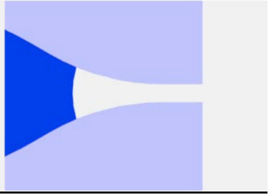

Bidirectional diode				
Status	Forward Off	Forward On	Backward Off	Backward On
Symbol				
Description	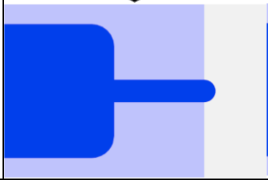	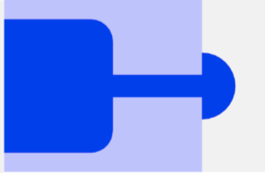		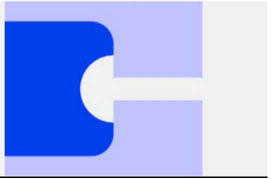

Cell culture in Petri dish Cancer cells are cultured at 37ºC under 5% CO_2 in 1x DMEM with 10% FBS, 1% Penicillin/streptomycin (Invitrogen). HUVEC (Human umbilical vein endothelial cells) are purchased from Lonza and cultured in an endothelial medium, EBM-2 media containing 2% FBS, and other growth factors (0.04% Hydrocortisone, 0.4% hFGF-B, 0.1% VEGF, 0.1% R3-IGF-1, 0.1% Ascorbic acid, 0.1% hEGF, 0.1% GA-1000, 0.1% Heparin (Lonza)) and 1% Penicillin/streptomycin are used for cell culturing under 5% CO_2 at 37 ºC. All HUVEC cells are used less than 5 passages.

Cell co-culturing in microfludic array After co-patterning, a media (1x DMEM with 2% FBS, 1% peninsuline) is continuously perfused at the flow rate of 0.1-0.5 μL/min for 6 days under 5% CO_2 at 37 ºC. Cells are prestained with MitoTracker Red and MitoTracker Green for the cancer cells and endothelial cells, respectively.

Live cell staining MCF7 (human breast cancer cell) and HUVEC cells are stained with 100 nM Mitotracker Green and Mitotracker Red (Invitrogen) for 20 min at cell culture incubator, respectively. After staining is complete, the staining solution is with PBS one time and the cells are detached for loading into a microfluidic device.

Gelation Type I collagen is purchased from BD Biosciences (Cat #354236). To make gel precursor solutions at a desired concentration, the collagen stock (solubilized in 0.02 N acetic acid) is diluted in sterile 0.1N NaOH, sterile DI water, and sterile PBS for the concentration of 2 mg/mL at pH 7.4. The solution is mixed thoroughly for the homogeneous gelation and kept in an ice up to 2 hrs to slow the gelation during experiments. After introducing the solution into a microfluidic device, the solution is gelled in an incubator after 30 min at 37 °C.

Preparation for reconstructing cancer angiogenesis in well plate To show the feasibility of cancer angiogenesis, the experiment is executed in a conventional environment, a 48 well plate[18-20]. Endothelial cells are seeded for 8 hours in culturing media with the variation of VEGF_{165} concentration and types of conditional media. The conditional media are prepared by culturing cancer cells in a serum-free medium for 48 hours. The conditional media is mixed with culturing media in the ratio of 3:1 (v/v). The compositions of media are summarized in Tabel 3.3.

Table 3.3 Summary on composition of medium to reconstruct cancer angiogenesis in a well plate.

Culturing medium 1	Culturing medium 2	Serum-free medium
1x DMEM, 2% FBS	EGM2 (2% FBS), growth factors	1x DMEM

Preparation for reconstructing cancer angiogenesis in microfludic array The cancer angiogenesis environment is reconstructed in the microfludic platform by providing tumor cells with a starvation condition without any growth factors in gel solutions. The compositions of gel solution and media are summarized in a table 3.4.

Table 3.4 Summary on the gel solution and media to reconstruct cancer angiogenesis in microfluidic array.

Case	TC region	ECM region	EC region	Media
Data	TC, gel	gel	EC, gel	1x DMEM, 2% FBS, 1% Penicillin
Positive control	VEGF 200 ng/mL, gel	gel	EC, gel	1x DMEM, 2% FBS, 1% Penicillin
Negative control	gel	gel	EC, gel	1x DMEM, 2% FBS, 1% Penicillin

Experimental setup for cell co-patterning in microfludic array To minimize the gelation during experiments, the microfluidic device and gel solution are maintained cool on top of a microscope by placing a cooling chamber (Fig. 3.7). The cooling chamber consists of an upper part filled with dry ices and a lower part filled with a cool air. The chamber can decrease the air temperature from 25 °C down 4 °C within 10 minutes and maintain the temperature ranging 0 to 5 °C during experiment. The platform is connected to the pressure regulator through a single tube at an outlet reservoir and supplied with each gel solution from a long-nose pipette tip connected to each inlet reservoir.

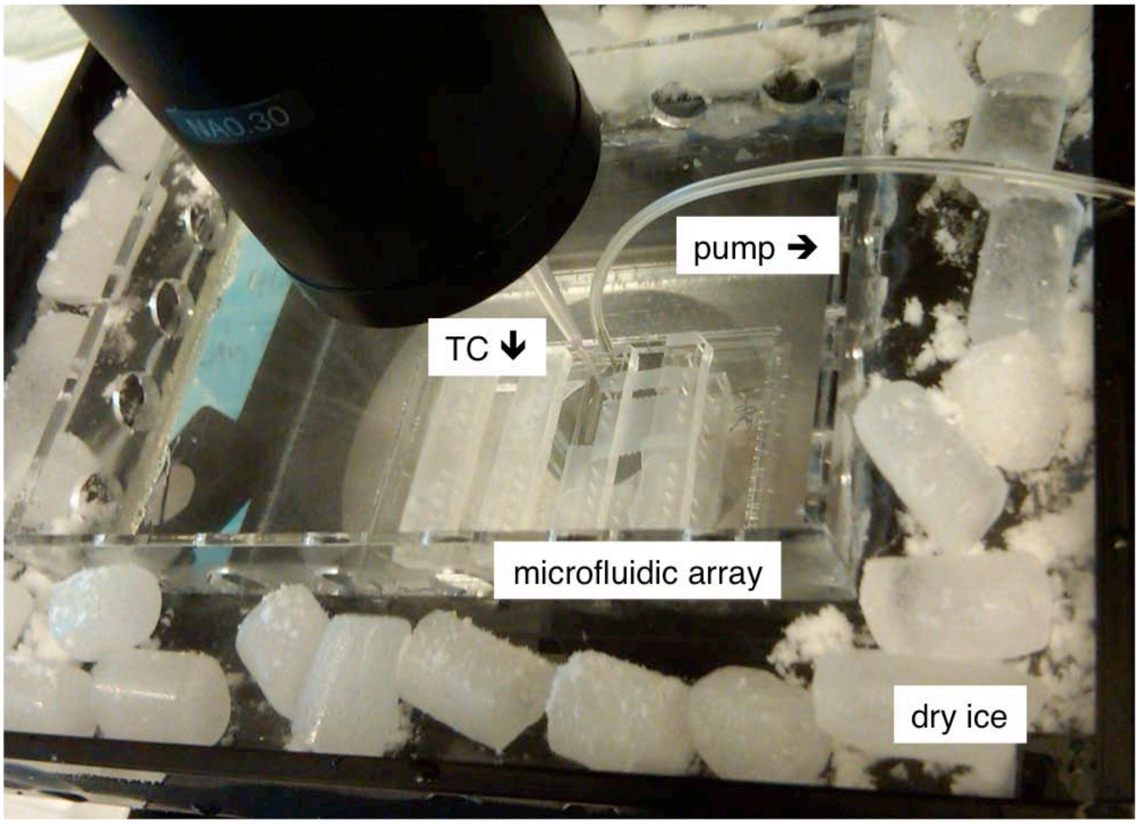

Figure 3.7 Experimental setup for cell co-patterning.

Experimental setup for cell co-culturing in microfludic array The platform is kept in a cell-culturing incubator under 5% CO_2 at 37 ºC while covered with a plastic lid minimizing evaporation and contamination. The platform is connected to a pressure pump through a single tube at an outlet reservoir and supplied with media from a long-nose pipette tip connected to each inlet reservoir.

3.4 CHARACTERIZATION

Co-patterning of multicolor dyes The concept of the co-patterning was verified by patterning multi-colored dyes representing gels including different types of cells. The co-pattering involves three steps: (A) filling circular chambers, (B) isolating liquid in the chambers to pattern cancer cells, and (C) filling line channels to pattern endothelial cells (Fig. 3.8).

Co-patterning of multicolor dyes in array The co-patterning was realized in chambers in a large scale with a variation of chamber sizes (Fig. 3.9).

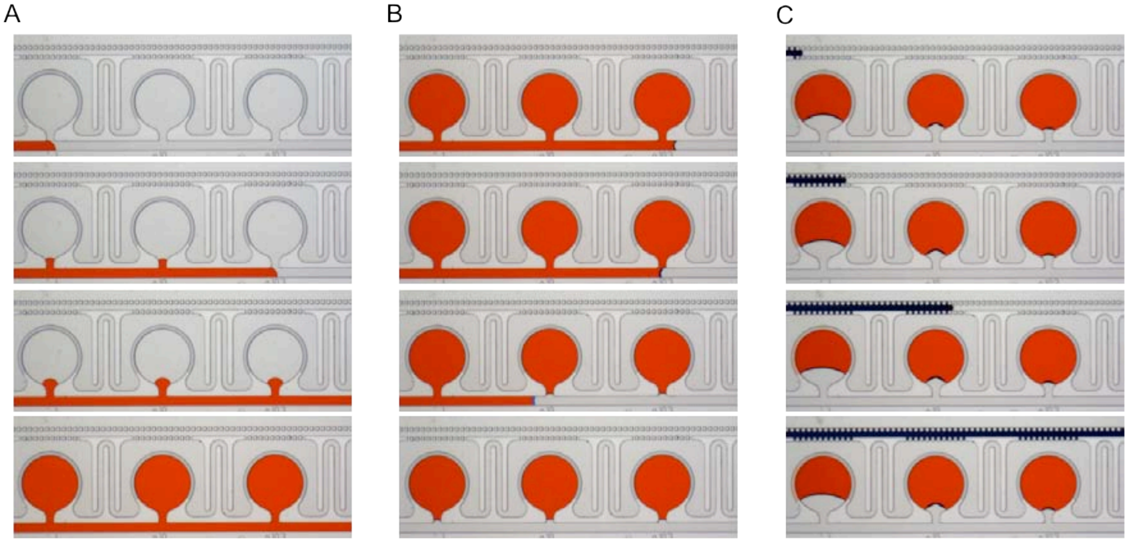

Figure 3.8 Experimental validation of the co-patterning with color dyes corresponding to co-patterning TCs (red) and ECs (blue). Co-patterning is accomplished through three steps: circular chamber filling (A), chamber isolation (B), and lined-channel filling (C).

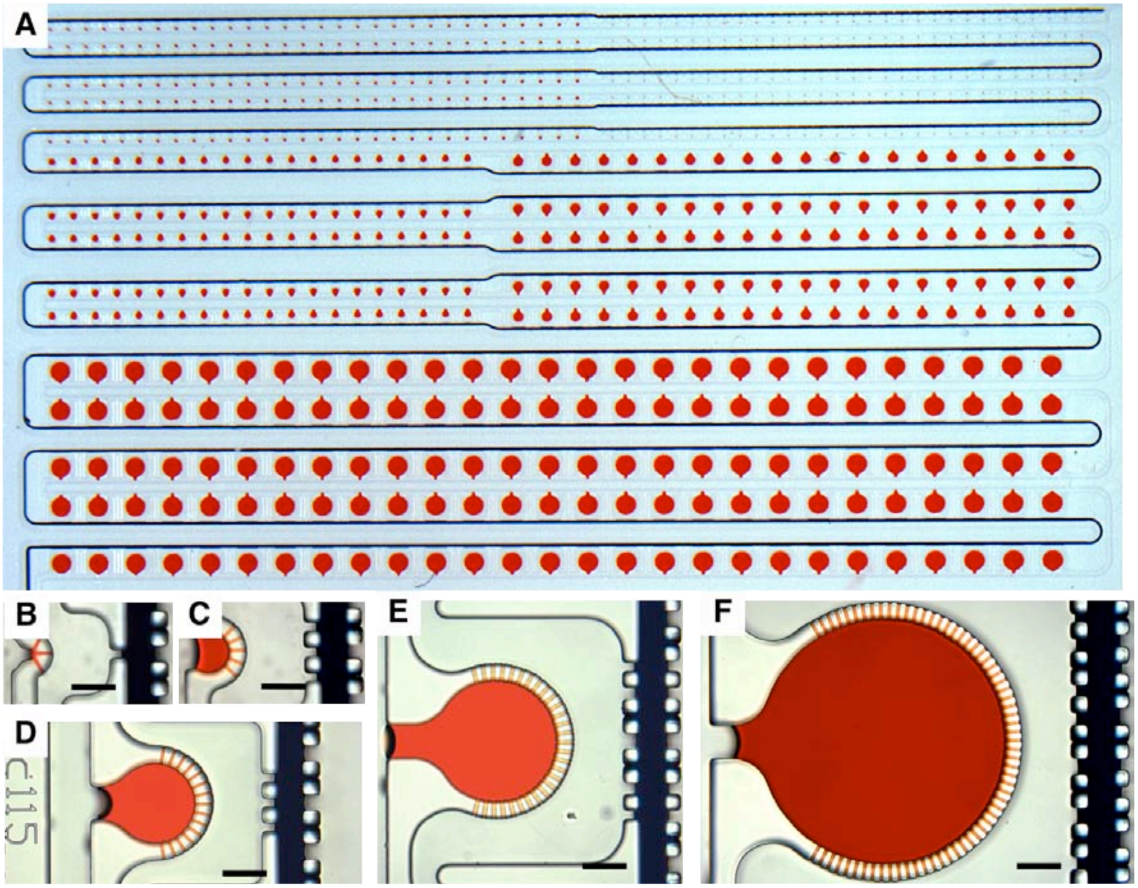

Figure 3.9 Co-patterning of dyes in an array. Liquids are patterned in the chambers in an array format (A) providing five size variations for the quantitative study on the size variation of clustered tumors (B – F). Scale bars are 50 μm.

Co-patterning of cells Furthermore, the technique was applied to pattern breast cancer cells (MCF7) in the circular chambers and endothelial cells (HUVEC) in line channels (Fig. 3.10).

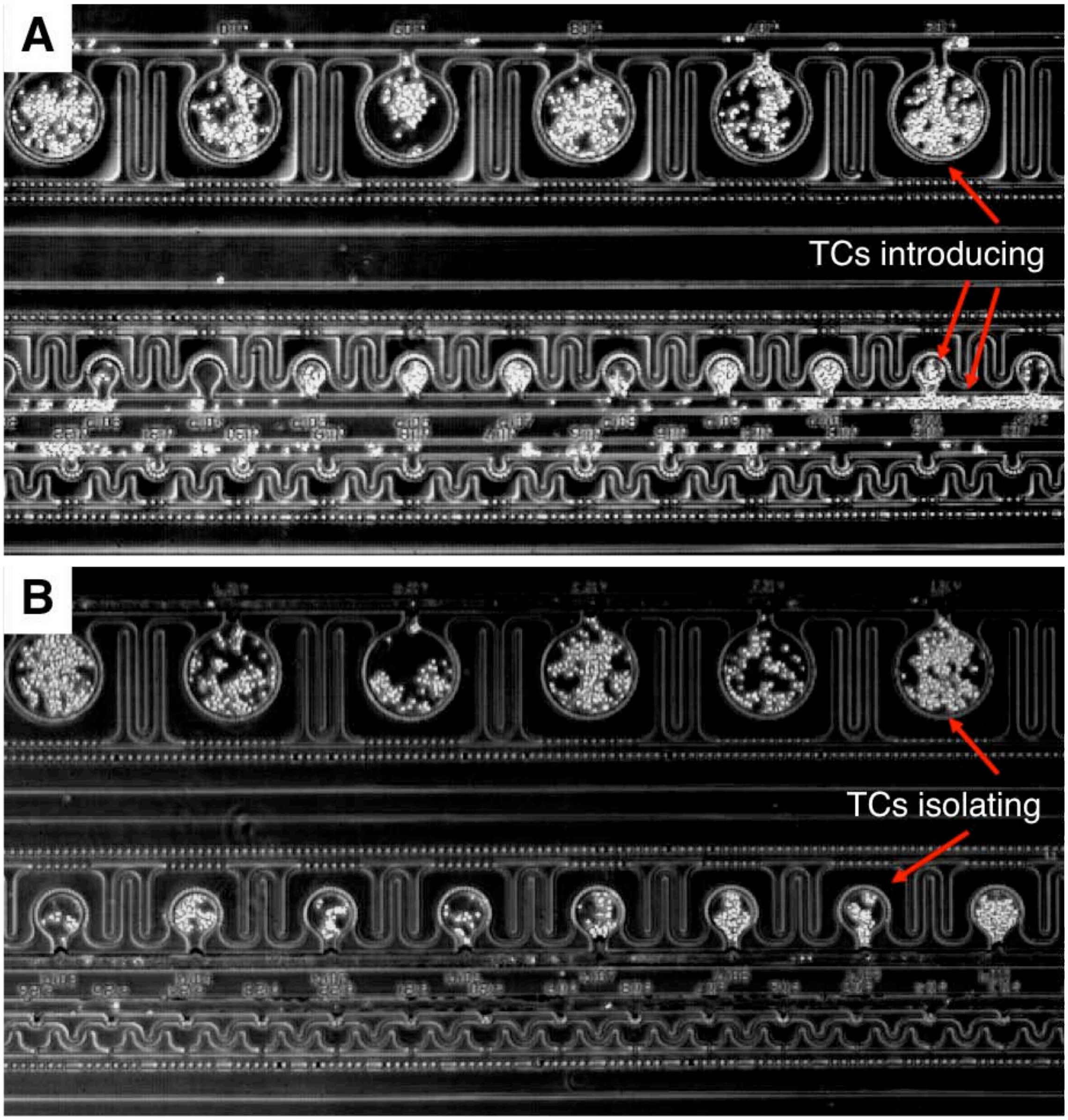

Figure 3.10 Co-patterning of breast cancer cells and endothelial cells. (A) Cancer cells are introduced through horizontal supplying channel and trapped in circular chambers. **(B)** Redundant cancer cells in the supplying channel are removed back.

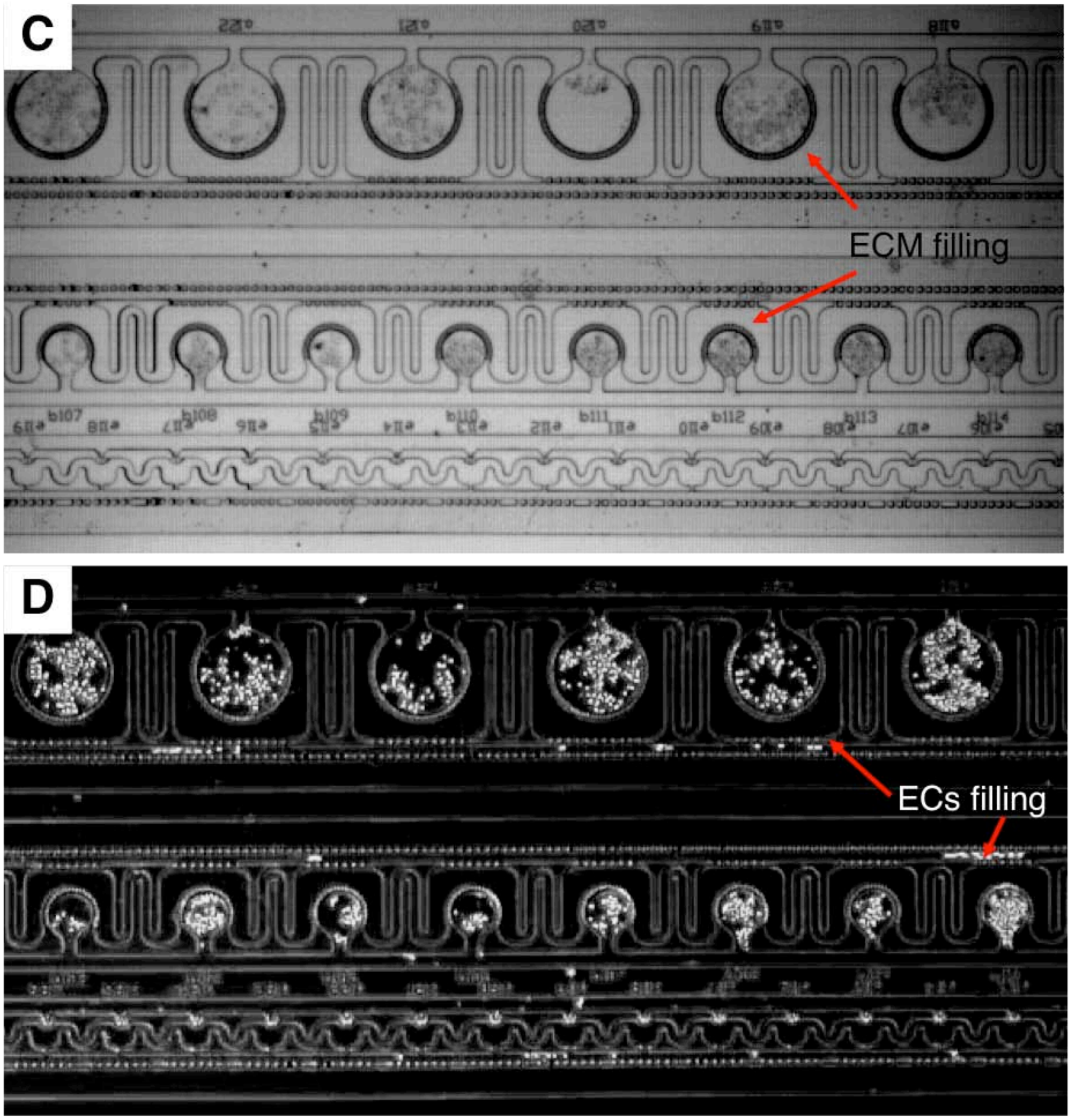

Figure 3.10 Co-patterning of breast cancer cells and endothelial cells. (C) Area surrounding the circular chambers is filled with empty gel to form extracellular matrix. **(D)** Endothelial cells are supplied through and trapped in another horizontal channels confined by pillars.

Characterization of cell patterning The cell trapping was quantified by counting average number of the MCF7 with the variation of the initial concentration (Fig. 3.11).

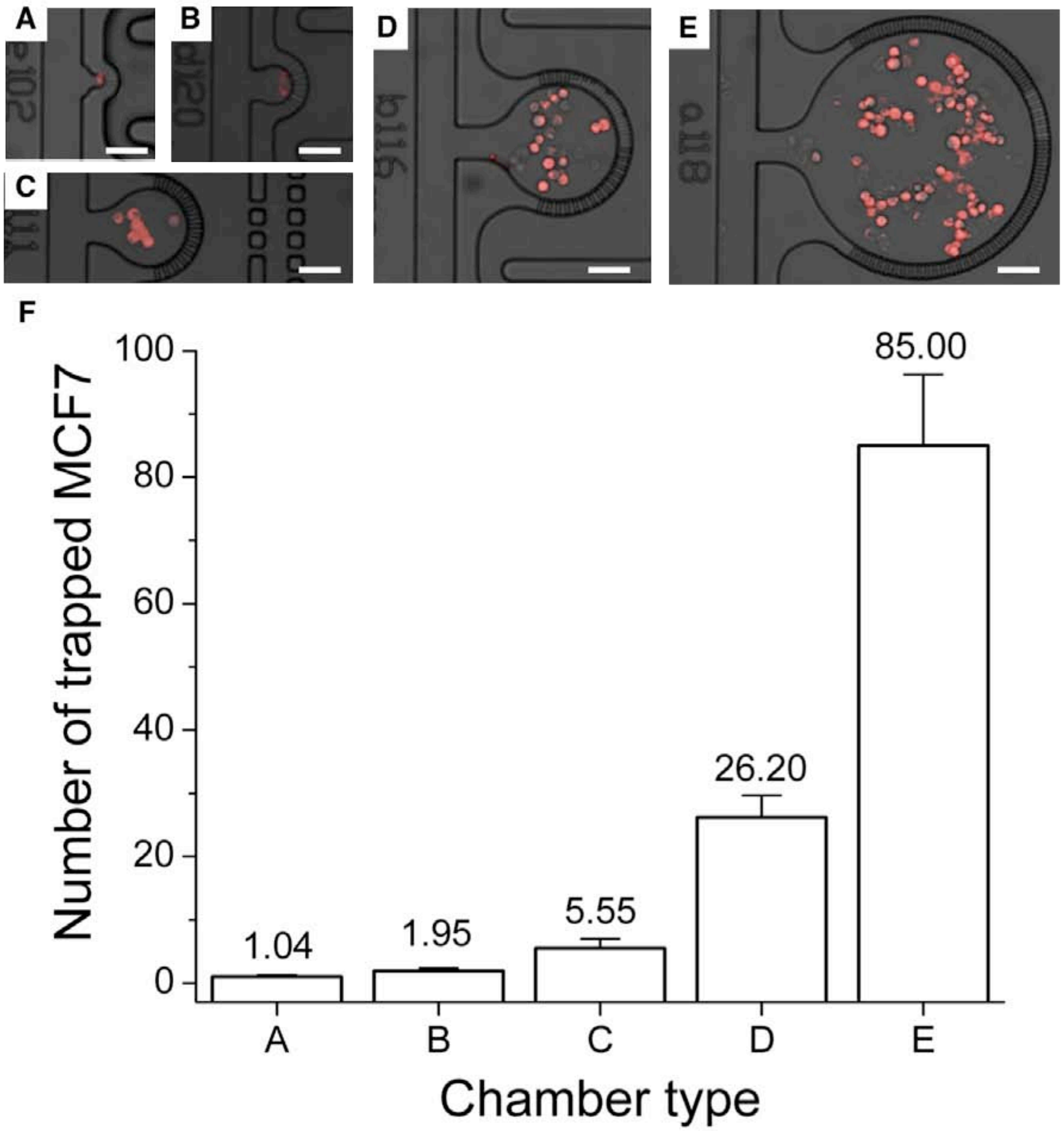

Figure 3.11 Cell trapping and the quantification. (A-E) Cells are enclosed in the circular chambers with the size variation. **(F)** The cell trapping is quantified by calculating the average number and a standard error of trapped cells in 10 chambers for each type. Scale bars in the sections of 'A' to 'E' are 50 µm.

Reconstructing cancer angiogenesis in well plate Endothelial cells formed tubes more actively with the higher concentration of VEGF and in certain conditional media (Fig. 3.12, 3.13). The tube formation was further elevated in the EGM2-based media. In all cases of media, conditional media from U87MG induced the tube formation indicating that U87MG secreted more growth factors inducing tube formation of the endothelial cells.

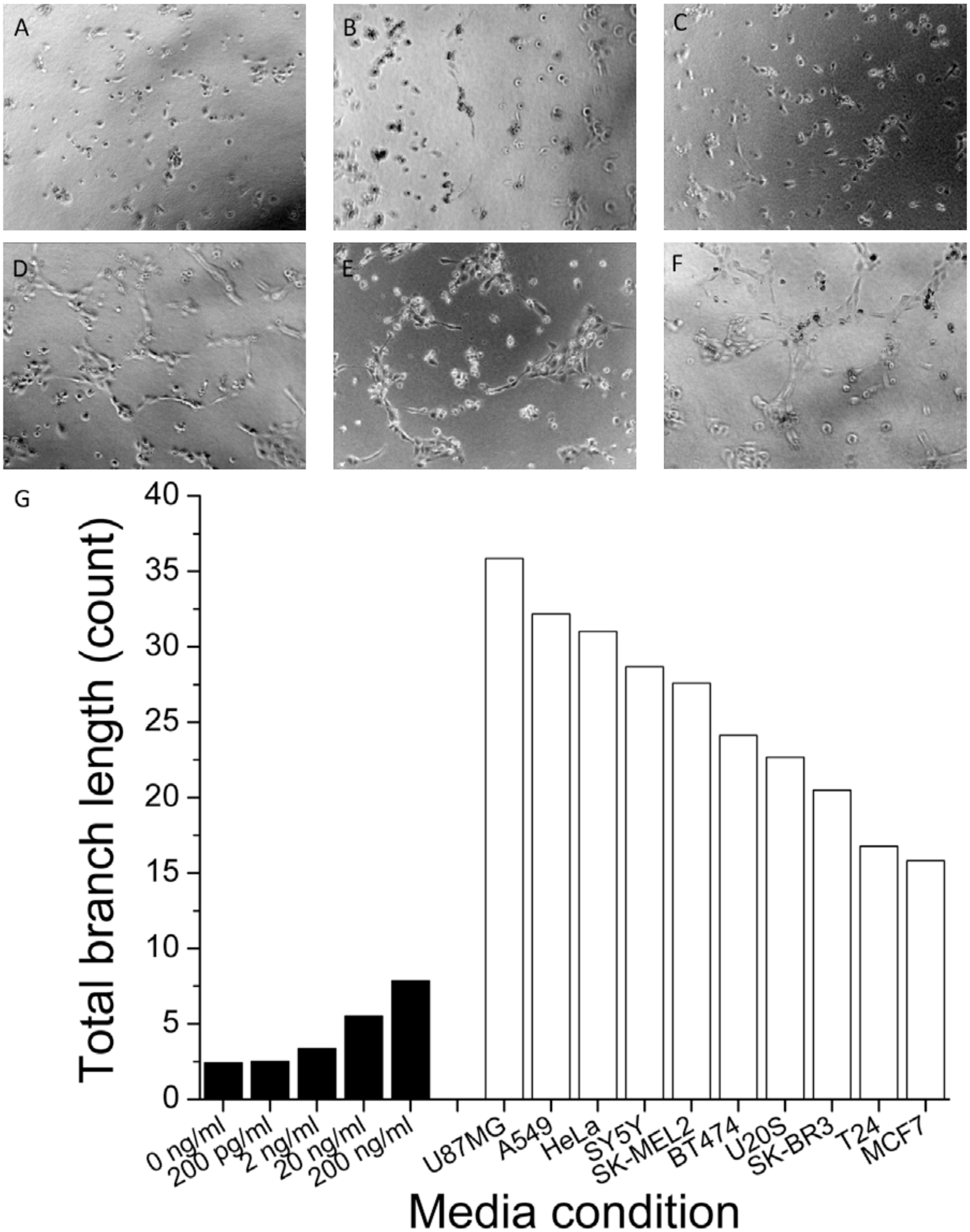

Figure 3.12 Reconstructing cancer angiogenesis with DMEM-based media in well plate. The tube formation was more effective as the concentration of VEGF increased (A: 0 ng/mL, B: 2 ng/mL, C: 200 ng/mL). More active formation was observed with conditional media (D: U87MG, E: A549, F: HeLa). (G) The tube formation was quantified by comparing the total branch length.

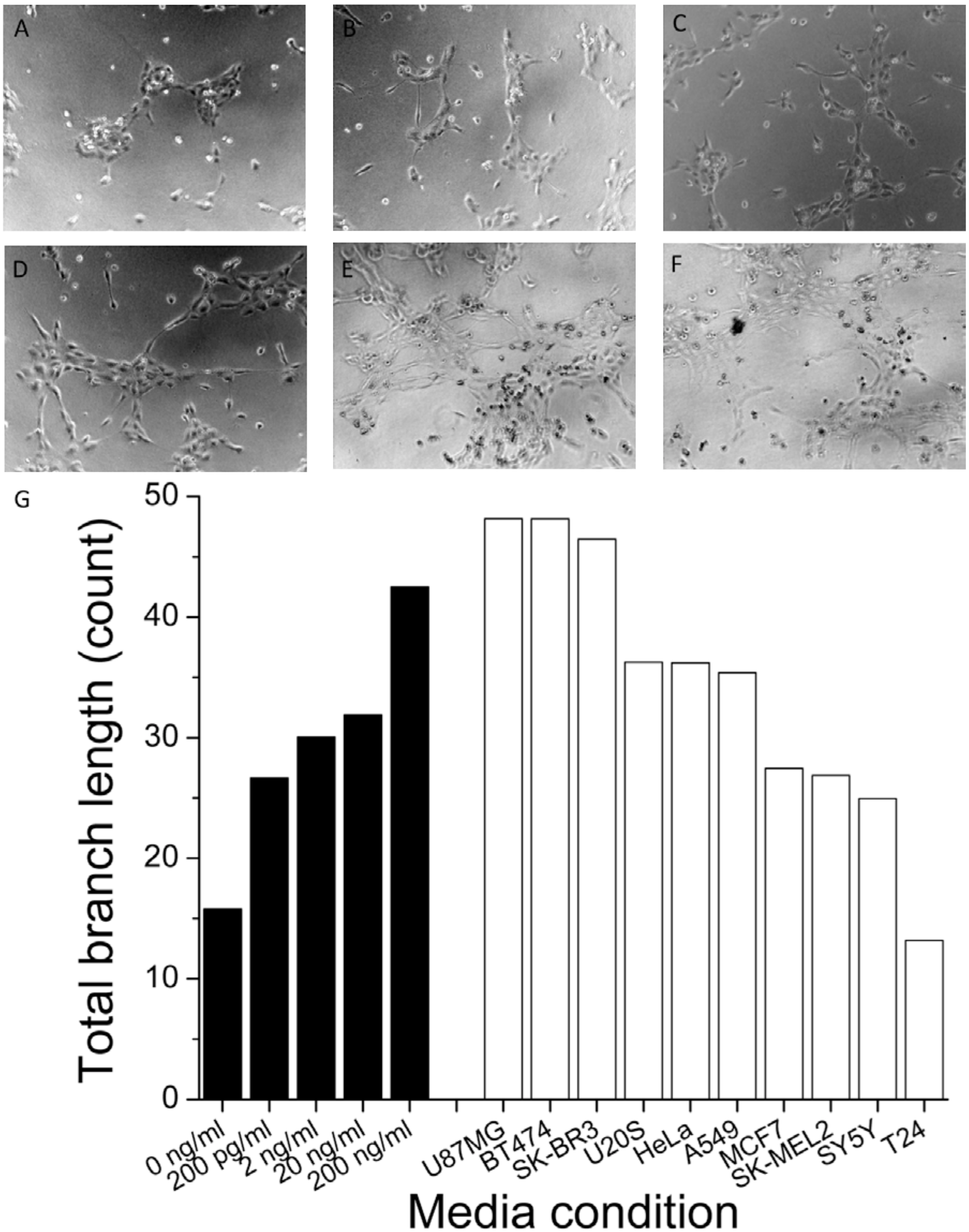

Figure 3.13 Reconstructing cancer angiogenesis with EGM2-based media in well plate. The tube formation was more effective as the concentration of VEGF increased (A: 0 ng/mL, B: 2 ng/mL, C: 200 ng/mL). More active formation was observed with conditional media (D: U87MG, E: BT474, F: SK-BR3). (G) The tube formation was quantified by comparing the total branch length.

Cell co-culturing To evaluate the cell-culturing environment, additional nutritents and growth factors were added as Table 3.4. After co-patterning, a media (1x DMEM with 10% FBS, 1% peninsuline) was continuously perfused at the flow rate of 0.1-0.5 μL/min for 6 days under 5% CO_2 at 37 ºC. Cells were prestained with MitoTracker Red and MitoTracker Green for the cancer cells and endothelial cells, respectively. Both of breast cancers and endothelial cell were proliferated successfully in the co-cultured environment (white circle in Fig. 3.14). The endothelial cells were divided in the EC region rather than growing toward cancer cells due to the presence of growth factors in the EC region.

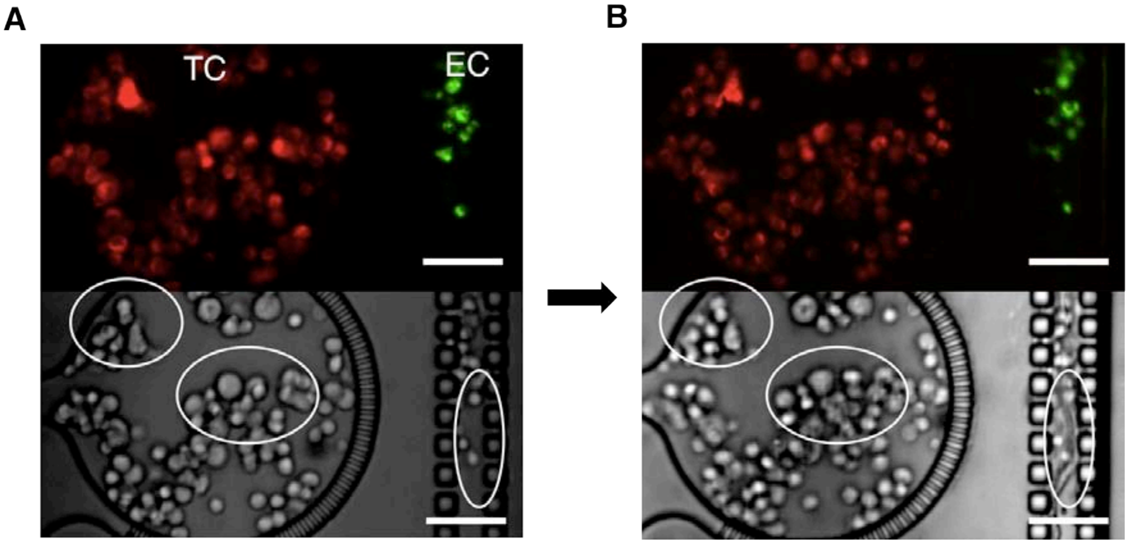

Figure 3.14 Co-culturing of breast cancer cells (TC) and endothelial cells (EC). Cell co-patterning at 0 day (A) and cell growing after 6 days (B) are shown in fluorescent images (upper: TCs in red and ECs in green) and bright field images (lower). Scale bars are 50 μm.

3.5 CONCLUSIONS

I demonstrate that microfluidic diode-based platform can design cell co-patterning in a large scale by using a single pump and a pipette loading. I provided cancer environment by co-patterning breast cancer cells adjacent to endothelial cells, which mimics cellular microenvironment for the study on cancer angiogenesis. The platform would allow investigating the cellular communication in angiogenesis by providing systematic and efficient ways to regulate the environment.

3.6 DISCUSSION

The study on the cancer angiogenesis in the co-culturing platform is under study. At of now, there a challenging issue: dense packing of EC. The dense packing EC in the channel is not realized uniformly due to the large gap size of pillars compared to cell size (EC is 10 to 25 μm diameter), pressure buildup after the cell clogging, and the breakage of the pinning meniscus by escaping cells (Fig. 3.15). To realize the dense packing, it is considered to decrease gap size (current version is 20 μm diameter) and widen the channel (current version is 30 μm width).

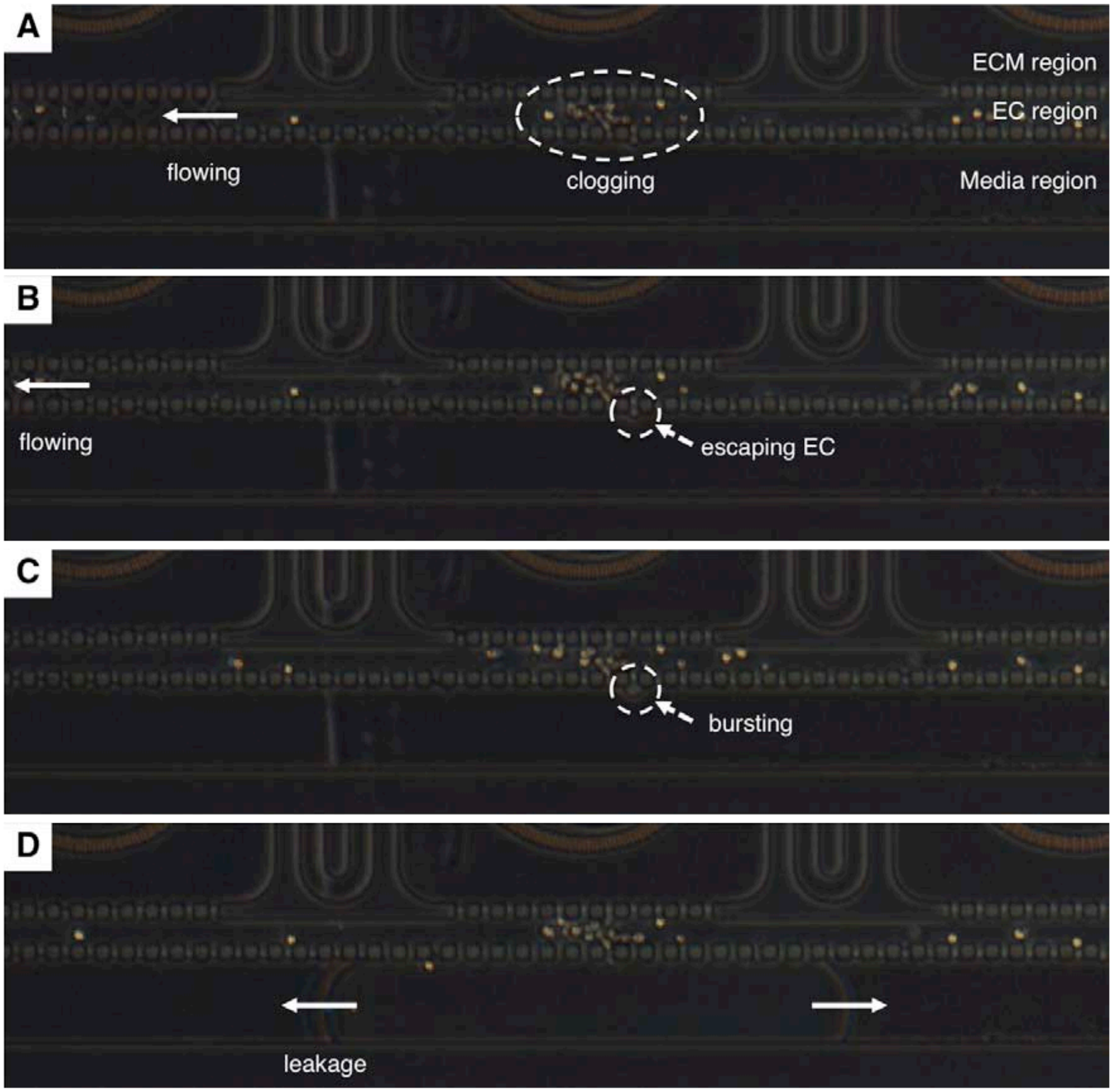

Figure 3.15 Meniscus breakdown due to a single cell escape. (A) The meniscus at pillars isolates the EC region form the media region while allowing flow through a straight channel. **(B)** As ECs clog the channel, the flow resistance through the channel increases and a single cell escapes through a pillar gap. **(C)** As the cell escapes through the gap, it breaks the meniscus. **(D)** As a result, leakage incurs at low pressure then the expected.

References:

(1) Petersen, O. W., Ronnov-Jessen, L., Howlett, A. R. & Bissell, M. J. Interaction with basement membrane serves to rapidly distinguish growth and differentiation pattern of normal and malignant human breast epithelial cells. *Proc. Natl Acad. Sci.* **1992**, 89, 9064–9068.

(2) Cukierman, E., Pankov, R., Stevens, D. R. & Yamada, K. M. Taking cell-matrix adhesions to the third dimension. *Science* **2001**, 294, 1708–1712.

(3) Zaman, M. H. *et al*. Migration of tumor cells in 3D matrices is governed by matrix stiffness along with cell-matrix adhesion and proteolysis. *Proc. Natl Acad. Sci. USA* **2006**, 103, 10889–10894.

(4) Montesano, R. *et al*. Identification of a fibroblast-derived epithelial morphogen as hepatocyte growth factor. *Cell* **1991**, 67, 901–908.

(5) Bissell, M. J., Hall, H. G. & Parry, G. How does the extracellular matrix direct gene expression? *J. Theor. Biol.* **1982**, 99, 31–68.

(6) Bissell, M. J., Rizki, Mian, A., I. S. Tissue architecture: the ultimate regulator of breast epithelial function, *Current Opinion in Cell Biology* **2003**, 15, 753–762.

(7) Friedrich, M. J., Studying Cancer in 3 Dimensions 3-D Models Foster New Insights Into Tumorigenesis, *JAMA* 2003, 290, 15, 1977-1979.

(8) Liotta, L. A., Kohn, E. C., The microenvironment of the tumour–host interface, *Nature* **2001**, 411, 375-379.

(9) Souza, G. R. et al., Three-dimensional tissue culture based on magnetic cell levitation, *Nat. Nano*. **2010**.

(10) Kim, J., Hegde, M., Jayaraman, A., Co-culture of epithelial cells and bacteria for investigating host-pathogen interactions, *Lab on a Chip* **2010**, 10, 43-50.

(11) Domansky, K., Inman, W., Serdy, J., Dash, A., Lim, M. H. M., Griffith, L. G., Perfused multiwell plate for 3D liver tissue engineering, *Lab on a Chip* **2010**, 10, 51-58.

(12) Zhang, C., Zhao, Z., Rahim, N. A. A., Noort, D. V., Yu, H., Towards a human-on-chip: Culturing multiple cell types on a chip with compartmentalized microenvironments, *Lab on a Chip* **2009**, 9, 3185-3192.

(13) Sudo, R., Chung, S., Zervantonakis, I. K., Vickerman, V., Toshimitsu, Y., Griffith, L. G., Kamm, R. D., Transport-mediated angiogenesis in 3D epithelial coculture, *FASEB J.* **2009**, 7, 2155-2164.

(14) Ni, M., Tong, W. H., Choudhury, D., Rahim, N. A. A., Iliescu, C., Yu, H., Cell Culture on MEMS Platforms: A Review, *Int. J. Mol. Sci.* **2009**, 10, 5411-5441.

(15) Lee, S. A., Chung, S. E., Park, W., Lee, S. H., Kwon, S., Three-dimensional fabrication of heterogeneous microstructures using soft membrane deformation and optofluidic maskless lithography, *Lab on a Chip* **2009**, 9, 1670-1675.

(16) Huang, C. P., Lu, J., Seon, H., Lee, A. P., Flanagan, L. A., Kim, H.-Y., Putnam, A. J., Jeon, N. L., Engineering microscale cellular niches for three-dimensional multicellular co-cultures, *Lab on a Chip* **2009**, 9, 1740-1748.

(17) Chung, S., Sudo, R., Mack, P. J., Wan, C.-R., Vickerman, V., Kamm, R. D., Cell migration into scaffolds under co-culture conditions in a microfluidic platform, *Lab on a Chip* **2009**, 9, 269-275.

(18) Haddad, L, El Hajj, H., Abou-Merhi, R., Kfoury, Y., Mahieux, R., El-Sabban, M., Bazarbachi, A., KSHV-transformed primary effusion lymphoma cells induce a VEGF-dependent angiogenesis and establish functional gap junctions with endothelial cells, *Leukemia* **2008**, 22, 826–834.

(19) Ali, M. A., Choy, H., Habiby, A. A., Saha, D., SNS-032 Prevents Tumor Cell–Induced Angiogenesis By Inhibiting Vascular Endothelial Growth Factor, *Neoplasia* **2007**, 9, 370–381.
(20) Ye, J., Yuan, L., Inhibition of P38 MAPK reduces Tumor Conditioned Medium-Induced Angiogenesis in Co-Cultured Human Umbilical Vein Endothelial Cells and Fibroblasts, *Biosci. Biotechnol. Biochem.* **2007**, 71, 1162-1169.

CHAPTER 4:
APTAMER-BASED NANOBIOSENSOR ANALOGOUS TO ANTIBODY

We describe an aptamer-based Surface Enhanced Resonance Raman Scattering (SERRS) nanosensor with high sensitivity, specificity, and stability for the detection of a coagulation protein, human α-thrombin. The nanosensor achieves high sensitivity and a limit of detection of 100 pM by monitoring the SERRS signal change upon the single step of thrombin binding to thrombin binding aptamer immobilized on gold nanoparticles. The selectivity of the nanosensor is demonstrated by the specific discrimination of thrombin from other protein analytes. The specific recognition and binding of thrombin by the thrombin binding aptamer is essential to the mechanism of the aptamer-based nanosensor, as shown through measurements using negative control oligonucleotides. In addition, the sensor can detect 1 nM thrombin in the presence of complex biofluids, such as 10% fetal calf serum, demonstrating that the immobilized, 5'-capped, 3'-capped aptamer is sufficiently robust for clinical diagnostic applications. Furthermore, the proposed nanosensor may be implemented for multiplexed detection using different aptamer-Raman probe complexes.

Reproduced from “Aptamer-based SERRS Sensor for Thrombin Detection,” by Hansang Cho and *et al.*, in Nano Letters, 8, 4386-4390 (2008), with permission from ACS publications.

4.1 INTRODUCTION

As nanobiotechnology progresses, aptamers, single-stranded (ss) oligonucleotides (<100 nt), have been promoted as ideal diagnostic reagents and potential antibody replacements for the development of biomolecular nanosensors due to their high affinity, specificity, and stability.[1-9] Interestingly, certain aptamers have been reported to undergo distinguishable conformational changes upon interaction with their targets.[10-15] Recently, numerous aptamer-based sensors (aptasensors or aptamer beacons) have exploited binding-induced conformational changes to monitor the interaction with targets by measuring electron transfer[10,11,16,17], color change[12-14,18], or fluorescence quenching[15,19,20]. However, these methods are limited by either the size or sensitivity of the sensors or by the complexity of the assays involved. For example, electrochemical sensors designed to measure electron transfer require electrodes on the millimeter scale to achieve sufficient sensitivity; colorimetric methods require a large amount of particle aggregation to induce a discernable color change; the previously reported surface-enhanced Raman scattering (SERS) aptasensor used multiple binding events, a sandwich assay requiring labeling of target molecules with the complex of gold nanoparticle/aptamer/Raman probe/silver nanoparticle after capturing the target.[21,22]

4.2 PRINCIPLES

Structural change in aptamers up on target binding Aptamers often undergo significant conformational changes when target molecules are bound to the aptamers. This property enables to design sensors reporting target binding without an additional step for probes. For example, the thrombin-binding aptamer containing 15-mer aptamer d(GGTTGGTGTGGTTGG) specifically binds thrombin protein and inhibits thrombin-catalyzed fibrin-clot formation. The thrombin aptamer forms a G-quadruplex structure induced by the interaction with a desired target (Fig. 4.1).[23,24]

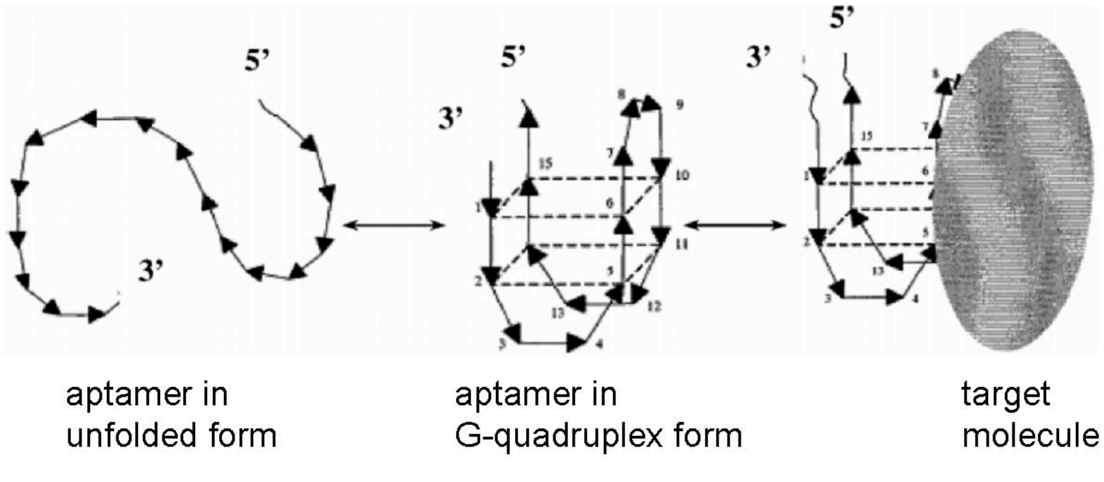

Figure 4.1 Schematics represent aptamer's structural change upon target binding. [x1]

SERRS Recently, surface-enhanced Raman scattering (SERS) is getting attention as nanofabrication techniques are developed. SERS provides spectra composed of narrow spectral peaks that allow multiplexed detection even without any labeling.

In general, the SERS enhancement factor is known as:

$$G_{em}(\nu_S) \propto \left|A(\nu_L)\right|^2 \cdot \left|A(\nu_S)\right|^2$$

,where $A(\nu_L)$ is a local enhancement factor of excitation light, which is the ratio of of 2/1 (blue waves in Fig. 4.2) at the light wavelength of ν_L and $A(\nu_S)$ is a local enhancement factor of excitation light, which is the ratio of of 4/3 (red waves in Fig. 4.2) at the wavelength of ν_S.

The intensity of SERS can be further enhanced by using wavelength matching, surface-enhanced resonance Raman scattering (SERRS). The maximized resonance occurs when the wavelength of an exciting laser is close to the peak wavelength of the surface plasmon peak on the metal surface and the wavelengths corresponding to molecular vibration modes.[25] SERRS is effective even for realizing the single molecular detection.[26]

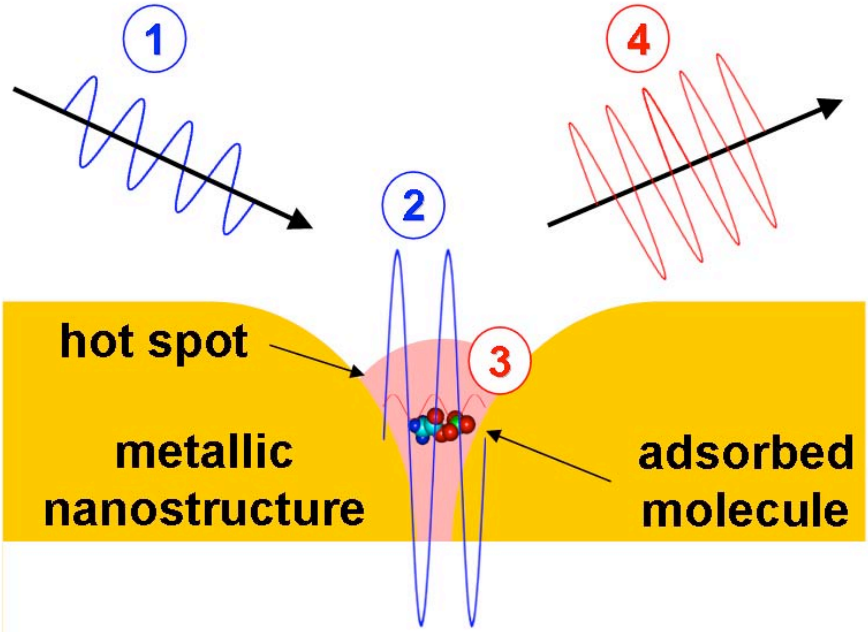

Figure 4.2 Schematics represent signal enhancement process mediated with surface plasmon. Excitation light (1) induces surface plasmon on metal surfaces, which is locally enhanced at a hot spot where surface plamon is coupled (2). Raman scattered light from molecules are induced by the local surface plasmon (3) and the Raman scattering is further enhanced at the hot spot (4).

4.3 DESIGN

Detection mechanism The detection is based on the change of SERRS intensity of the Raman probe (Fig. 4.3). In the absence of thrombin, single-stranded thrombin-binding aptamer (TBA) is unfolded and adsorbed onto a GNP surface. This brings the methylene blue in close proximity to the GNP surface (Fig. 4.3A), resulting in surface enhanced Raman scattering for methylene blue. Upon introduction of the target protein, TBA undergoes a conformational change (G-quadruplex formation) induced by a single-step binding event with thrombin (Fig. 4.3B). TBA is thus being displaced from the GNP surface, hence reducing the intensity of the SERRS signal for MB.

TBA displacement event is realized by exploiting the propensity of single-stranded DNA (ssDNA) to readily absorb onto GNP surfaces and to subsequently desorb upon its target binding.[12,13,27,28] For the present study, a 15-mer TBA (5’-**GG**T T**GG** TGT **GG**T T**GG**-3′**,** “**G**” marked in bold is essential for quadruplex formation for thrombin binding) previously reported to bind thrombin with a dissociation constant of 25 nM, was used.[29,30] A thiol functional group was added to the 5′ end for covalent binding to the gold surface, and the Raman probe (methylene blue, MB) was covalently bound to the 3′ end. The full sequence is as follows: [5′-$(CH_2)_6$-S-S-$(CH_2)_6$-TAA GTT CAT CTC CCC **GG**T T**GG** TGT **GG**T T**GG** T–MB-3′]. The thiolized TBA is adsorbed on the surface in two populations: chemical and physical adsorption.[31,32] Chemisorbed TBA, bound through a covalent gold-thiol bond, would remain immobilized upon addition of sample solutions and provide a baseline signal level to verify the stability of the ssDNA aptamer and the light-sensitive MB during exposure to complex biofluids, surface plasmon heating, and incident laser. Physisorbed TBA, in contrast, is held to the GNP surface only through electrostatic interactions between nitrogenous bases and the GNP surface and will be susceptible to displacement from the surface upon recognition and binding of target molecules.[27,32,33]

Quantitative and sensitive detection of thrombin is achieved by monitoring the strong SERRS peaks of methylene blue, covalently attached to TBA. Methylene blue has a $S_0 \rightarrow S_1$ transition centered at around 660 nm, allowing the incoming light in 632 nm wavelength to excite resonant vibration of the molecule. As a result, SERRS which is much stronger than non-resonant SERS is observed while providing narrow spectral lines suited to quantitative analysis.[34,35]

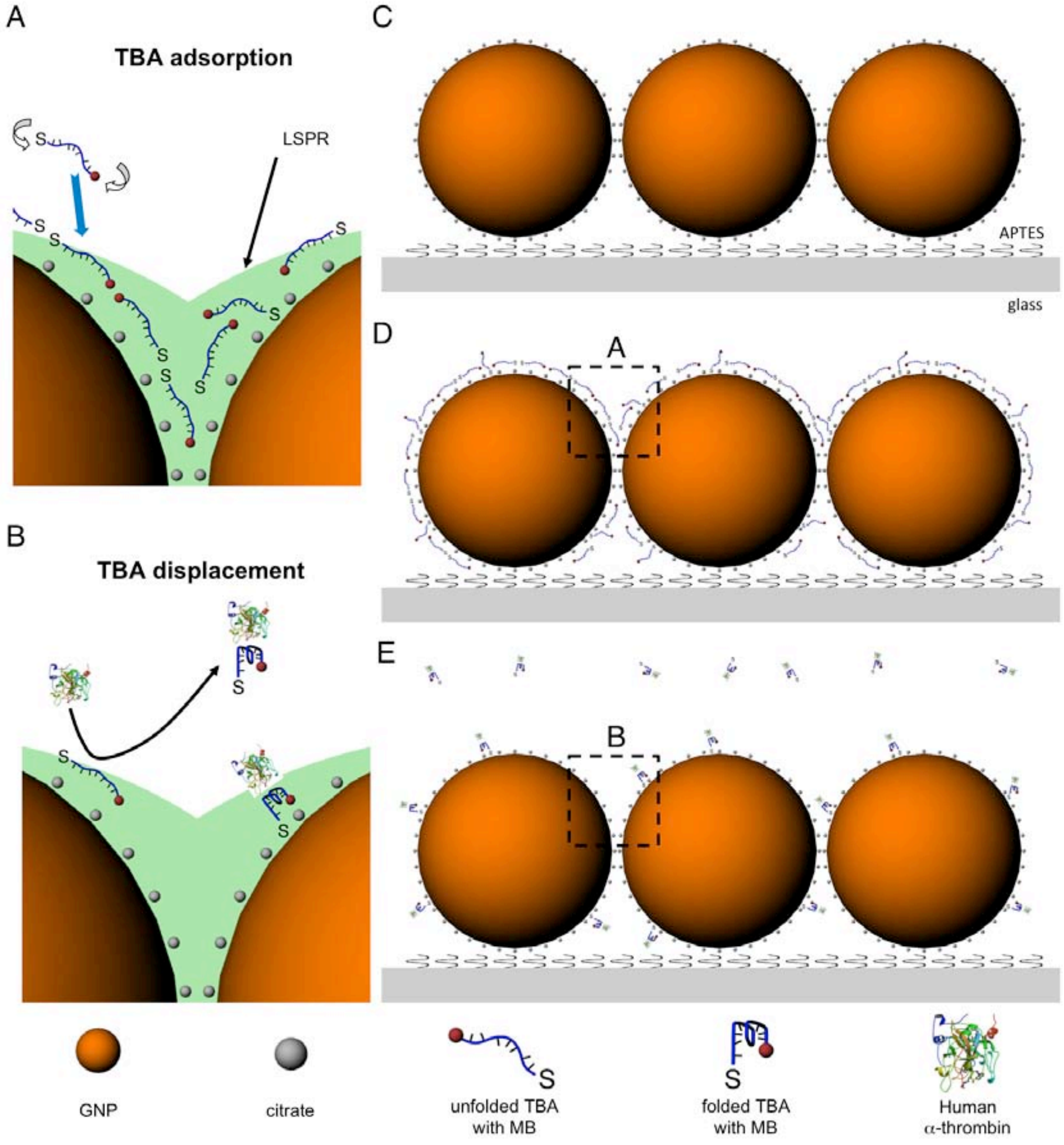

Figure 4.3 Schematics of detection method and preparation steps for the aptamer-based SERRS nanosensor. (A) A thiol-modified single-stranded TBA attached to MB, is naturally unfolded in the absence of human α-thrombin target molecule. The unfolded TBA is physisorbed on GNP surface through electrostatic interactions or chemisorbed through gold-thiol bonds. As a large number of MB is present in the hot spots, where local surface plasmon resonance is induced, a strong SERRS signal for MB is observed. **(B)** In the presence of thrombin, TBA changes conformation into a G-quadruplex form and physisorbed TBA is thus displaced from the surface, resulting in the prompt decrease of the SERRS signal. **(C)** GNP-substrate is prepared by aggregating citrate-coated GNPs on an APTES-treated glass substrate. **(D)** TBA-GNP substrate is prepared by immobilizing MB-conjugated TBA on the GNP-substrate followed by a rinsing step removing unbounded TBA. **(E)** Thrombin is incubated on the prepared TBA-GNP substrate followed by a rinsing step removing displaced TBA-thrombin complex.

Materials 3’ Methylene blue-tagged DNA oligonucleotides were synthesized by Biosearch Technologies, Inc. (Novato, CA), purified via RP-HPLC, and confirmed by mass spectroscopy to be >95% pure. The sequences of these two aptamer oligonucleotides and thrombin binding buffer solution employed in the experiment are given below:
Thrombin Binding Aptamer (TBA):
5′-(CH2)6-S-S-(CH2)6-TAA GTT CAT CTC CCC GGT TGG TGT GGT TGG T–MB-3′
non-thrombin binding oligonucleotide (Mutant TBA):
5′-(CH2)6-S-S-(CH2)6-TAA GTT CAT CTC CCC AAT TGG TGT GGT TAA T–MB-3′
1x Thrombin Binding Buffer (TBB):
140 mM NaCl, 5 mM KCl, 1 mM $MgCl_2$, 1 mM CaCl2, 20 mM Tris-acetate at pH 7.4
Methylene blue active ester was used for coupling to the amine group of the oligonucleotide (3' C7 amine CPG purchased from Glen Research, Sterling, Virginia). Human alpha-thrombin was purchased from Haematologic Technologies Inc. (Essex Junction, VT) in a powder form and was diluted with deionized water (DI water) to obtain desired stock concentration. 99% 3-Aminopropyltriethoxysilane (APTES), fetal calf serum and bovine serum albumin (BSA) were purchased from Sigma-Aldrich, Co. (St. Louis, MO). An appropriate amount of BSA was dissolved in DI water to obtain desired stock concentration. A solution of gold nanoparticles (80 nm in diameter) was purchased from TED Pella, Inc., (Redding, CA) and PDMS membrane (HT 6240, 256 μm in thickness) was purchased from Rogers Corporation (Woodstock, CT).

Preparation of aptasensor The SERRS substrate was fabricated by first fixing aggregated GNPs on a glass side. The slide was thoroughly rinsed with acetone and isopropyl alcohol (IPA) sequentially and then modified with amino-terminal group by immersion in APTES (10% v/v with IPA) for 10 minutes followed by rinsing with IPA and drying with N_2 gas. A 14 μL mixture (50:1 v/v) of GNP solution and aggregation agent, 10 mM $CuSO_4$, was spotted on the modified slide (3 mm in diameter) defined by a PDMS membrane and dried at 60°C for 40 minutes. Unfixed GNPs were removed by rinsing the substrate three times with 10 μL of DI water. Both MB-tagged TBA and MB-tagged mutant TBA in 1x TBB at the concentration of 100 μM were then immobilized on the GNP-substrate by incubating overnight at room temperature in a dark room. The unbound aptamers were subsequently removed via repeated rinsing five times with 10 μL 1x TBB. Protein (in TBB or serum) was introduced on the aptamer-immobilized SERRS substrate by dropping 10 μL and incubating for 1 hour at room temperature in the dark room. The displaced TBA and protein were subsequently removed via repeated rinsing five times with 10 μL 1x TBB.

Experimental conditions An inverted microscope (Zeiss, Axiovert S100TV) was coupled with a helium-neon laser (LHRP-0501, 632.8 nm in wavelength, Research Electro Optics Inc., Boulder, CO), a spectrograph (SpectraPro 300i) equipped with a back-thinned LN-cooled CCD camera (Roper Scientific, Spec-10:100B (LN)) to collect spectra and a closed-loop X-Y piezo stage (Physik Instrumente) equipped with an avalanche photodiode (EG&G, SPCM-AQR-14), where both fluorescence and Raman scattering light were focused on through a 100-μm pinhole to take scanning image. The laser focused on and scattering from the SERRS substrate passed through a high numerical aperture oil immersion objective lens (Zeiss, Plan-Achromat 100X, N/A. 1.4). The spectra were analyzed by software (WinSpec/32, Roper Scientific) and the control of the stage and image analysis was done by software (Digital Instruments, Nanoscope IIIA). The SERRS spectra were measured with the laser of the power 10 μW and 10 s of integration time and the scanning was performed with laser power of 1 μW. The optical equipment was calibrated by measuring the Raman spectrum of a control sample (100% Toluene solution) before every experiment. To minimize the variation of signal with respect to the number of aggregated GNPs, the data were collected by shining the laser on GNP aggregates larger than the laser spot four times and averaging.

4.4 CHARACTERIZATION

The spectra were collected from aggregated GNPs in a fractal structure (Fig. 4.4A inset, SEM image). The whole spectra are displayed after subtracting the fluorescence background from the original signal (Fig. 4.4A) for clarity and the most prominent Raman peak at 1622 cm^{-1} (assigned to ν(CC) ring and ν(CNC) ring modes of methylene blue)[38] was compared for quantitative analysis (Fig. 4.4B, 4.4C). The effect of adding thrombin to the aptamer can clearly be observed through the reduction of the peak's intensity at the 1622 cm^{-1}. Initially, the peak's intensity dropped approximately 10% when introduced with 100 pM thrombin. However, with ≥ 1 μM thrombin concentration, the intensity dropped to about 50 %, the observed saturation level (Fig. 4.4C). We thus estimate the limit of detection for this assay to be 100 pM with a dynamic range spanning 100 pM to 1 μM.

To verify that the signal change is dependent on the specific recognition of thrombin, we added a nonspecific binding protein, bovine serum albumin (BSA). When the substrate was treated with increasing concentration of BSA (up to 1 μM BSA), we did not observe any significant change in the SERRS signal (Fig. 4.4C). This suggests that the TBA was not displaced from the GNP substrate, as TBA did not bind to BSA. The specificity of the aptamer-based SERRS method was further investigated with a mutant TBA [5′-$(CH_2)_6$-S-S-$(CH_2)_6$-TAA GTT CAT CTC CCC **AA**T T**GG** TGT **GG**T T**AA** T–MB-3′] (nucleotides marked in bold indicate the position of essential "G" in the original aptamer sequence) in 1x TBB (Fig. 4.5). Upon the addition of 100 nM thrombin to the mutant TBA-GNP substrate, we did not observe any decrease in the SERRS signal intensity. Taken together, these observations suggest that the displacement mechanism relies on specific recognition and that the aptamer-based SERRS method is highly specific for the detection of TBA-thrombin interaction.

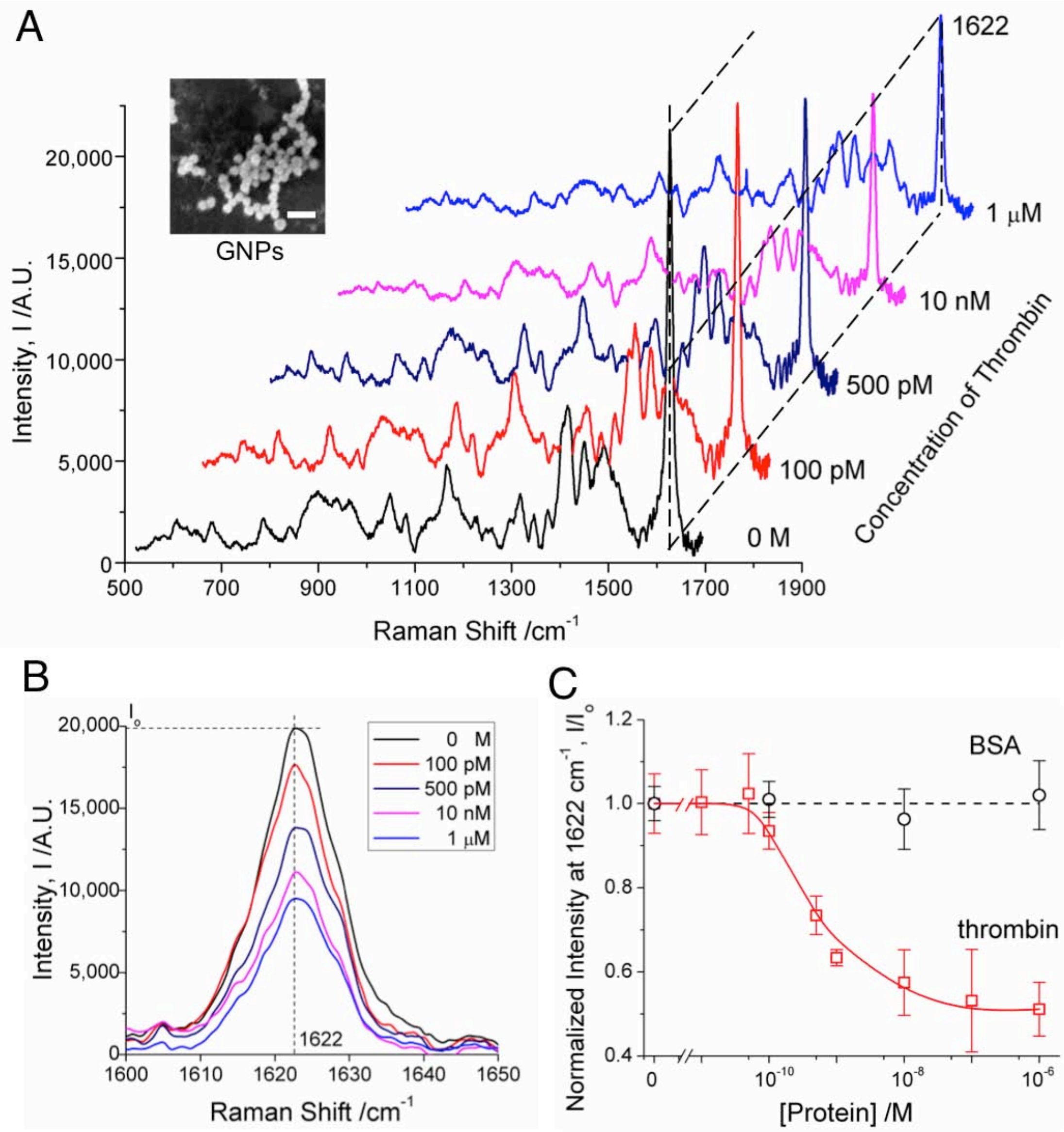

Figure 4.4 Thrombin is quantitatively detected by measuring the SERRS signal drop for MB conjugated with TBA. (A) The SERRS intensity of MB decreases with the increasing thrombin concentration. **(B)** The most prominent peak of MB, observed at 1622 cm^{-1}, was compared upon addition of varying concentrations of thrombin. The limit of detection was estimated to be 100 pM. **(C)** The SERRS signal drop was proportional to the thrombin concentration and reached a saturation level at 1 μM thrombin. However, the intensity was unaffected with increasing BSA concentrations up to 1 μM. Scale bar in an inset is 200 nm. Note that the y-axis, i.e. normalized intensity (I/I_o), was plotted as a ratio of the measured intensity at each protein concentration over the intensity without thrombin in 1x thrombin-binding buffer solution. Data shown represents the mean, with standard deviation, of four separate measurements.

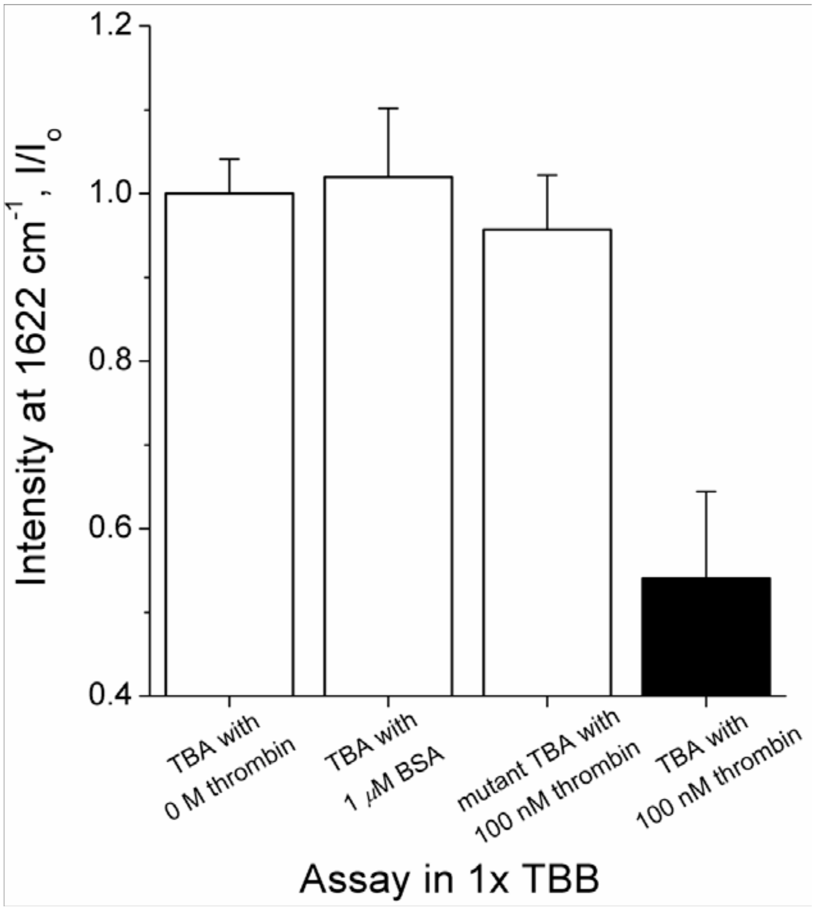

Figure 4.5 Evaluation on the specificity of the developed method and the aptamer-based SERRS nanosensor. Assays were performed in 1x TBB. We did not observe any significant intensity change in SERRS signal from the TBA-GNP substrate in 1 μM BSA or from the mutant TBA on GNP substrate in 100 nM thrombin. In contrast, the SERRS signal drop was clearly distinguishable for the TBA-GNP substrate incubated with 100 nM thrombin. Data shown represents the mean, with standard deviation, of four separate measurements.

The stability of the nanosensor was evaluated in the presence of complex mixtures including nucleases, i.e. serum (Fig. 4.6). We observed ~20 % signal decrease when the substrate was treated with 10 % fetal calf serum (*v/v* in TBB), indicating that the TBA was minimally displaced from the aggregated GNPs by the serum's constituents; the SERRS signal drop reached the 50 % saturation in 75 % serum. We hypothesize that the displacement of TBA in elevated serum levels was probably due to stronger electrostatic interference by serum's salt contents rather than by nuclease activity in the serum, which are unlikely to degrade the immobilized, 5'- and, 3'-capped TBA.[39] With this "serum baseline," the intensity in the presence of 10% serum, we proceed to introduce thrombin to both the TBA-GNP substrate and the mutant TBA-GNP substrate. With the addition of 1 nM thrombin in 10% serum to the TBA-GNP substrate, the signal dropped ~25 % from the serum baseline, and the signal further decreased to a saturating level of 60 % when the thrombin concentration increased to 100 nM. In contrast, the mutant TBA-GNP substrate did not produce any significant signal change when exposed to 1 nM thrombin in 10% serum. These observations collectively indicate that the nanosensor can be performed in the presence of 10% serum. We also note that mutant TBA-GNP substrate is unaffected by nucleases in serum. Thus, the mutant aptamer both effectively and conveniently provides a "negative control" that enables specific protein detection for each respective assay performed in 10% serum.

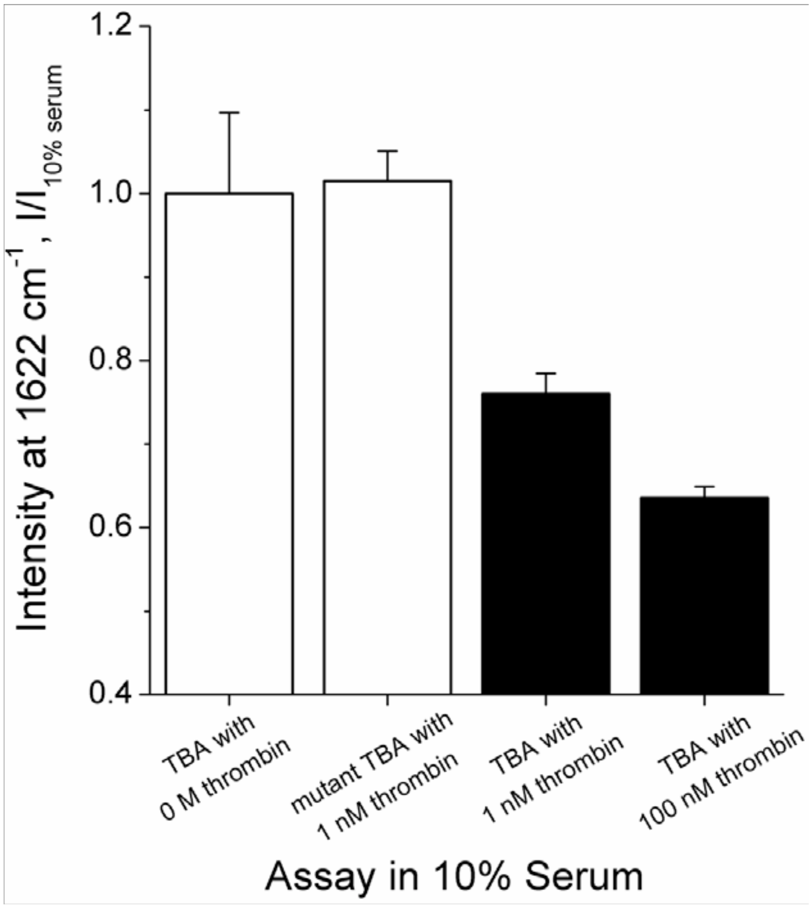

Figure 4.6 Evaluation on the reliability of the developed method and the aptamer-based SERRS nanosensor. Assays were performed in 10% fetal calf serum (v/v in 1x thrombin binding buffer). Based on a "serum baseline at 10% serum," the signal dropped to ~75% with the addition of 1 nM thrombin in 10% serum, while the signal dropped to a saturating level of 60% when the input thrombin was increased to 100 nM. Mutant TBA-GNP substrate was unaffected with the input of 1 nM thrombin. Note that the y-axis, i.e. normalized intensity ($I/I_{10\%\ \mathrm{serum}}$), was plotted as a ratio of the measured intensity at each protein concentration over the intensity without thrombin in 10 % serum. Data shown represents the mean, with standard deviation, of four separate measurements.

The 50% saturation level can be attributed to the chemisorbed aptamer population. To verify that the signal was stemming only from chemisorbed aptamer, we repeatedly subjected the substrate to harsh conditions: high NaCl (1.4 M), high serum (100%) wash, and high thrombin (1 μM) interaction (Fig. 4.7). In all cases we observed a 50% maximum signal reduction, suggesting that ~50% of the aptamer is chemisorbed onto the GNPs and is, therefore, resistant to displacement via disruption of electrostatic interactions rather than the denaturation of TBA.

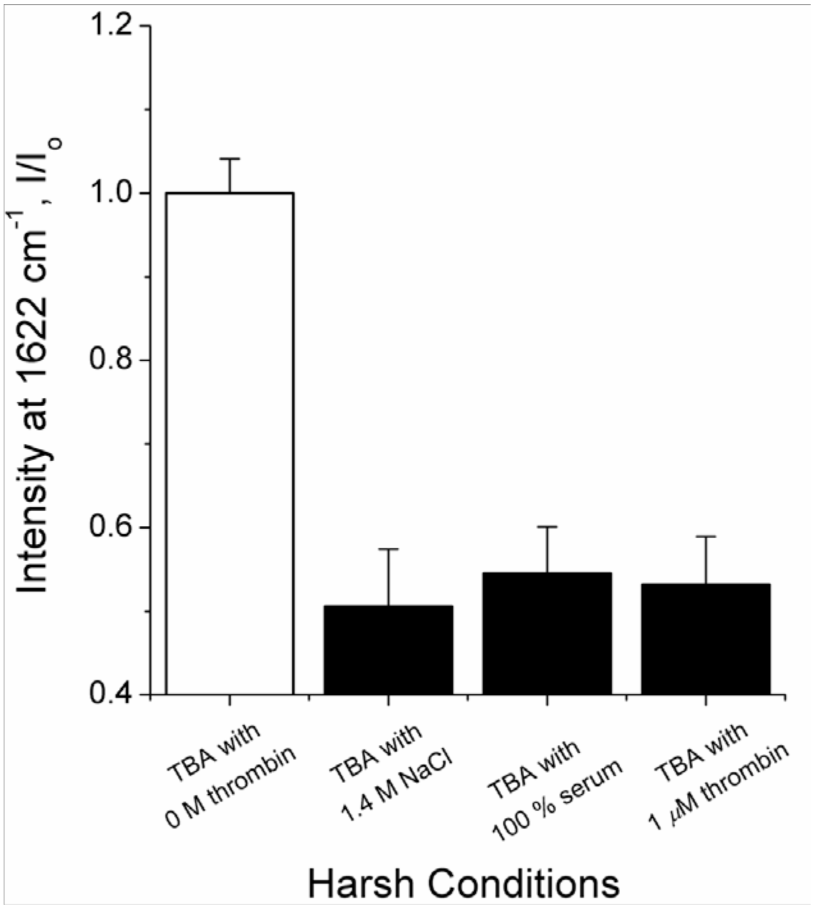

Figure 4.7 Evaluation of 50% signal saturation. The relative intensity of most prominent signal afforded by MB, measured at 1624 cm^{-1}, decreased to a saturating level ~50% under the harsh conditions: high NaCl, serum, and thrombin indicating that physisorbed TBA was removed by ion effects or thrombin-interaction.

4.5 CONCLUSIONS

In conclusion, we have demonstrated highly sensitive, selective, and stable aptamer-based SERRS nanosensor for the detection of thrombin. The limit of detection is100 pM (below the dissociation constant of TBA, 25 nM). This low limit of detection is possible because the aptamer-based SERRS signal depends on the number of aptamers displaced from the surface, not the number of aptamers that are bound to target. In addition, this assay is sufficiently stable to identify the target in the presence of 10 % serum. Given the size and simplicity of the proposed detection schematic, this method may be readily used in a miniaturized and integrated platform as it can easily accommodate numerous protein-specific aptamers with a variety of Raman probes for high throughput and multiplexed drug screening and biomedical diagnostics.

References:

(1) Ellington, A. D., Szostak, J. W., In vitro selection of RNA molecules that bind specific ligands, *Nature* **1990**, *346*, 818-822.

(2) Tuerk, C., Gold, L., Systematic evolution of ligands by exponential enrichment: RNA ligands to bacteriophage T4 DNA polymerase, *Science* **1990**, *249*, 505-510.

(3) Jayasena, S. D., Aptamers: An Emerging Class of Molecules That Rival Antibodies in Diagnostics, Clinical Chemistry **1999**, *45*, 1628-1650.

(4) Sullenger, B. A., Gilboa, E., Emerging clinical applications of RNA, *Nature-review* **2002**, *418*, 252-258.

(5) Pestourie, C., Tavitian, B., Duconge, F., Aptamers against extracellular targets for in vivo applications, *Biochimie* **2005**, *87*, 921-930.

(6) Bunka, D. H. J., Stockley, P. G., Aptamers come of age - at last, *Nat Rev Micro* **2006**, *4*, 588-596.

(7) Klussmann, S., *The aptamer handbook: functional oligonucleotides and their applications*, WILEY-VCH Verlag GmbH & Co. KGaA, 2006.

(8) Fischer, N. O., Tarasow, T. M., Tok, J. B. H., Aptasensors for biosecurity applications, *Current Opinion in Chemical Biology* **2007**, *11*, 316-328.

(9) Szakacs, G., Paterson, J. K., Ludwig, J. A., Booth-Genthe, C., Gottesman, M. M., Targeting multidrug resistance in cancer, *Nat Rev Drug Discov* **2006**, *5*, 219-234.

(10) Xiao, Y., Piorek, B. D., Plaxco, K. W., Heeger, A. J., A Reagentless Signal-On Architecture for Electronic, Aptamer-Based Sensors via Target-Induced Strand Displacement, *J. Am. Chem. Soc.* **2005**, *127*, 17990-17991.

(11) Baker, B. R., Lai, R. Y., Wood, M. S., Doctor, E. H., Heeger, A. J., Plaxco, K. W., An Electronic, Aptamer-Based Small-Molecule Sensor for the Rapid, Label-Free Detection of Cocaine in Adulterated Samples and Biological Fluids, *J. Am. Chem. Soc.* **2006**, *128*, 3138-3139.

(12) Stojanovic, M. N., Landry, D. W., Aptamer-Based Colorimetric Probe for Cocaine, *J. Am. Chem. Soc.* **2002**, *124*, 9678-9679.

(13) Huang, C. C., Huang, Y. F., Cao, Z., Tan, W., Chang, H. T., Aptamer-Modified Gold Nanoparticles for Colorimetric Determination of Platelet-Derived Growth Factors and Their Receptors, *Anal. Chem.* **2005**, *77*, 5735-5741.

(14) Liu, J., Lu, Y., Preparation of aptamer-linked gold nanoparticle purple aggregates for colorimetric sensing of analytes, *Nat. Protocols* **2006**, *1*, 246-252.

(15) Bagalkot, V., Zhang, L., Levy-Nissenbaum, E., Jon, S., Kantoff, P. W., Langer, R., Farokhzad, O. C., Quantum Dot-Aptamer Conjugates for Synchronous Cancer Imaging, Therapy, and Sensing of Drug Delivery Based on Bi-Fluorescence Resonance Energy Transfer, *Nano Lett.* **2007**, *7*, 3065-3070.

(16) Xiao, Y., Lubin, A. A., Heeger, A. J., Plaxco, K. W., Label-Free Electronic Detection of Thrombin in Blood Serum by Using an Aptamer-Based Sensor, *Angewandte Chemie International Edition* **2005**, *44*, 5456-5459.

(17) Radi, A. E., AceroSanchez, J. L., Baldrich, E., O'Sullivan, C. K., Reagentless, Reusable, Ultrasensitive Electrochemical Molecular Beacon Aptasensor, *J. Am. Chem. Soc.* **2006**, *128*, 117-124.

(18) Wei, H., Li, B., Li, J., Wang, E., Dong, S., Simple and sensitive aptamer-based colorimetric sensing of protein using unmodified gold nanoparticle probes, *Chemical Communications* **2007**, 28, 3735-3737.

(19) Fang, X., Sen, A., Vicens, M., Tan, W., Synthetic DNA Aptamers to Detect Protein Molecular Variants in a High-Throughput Fluorescence Quenching Assay, *ChemBioChem* **2003**, *4*, 829-834.

(20) Shlyahovsky, B., Li, D., Weizmann, Y., Nowarski, R., Kotler, M., Willner, I., Spotlighting of Cocaine by an Autonomous Aptamer-Based Machine, *J. Am. Chem. Soc.* **2007**, *129*, 3814-3815.

(21) Wang, Y., Wei, H., Li, B., Ren, W., Guo, S., Dong, S., Wang, E., SERS opens a new way in aptasensor for protein recognition with high sensitivity and selectivity, *Chemical Communications* **2007**, 5220-5222.

(22) Chen, J.-W., Liu, X.-P., Feng, K.-J., Liang, Y., Jiang, J.-H., Shen, G.-L., Yu, R.-Q. *Biosensors and Bioelectronics* **2008**, *In Press, Corrected Proof.*

(23) Li J. J., Fang X, Tan W., Molecular aptamer beacons for real-time protein recognition, *Biochem. Biophys. Res. Commun.* **2002**, 292, 31–40.

(24) Vairamani, M., Gross, M. L., G-Quadruplex Formation of Thrombin-Binding Aptamer Detected by Electrospray Ionization Mass Spectrometry, *J. Am. Chem. Soc.,* **2003**, 125, 42-43.

(25) Robert J. Stokes *et al.*, Quantitative Enhanced Raman Scattering of Labeled DNA from Gold and Silver Nanoparticles, *Small* **2007**, 3, 1593-1601.

(26) Nie, S., Emory, S. R., Probing Single Molecules and Single Nanoparticles by Surface-Enhanced Raman Scattering, *Science* **1997**, 275, 5303, 1102 – 1106.

(27) Li, H., Rothberg, L., Colorimetric detection of DNA sequences based on electrostatic interactions with unmodified gold nanoparticles, *PNAS* **2004**, *101*, 14036-14039.

(28) Li, H., Rothberg, L. J., DNA Sequence Detection Using Selective Fluorescence Quenching of Tagged Oligonucleotide Probes by Gold Nanoparticles, *Anal. Chem.* **2004**, *76*, 5414-5417.

(29) Bock, L. C., Griffin, L. C., Latham, J. A., Vermaas, E. H., Toole, J. J., Selection of single-stranded DNA molecules that bind and inhibit human thrombin, *Nature* **1992**, *355*, 564-566.

(30) Vairamani, M., Gross, M. L., G-Quadruplex Formation of Thrombin-Binding Aptamer Detected by Electrospray Ionization Mass Spectrometry, *J. Am. Chem. Soc.* **2003**, *125*, 42-43.

(31) Yau, H. C. M., Chan, H. L., Sui, S. f., Yang, M., Integrity and redox properties of homogeneous and heterogeneous DNA films on gold surface probed by cyclic voltammetry, *Thin Solid Films* **2002**, *413*, 218-223.

(32) Herne, T. M., Tarlov, M. J. *J.,* Characterization of DNA Probes Immobilized on Gold Surfaces, *Am. Chem. Soc.* **1997**, *119*, 8916-8920.

(33) Gearheart, L. A., Ploehn, H. J., Murphy, C. J., Oligonucleotide Adsorption to Gold Nanoparticles: A Surface-Enhanced Raman Spectroscopy Study of Intrinsically Bent DNA, *J. Phys. Chem. B* **2001**, *105*, 12609-12615.

(34) Nicolai, S. H. A., Rubim, J. C., Surface-Enhanced Resonance Raman (SERR) Spectra of Methylene Blue Adsorbed on a Silver Electrode, *Langmuir* **2003**, *19*, 4291-4294.

(35) Stokes, Robert J., Macaskill, A., Lundahl, P. J., Smith, W. E., Faulds, K., Graham, D., Quantitative Enhanced Raman Scattering of Labeled DNA from Gold and Silver Nanoparticles, *Small* **2007**, *3*, 1593-1601.

(36) Bell, S. E. J., Sirimuthu, N. M. S., Surface-Enhanced Raman Spectroscopy as a Probe of Competitive Binding by Anions to Citrate-Reduced Silver Colloids, *J. Am. Chem. Soc.* **2005**, *109*, 7405-7410.

(37) Weitz, D. A., Oliveria, M., Fractal Structures Formed by Kinetic Aggregation of Aqueous Gold Colloids, *Physical Review Letters* **1984**, *52*, 1433-1436.
(38) Nicolai, S. H. d. A., Rodrigues, P. R. P., Agostinho, S. M. L., Rubim, J. C., Electrochemical and spectroelectrochemical (SERS) studies of the reduction of methylene blue on a silver electrode, *Journal of Electroanalytical Chemistry* **2002**, *527*, 103-111.
(39) Ruckman, J., Green, L. S., Beeson, J., Waugh, S., Gillette, W. L., Henninger, D. D., Claesson-Welsh, L., Janjic, N., 2′-Fluoropyrimidine RNA-based Aptamers to the 165-Amino Acid Form of Vascular Endothelial Growth Factor ($VEGF_{165}$), *J. Biol. Chem.* **1998**, *273*, 20556-20567.

CHAPTER 5:
CANCER DIAGNOSTICS USING VEGF_{165} APTASENSOR

Cancer diagnostics using biofluids (i.e., whole blood, plasma, serum, and saliva) of cancer patients at risk are in critical demand, particularly for early detection of cancer biomarkers and towards eventual prevention or mitigation of metastasis. Here, we present aptamer based nanoplasmonic sensor, 'aptasensor' targeting vascular endothelial growth factor-165 (VEGF_{165}), a predominant cancer biomarker for various solid cancers by utilizing a single-step aptamer-molecule interaction for target recognition and a metal-fluorophore interaction for signal enhancement in a nanometer scale. The aptasensor provides the appropriate sensitivity for clinical diagnostics with a wide range of linear detection range from 125 pg/mL to 2.5 μg/mL and high specificity for VEGF_{165} against PDGF-BB, OPN, NaCl, and VEGF_{121}. Also, we demonstrate its capability of cancer diagnostics using patient samples by observing the higher level of signal change in serum from breast cancer patients by 20 % compared to normal women, indicating that more VEGF_{165} are present in the breast cancer patients.

5.1 INTRODUCTION

Cancer diagnostics using biofluids of cancer patients at risk are in critical demand, particularly for early cancer detection and towards eventual prevention or mitigation of metastasis.[1,2] Currently, most cancer diagnostics rely on enzyme-linked immunosorbent assay (ELISA). However, the ELISA method requires large volumes of biofluids, multi-step assays with associated long incubation times, and expensive reagents. Alternative aptamer-based sensing methods include electric,[3,4] optical,[5-7] or magnetic[8,9] monitoring of cancer biomarkers. These methods still have the limiting factors for practical cancer diagnostics: the requisition of large sample volume (electric and optical methods) or multi-step assays (magnetic method). In this paper, we present an aptamer-based nanoplasmonic sensor, 'aptasensor' utilizing a single-step aptamer-molecule interaction for target recognition[10,11] and a metal-fluorophore interaction for signal enhancement in a nanometer scale.[12,13] The aptasensor is sensitive, specific for vascular endothelial growth factor-165 (VEGF_{165}), a predominant cancer biomarker of various solid cancers,[14,15] and applicable for cancer diagnostics.

5.2 PRINCIPLES

VEGF over-secretion from tumors VEGF is an endothelial cell-growing factor and an angiogenic mediator of pathological angiogenesis in a variety of solid tumors. VEGF is regarded to be responsible for inducing a neovascularization and thus for delivery of nutrients to the growing tumor (Fig 5.1).[16] For example, hypoxia-regulated VEGF is over-released in the progression of the retinal vasculature, resulting in development of the superficial and deep layers of retinal vessels.[17] The over-expression of VEGF has been monitored by measuring circulating VEGF in serum or plasma.[18]

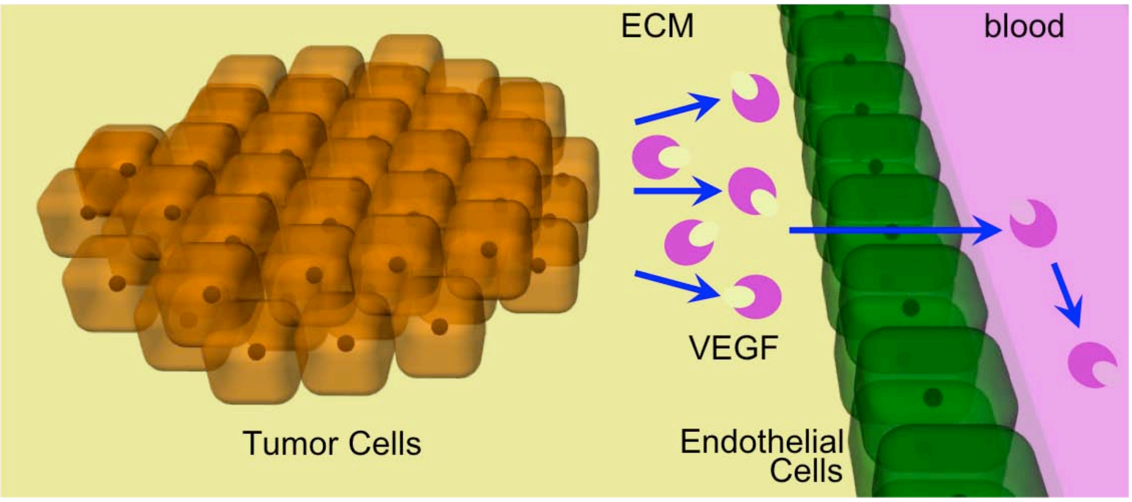

Figure 5.1 Schematic representation and kinetics of target detection.

Conformation change in aptamer upon target binding Aptamers have the properties: sensitivity, specificity, and stability over antibodies. Also, the target-binding event induces the change of secondary structures in the aptamer (Fig. 5.2), of which property has been monitored by optical, electrical, magnetic ways.

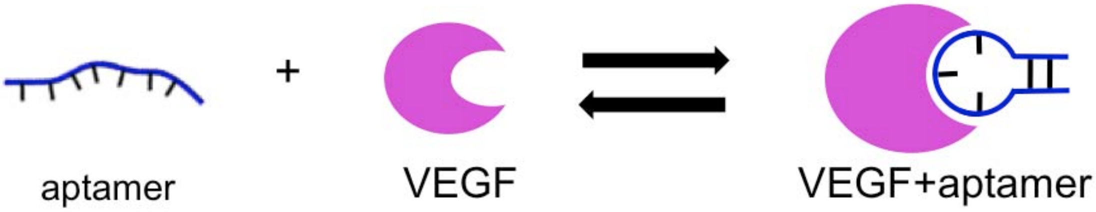

Figure 5.2 Schematic representation and kinetics of target detection.

Metal-fluophore interaction Contrary to the relatively constant radiative rates in free solution, it is known that the radiative rates can be increased or decreased affected by the presence of fluorophores depending on distances from metallic surfaces. These effects are caused by the dople of fluorophore interacting with free electrons on the surface. These interactions change the intensity and temporal and spatial distribution of the radiation. The appropriate localization of fluorophores near particles can result in usefully high emission from "nonfluorescent" molecules and million-fold increases in the number of photons observable from each fluorophore. [q4]

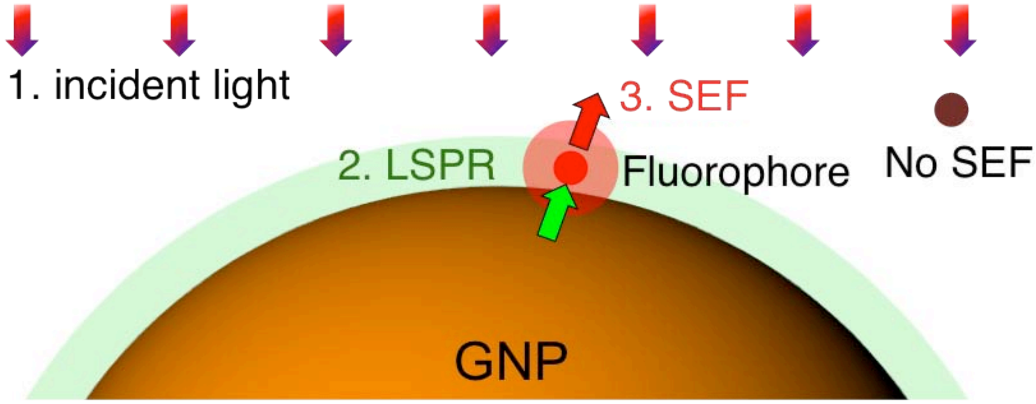

Figure 5.3 Schematic representation and kinetics of target detection.

5.3. DESIGN

Detection mechanism Negatively charged citrate-coated gold nanoplasmonic particles (GNPs) are fixed on a positively charged amino-silane (APS)-coated glass slide and positively charged poly-L-lysine (PLL) is added on top of GNPs not only to immobilize more aptamers made of negatively charged single stranded RNA but also to provide a spacing layer avoiding quenching.[6] To directly monitor the event of target binding without requiring an additional labeling step, VEGF$_{165}$-specific aptamer is conjugated with a fluorescent molecule, Cy3B, which has an absorption peak wavelength (λ = 552 nm) that matches with a localized surface plasmon resonance (LSPR) peak wavelength of a spherical GNP 80 nm in diameter ($\lambda \approx 550$ nm). The aptamer complex is immobilized on the PLL-GNP surface with an electrostatic force, F$_E$. In the absence of target VEGF$_{165}$ molecules, Cy3B is spaced at a relevant coupling distance from the GNP surface for LSPR to induce surface enhanced fluorescence (SEF) (Fig. 5.4A).

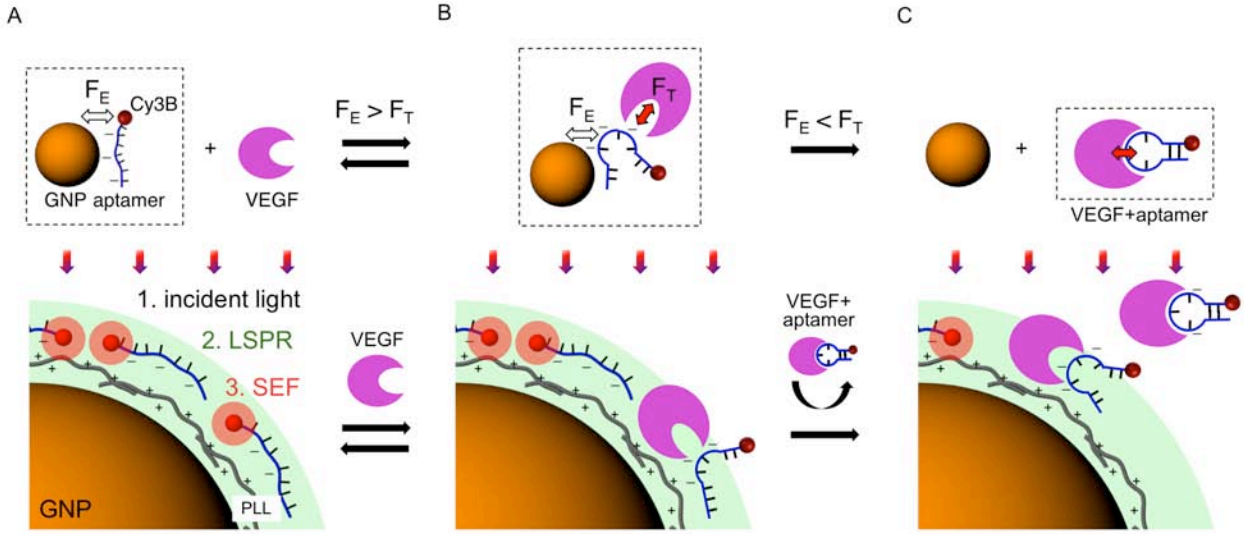

Figure 5.4 Schematic representation and kinetics of target detection.

In the presence of a $VEGF_{165}$ molecule, however, the aptamer tends to form a thermo-dynamically stable secondary structure, represented by a target binding force, F_T. In case that the binding force is stronger than the electrostatic force, the aptamer undergoes a conformational change causing the negatively charged aptamer to less contribute to the immobilizing electrostatic force (Fig. 5.4B). The loss of the electrostatic force leads to the subsequent detachment of aptamers from the GNP surface and signal enhancement is precluded (Fig. 5.4C).[19] Therefore, the concentration of $VEGF_{165}$ molecules can be estimated by measuring the amount of signal change in the fluorescence intensity.

Preparation of aptasensor A glass slide was cleaned with Piranha (3:1 concentrated sulfuric acid to 30% hydrogen peroxide solution) for 10 minutes, thoroughly washed with DI water, and then dried by a nitrogen gun. After the cleaning, the glass slide was coated with amino-terminal groups by immersing in a diluted APS solution (1% v/v in 100% ethanol) for 5 minutes at room temperature, rinsing with ethanol, and drying it gently with a nitrogen gun without leaving any trace marks. Baking for 5 minutes at 125°C was applied to further stabilize the amino-group layer. Arrayed holes of 3mm in diameter were patterned on a thin poly (dimethyl-siloxane) (PDMS) membrane (HT 6240) by using the laser-engraving machine (VersaLaser). The PDMS membrane was cleaned with ethanol followed by drying with N2 gas and in an oven at 60°C for 10 minutes and then treated with UV/Ozone (UVO Cleaner Model 42, Jelight, Irvine, CA) for 3 minutes to elevate the surface energy.[20] Right after the UV/Ozone treatment, the membrane was coated with epoxy-terminal groups by immersing in a diluted GPS solution (1% v/v in 100% ethanol) for 20 minutes at room temperature, rinsing with ethanol, and drying it gently with a nitrogen gun. The positively charged glass slide treated with APS and the negatively charged PDMS membrane treated with GPS were immediately contacted for bonding and then incubated for 1 hour at room temperature. GNP stock solution was sonicated (30 seconds) for even distribution in the stock solution before dropping. 10 μl of the GNP solution was dropped at an opening area defined by the hole on the PDMS membrane and incubated for 1 hour at 4°C in a humidity chamber. Unbound GNPs were washed off by rinsing the slide in distilled water and then drying in a centrifuge (IEC clinical centrifuge, International Equipment Co., Needham, MA). 10 μl of PLL (70kDa M.W., 0.1% in distilled water) was dropped at the opening area and incubated for 10 minutes at room temperature in the humidity chamber. Unbound PLL was washed off by rinsing the slide in distilled water and then drying in a centrifuge. Apatmers were fully dehybridized and stretched by heating to 90˚C for 2 minutes in a dry block heater (HeatBlock I, VWR International, LLC, West Chester, PA) above a calculated melting temperature of 64˚C. 10 μl of the aptamer solution was dropped immediately at the opening area and incubated for 1 hour at 70˚C in the humidity chamber. Unbound aptamers were gently washed off by rinsing the slide in PBS and then drying in a centrifuge. For assay, 10 μl samples (biofluids, VEGF165, and other molecules) were dropped at the opening area and incubated for 1 hour at room temperature in the humidity chamber. Detached aptamers and unbound molecules are washed off by gently pippetting each sensor with 10 μl PBS while avoiding cross-contamination.

Preparation of biofluids 7 non-smoking participants were recruited at the GCRC, Penn State College of Medicine, Hershey, PA for this study. All the subjects involved in this study signed the institutional review board–approved consent form. Three healthy women with no known breast disease were included as normal controls and four women with breast cancer had diagnoses ranging from infiltrating ductal carcinoma, ductal carcinoma in situ, to invasive cribiform carcinoma, and invasive lobular carcinoma. All of the breast cancer patients were recently diagnosed and had not received any prior treatment in the form of chemotherapy, radiotherapy, surgery, or alternative remedies before sample collection. The mean ages for breast cancer patients and healthy controls were 43.0 ± 5.1 yr and 50.3 ± 3.5 yr ($P > 0.05$, Student's t test), respectively. Fasting blood and stimulated whole saliva samples using base-gum (a gift from Wrigley's) and blood samples were collected. Separated serum and centrifuged saliva (12,000 rpm for 10 minutes) were stored at -80ºC until used. Prior to analysis, serum and saliva samples were diluted in normal saline (0.9% NaCl).

Lifetime measurement A home-built sample scanning confocal microscope (TE300, Nikon Instruments Inc., Melville, NY) was equipped with a pulsed diode laser (LDH-P-C-470B, PicoQuant GmbH, Berlin, Germany) 470 nm in wavelength, a time-correlated single photon counting module (PicoHarp 300, Picoquant GmbH, Berlin, Germany), and a piezo scanning stage (Nano-LP 200, Mad City Labs Inc., Madison, WI). A fluorescent molecule, Cy3B conjugated with aptamer was excited by the laser with a power of 2 μW and a pulse rate of 40 MHz. The fluorescence was excited and collected through an oil immersion objective lens (Plan Apochromat, 60×, N/A=1.4, Nikon), and filtered with a 580 nm bandpass filter (580DF60, Omega Optical Inc., Brattleboro, VT). The photons were detected with an avalanche photodiode (PDM series, Micro Photon Devices, Bolzano, Italy), and the time delay between the laser pulse and the photons were measured using the PicoHarp 300. From each measurement we acquired images for 10 seconds, performing a line scan over 100 μm. After the measurement, the lifetimes were fitted by a sum of exponentials, accounting for a measured instrument response.

Fluorescence imaging An inverted microscope (TE2000-E, Nikon Instruments Inc., Melville, NY) was coupled with a mercury lamp (1x HBO 103w/2, OSRAM, München, Germany) and a monochrome CCD camera (Cascade 512B, Photomatrics, Tucson, AZ). The lights were filtered with a TRITC fluorescence filter set (EX: 528-553 nm, DM: 565nm, BA: 578-633nm) through an objective lens (Plan Fluor, 20×, N/A = 0.45, Nikon). The fluorescent images of aptasensors were acquired with a software (Image-pro Express, Media Cybernetics, Inc., Bethesda, MD) with an acquisition time of 200 ms and a gain factor of 3, and then stored in a 16-bit depth monochrome image.

Dark field imaging An inverted microscope (Axiovert 200, Carl Zeiss, Göttingen, Germany) was equipped with a white light illumination (Xenon Light Source 610, KARL STORZ GmbH & Co. KG, Tuttlingen, Germany), a wet dark-field condenser ($1.2 < NA < 1.4$), and a true-color digital camera (MP3.3-RTV-CLR-10, QImaging, Surrey, BC, Canada). Space between arrayed aptasensors and the condenser was filled with PBS and maintained at room temperature in a complete dark room. The true-color images of aptasensors were taken through an objective lens (LD ACHROPLAN, 40×, NA = 0.6, Zeiss), acquired with a software (QCapture Pro, Media

Cybernetics, Inc., Bethesda, MD) with an acquisition time of 100 ms and a gain factor of 1, and then stored in a 24-bit true color image.

5.4 CHARACTERIZATION

Experimental validation of target detection The kinetics of interaction of aptamer to $VEGF_{165}$ presents that the developed aptasensor could detect the presence of target, $VEGF_{165}$ and the interaction reached the saturation around 30 minutes (Fig. 5.5).

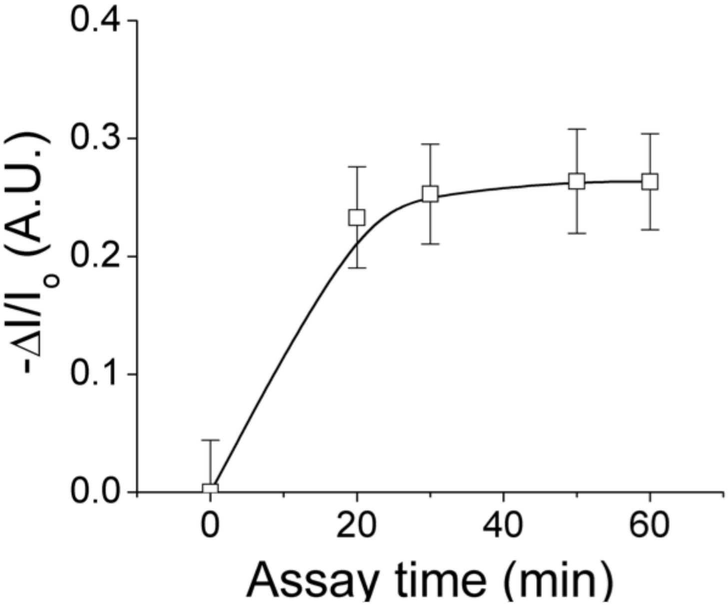

Figure 5.5 Within 30 minutes, aptasensor detects VEGF165 of 20 ng/mL

Experimental validation of SEF Signal enhancement was experimentally confirmed by observing the intensity increase by 33% and the lifetime decrease by 24% derived from the increase of the radiative decay rate of Cy3B caused by the interaction with GNPs (Fig. 3.7).[12,13]

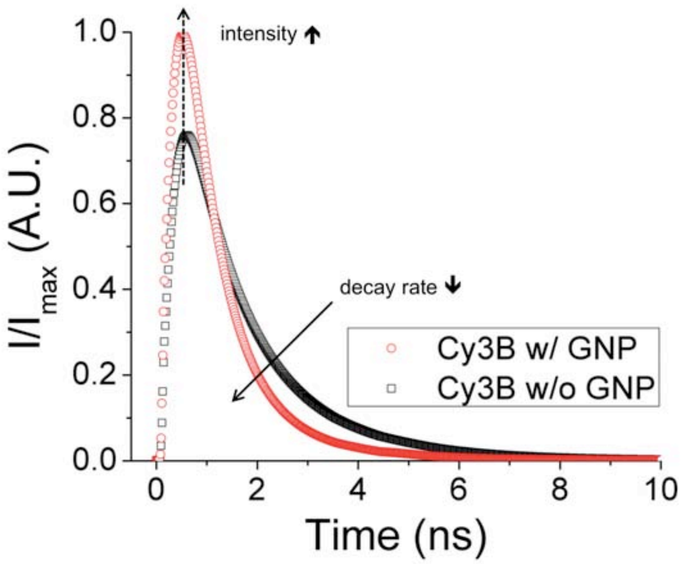

Figure 5.6 Experimental verification of SEF. The radiative decay rate of Cy3B increases by 24% due to the interaction between GNP and Cy3B (solid line). As a result, the intensity of fluorescent signal increases by 33% (dashed line).

Optimization of sensor preparation In order to maximize the signal sensitivity, PLL conditions were optimized with the variation of molecular weight and the incubation time (Fig. 5.7). The longer PLL and longer incubation time increased both sensing signals (w/ target) and the background signal (w/o target). However, the detection index, the ratio of signal change and the background signal were maximized at the intermediate conditions (5 minutes incubation time and 70 kDa molecular weight) due to the saturation of the background signal at the longer PLL and incubation time. The aptasensor was treated with VEGF_{165} at 20 pg/mL for an hour.

Sensitivity and specificity The sensitivity and specificity of the aptasensor were experimentally characterized through assays within an hour at room temperature, with 10 μL solution per assay (Fig. 5.8). The aptasensor showed discernable signal changes proportional to the concentration of VEGF_{165} over a wide range from 125 pg/mL to 2.5 μg/mL (= from 6.1 pM to125 nM) diluted in PBS at pH 7.4 (Fig. 5.8A). Limit of detection was determined at 125 pg/mL showing a signal change of 10%. Based on the experimental results, the concentration of VEGF_{165} could be estimated with an equation as: by fitting the averaged values of experiments. The aptasensor also presented a selective signal change with VEGF_{165} at 2.5 ng/mL[21] compared to other cancer-related proteins: platelet-derived growth factor (PDGF)-BB at 2.5 ng/mL[22], osteopontin (OPN) at 1.5 μg/mL[23] and a noncancer-related molecules: NaCl at 1M, VEGF_{121} at 560 pg/mL[24] (Fig. 5.8B). However, the correlation with the most abundant non-specific protein, human serum albumin (HSA) at 40 mg/ml was significant. Measured fluorescent signal changes were normalized by the value of control (the signal treated only with PBS). The cases marked with '*', '**', and '***' correspond to the assays at nominal, peak, and extraordinary high values in serum or plasma. Average and standard error were calculated with values from 4 assays for sensitivity and 3 for specificity.

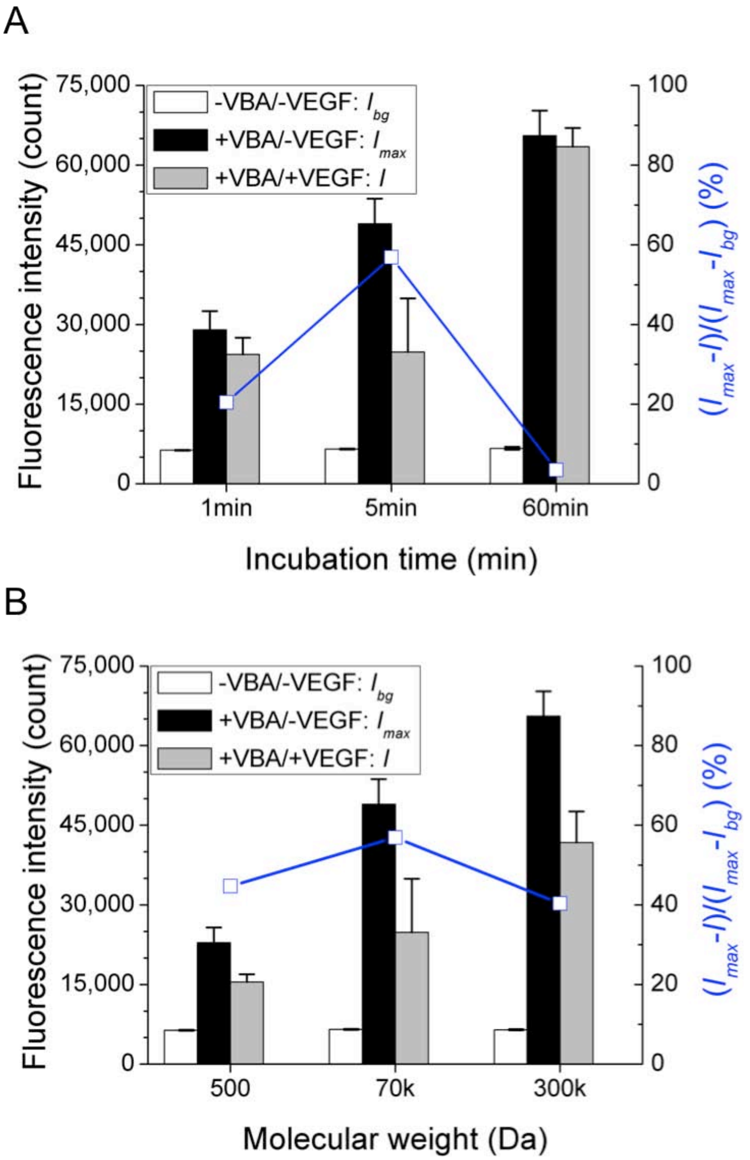

Figure 5.7 Optimization of PLL immobilization by variation of PLL molecular weight and incubation time. The performance of aptasensor is maximized at molecular weight of 70 kDa and incubation time of 5 minute.

Cancer diagnostics The aptasensor was applied to estimate $VEGF_{165}$ levels in biofluids (serum and saliva) of breast cancer patients and normal healthy women (Fig. 5.9). In general, the signal changes were proportional to the concentration of the biofluids both from breast cancer patients and normal healthy women. More positive signal changes were observed in serum solution from breast cancer patient samples, which were thought to represent the higher level of the cancer biomarker, $VEGF_{165}$. The quantitative comparison was conducted with biofluids diluted by 100 times in saline (0.9% NaCl in distilled water) and provided the relevant signal change within the relevant sensing range from 10 to 50% signal change. In serum diluted by 100 times in saline, a 20% greater signal change was observed in breast cancer samples than in normal women, indicating that the breast cancer patients had more $VEGF_{165}$. Furthermore, in the samples from breast cancer patients, 40% more change was observed in serum than saliva, indicating that serum contains more $VEGF_{165}$. Average and standard error were calculated with values from 4 breast cancer patients and 3 normal women.

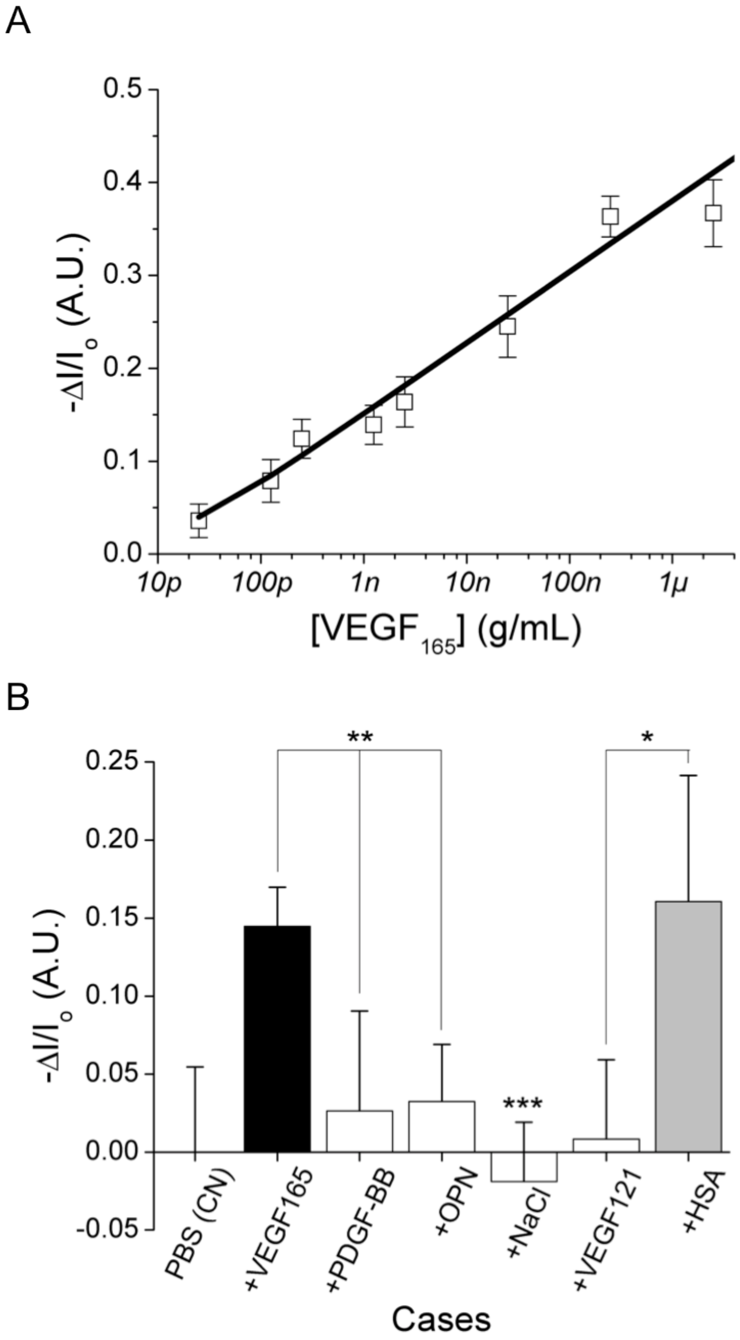

Figure 5.8 Characterization of aptasensor. (A) Aptasensor for $VEGF_{165}$ provides a wide range of detection from 125 pg/mL to 2.5 μg/mL. **(B)** The aptasensor shows the high specificity with $VEGF_{165}$ against PDGF-BB, OPN, NaCl, and $VEGF_{121}$.

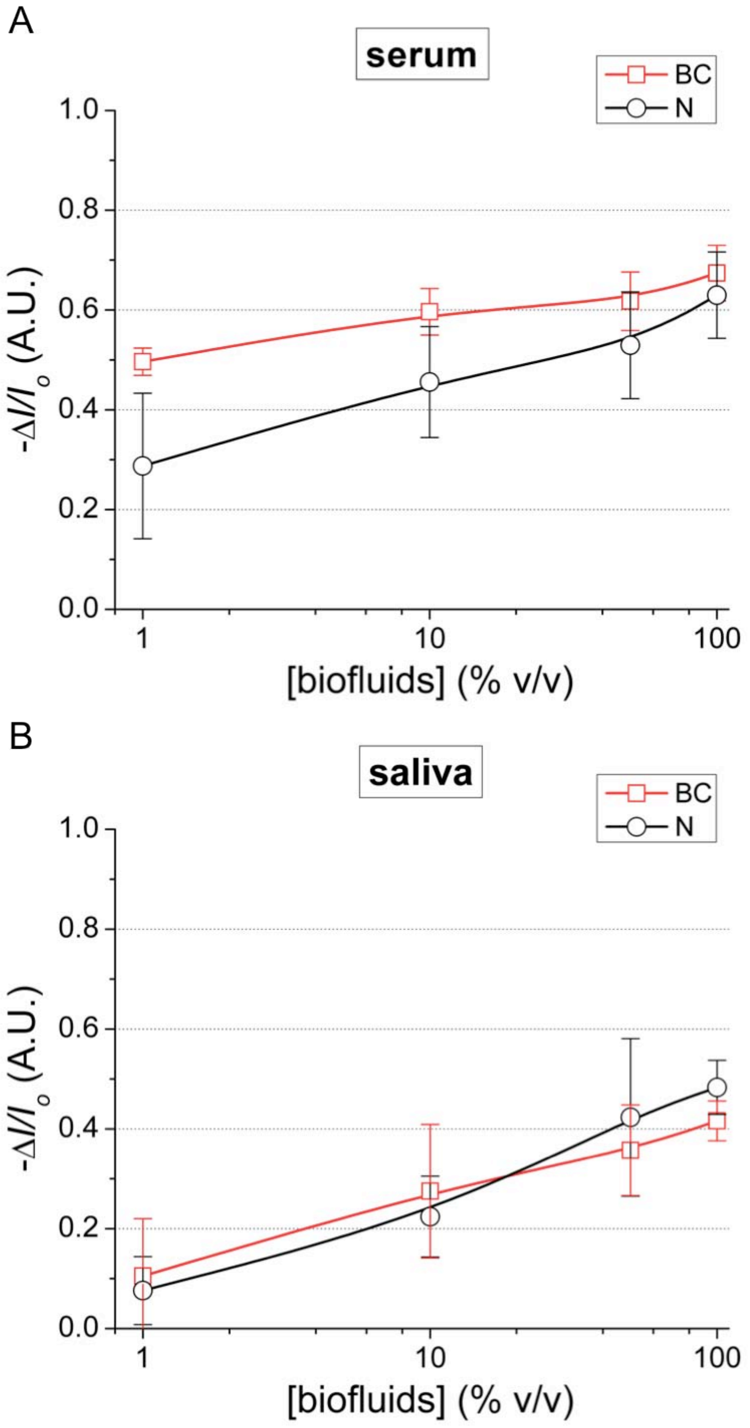

Figure 5.9 Application of aptasensor in cancer diagnostics. In breast cancer (BC) samples, further signal increase is observed in serum (A) but not significant in saliva (less than 10%) (B) compared to normal women (N).

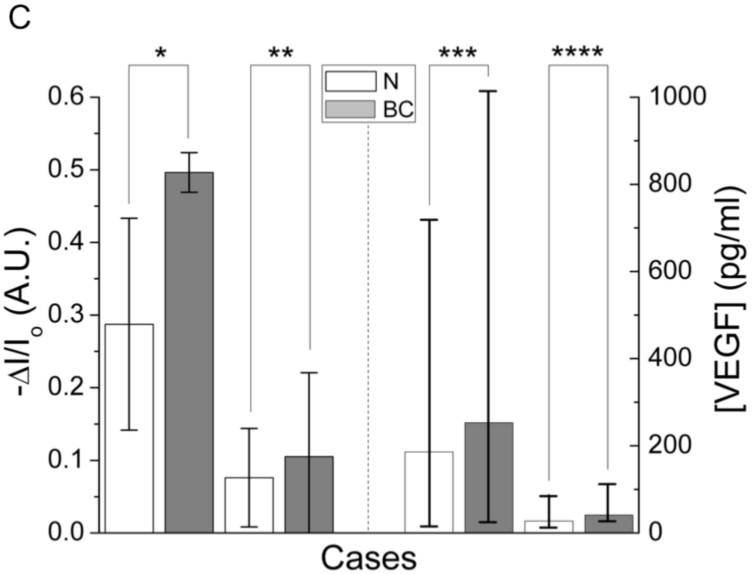

Figure 5.9 Application of aptasensor in cancer diagnostics. (C) At the dilution of 1:99 with saline, aptasensor provides distinguishable signal difference in serum samples (*), compared to saline (**) with narrower standard error compared with antibody-based diagnostics of serum (***) and plasma (****).[q3]

5.5 CONCLUSIONS

In summary, the aptasensor for $VEGF_{165}$ demonstrated target detection in a quick single-step (within an hour) with a small amount of sample solutions (less than 10 μL). In addition, the sensor provided a wide range of linear detection range from 125 pg/mL to 2.5 μg/mL, which is appropriate to clinical diagnostics. Also, the aptasensor of $VEGF_{165}$ showed strong specificity against PDGF-BB, OPN, NaCl, and VEGF121, and weak specificity against HSA, which probably elevated the signal change level in biofluids. The aptasensor showed its capability of cancer diagnostics using patient samples by observing the higher level of $VEGF_{165}$ in serum from breast cancer patients compared to healthy women. Furthermore, our demonstration shows the benefit of a low cost (7.84¢/assay), which is significant for high-throughput cancer diagnostics.

References:

(1) Etzioni, R., Urban, N., Ramsey, S., McIntosh, M., Schwartz, S., Reid, B., Radich, J., Anderson, G., Hartwell, L., The case for early detection, *Nat Rev Cancer* **2003**, 3, 243-252.
(2) Rifai, N., Gillette, M. A., Carr, S. A., Protein biomarker discovery and validation: the long and uncertain path to clinical utility, *Nat. Biotech.* **2006**, 24, 971-983.
(3) Zheng, G., Patolsky, F., Cui, Y., Wang, W. U., Lieber, C. M., Multiplexed electrical detection of cancer markers with nanowire sensor arrays, *Nat. Biotech.* **2005**, 23, 1294-1301.
(4) Swensen, J. S., Xiao, Y., Ferguson, B. S., Lubin, A. A., Lai, R. Y., Heeger, A. J., Plaxco, K. W., Soh, H. T., Continuous, Real-Time Monitoring of Cocaine in Undiluted Blood Serum via a

Microfluidic, Electrochemical Aptamer-Based Sensor, *Journal of the American Chemical Society* **2009**, 131, 4262-4266.
(5) Yang, C. J., Jockusch, S., Vicens, M., Turro, N. J., Tan, W., Light-switching excimer probes for rapid protein monitoring in complex biological fluids, *PNAS* **2005**, 102, 17278-17283.
(6) Stern, E., Vacic, A., Rajan, N. K., Criscione, J. M., Park, J., Ilic, B. R., Mooney, D. J., Reed, M. A., Fahmy, T. M., Label-free biomarker detection from whole blood, *Nat. Nano.* **2009**, 1-5.
(7) Huang, C. C., Huang, Y. F., Cao, Z., Tan, W., Chang, H. T., Aptamer-Modified Gold Nanoparticles for Colorimetric Determination of Platelet-Derived Growth Factors and Their Receptors, *Anal. Chem.* **2005**, 77, 5735-5741.
(8) Lee, H., Sun, E., Ham, D., Weissleder, R., Chip-NMR biosensor for detection and molecular analysis of cells, *Nat. Med.* **2008**, 14, 869-874.
(9) Galanzha, E. I., Shashkov, E. V., Kelly, T., Kim, J.-W., Yang, L., Zharov, V. P., In vivo magnetic enrichment and multiplex photoacoustic detection of circulating tumour cells, *Nat. Nano.* **2009**, 4, 855-860.
(10) Tuerk, C., Gold, L., Systematic evolution of ligands by exponential enrichment: RNA ligands to bacteriophage T4 DNA polymerase, *Science* **1990**, 249, 505-510.
(11) Cho, E. J., Lee, J.-W., Ellington, A. D., Annual Review of Analytical Chemistry, *Annual Review of Analytical Chemistry* **2009**, 2, 241-264.
(12) Lakowicz, J. R., Radiative Decay Engineering: Biophysical and Biomedical Applications, *Analytical Biochemistry* **2001**, 298, 1-24.
(13) Ray, K., Zhang, J., Lakowicz, J. R., Fluorescence Lifetime Correlation Spectroscopic Study of Fluorophore-Labeled Silver Nanoparticles, *Analytical Chemistry* **2008**, 80, 7313-7318.
(14) Ferrara, N., Vascular Endothelial Growth Factor: Basic Science and Clinical Progress, *Endocrine Reviews* **2004**, 25, 581-611.
(15) Mammoto, A., Connor, K. M., Mammoto, T., Yung, C. W., Huh, D., Aderman, C. M., Mostoslavsky, G., Smith, L. E. H., Ingber, D. E., A mechanosensitive transcriptional mechanism that controls angiogenesis, *Nature* **2009**, 457, 1103-1108.
(16) Ferrara, N., Vascular Endothelial Growth Factor: Basic Science and Clinical Progress, *Endocrine Reviews*, **2004**, 25, 581-611.
(17) Stone J., Itin A., Alon T., Pe'er J., Gnessin H., Chan L. T., Keshet E., Development of retinal vasculature is mediated by hypoxia-induced vascular endothelial growth factor (VEGF) expression by neuroglia, *J Neurosci*, **1995**, 15, 4738–4747.
(18) Adams, J., Vascular Endothelial Growth Factor (VEGF) in Breast Cancer: Comparison of Plasma, Serum, and Tissue VEGF and Microvessel Density and Effects of Tamoxifen, *Cancer Research,* **2000**, 60, 2898-2905.
(19) Cho, H., Baker, B. R., Wachsmann-Hogiu, S., Pagba, C. V., Laurence, T. A., Lane, S. M., Lee, L. P., Tok, J. B. H., Aptamer-Based SERRS Sensor for Thrombin Detection, *Nano Letters* **2008**, 8, 4386-4390.
(20) Lee, N. Y., Chung, B. H., Novel Poly(dimethylsiloxane) Bonding Strategy via Room Temperature ,"Chemical Gluing", *Langmuir* **2009**, 25, 3861-3866.
(21) Adams, J. *et. al.*, Vascular Endothelial Growth Factor (VEGF) in Breast Cancer: Comparison of Plasma, Serum, and Tissue VEGF and Microvessel Density and Effects of Tamoxifen, *Cancer Research* **2000**, 60, 2898-2905.
(22) Ariad, S., Seymour, L., Bezwoda, W. R., Platelet-derived growth factor (PDGF) in plasma of breast cancer patients: Correlation with stage and rate of progression, *Breast Cancer Research and Treatment* **1991**, 20, 11-17.

(23) Tuck, A. B., Chambers, A. F., The Role of Osteopontin in Breast Cancer: Clinical and Experimental Studies, *Journal of Mammary Gland Biology and Neoplasia* **2001**, 6, 419-429.
(24) Homer, J. J., Anyanwu, K., Ell, S. R., Greenman, J., Stafford, N. D., Serum vascular endothelial growth factor in patients with head and neck squamous cell carcinoma, *Clinical Otolaryngology & Allied Sciences* **1999**, 24, 426-430.

CHAPTER 6:
INTEGRATED MICROFLUIDIC PLATFORM WITH APTASENSOR

Although there are many hypotheses from clinical and laboratory data on the mechanism of growth factors in angiogenesis and metastasis, there is not yet any definitive and quantitative evidence for their efficacy. Antibody-based detection methods are limited due to their instability under long-term culturing conditions (37°C). Additionally, detection of growth factors using antibodies requires the extraction of conditioned medium, which precludes monitoring of cellular behavior in dynamic tumor microenvironments. In this section, I propose an integrated nanoplasmonic aptasensor (aptamer sensor) within a microfluidic device for on-chip label-free detection of secreted growth factor under the spatial and temporal control of a simulated tumor microenvironment. The sensor is applicable to culturing conditions owing to the stability of the aptamer at 37°C for a week. The integrated platform achieved the label-free detection of vascular endothelial growth factor (VEGF) down to 1 nM in buffer solution and also VEGF secreted from MCF-7 (human breast cancer) cells upon continuous stimulation with 0.1 mM estrodiole for 37 hrs. Additionally, there was no discernible signal change in the absence of VEGF in buffer or in the absence of the estrodiole stimulus in cells.

6.1 INTRODUCTION

The cell is a basic unit of life that makes up complex living organism systems. At the cellular level, the microenvironment plays an important role in determining a cell's behavior and growth patterns. Thus, cellular behaviors in response to input stimuli can reflect the basic response of the organism. Furthermore, the cell-based bioassay is known as an important analytical technique in fundamental biology research, disease diagnosis, and advanced drug and therapeutic development.

In this section, an integrated platform is presented, which is applicable for the study of tumor metastasis by quantifying secretion pathway of the growth factors related to the metastasis. The platform could detect a cancer-related protein, vascular endothelial growth factor (VEGF) secreted from breast cancer cells by introducing a chemical stimulus, estrodiole in a culturing microfluidic device while monitoring the secretome with integrated sensors. Therefore, the platform is expected to be a useful tool to quantitatively understand the tumor metastasis-signaling pathway and discover drugs for cancer therapy.

6.2 PRINCIPLES

Significance of angiogenesis The primary cause of death for most cancer patients is metastatic disease, which invades foreign organs and disrupts important body processes necessary for survival.[1, 2] Certain mutations provide the tumor cells with redundant pathways to escape apoptosis, enhance survival in the bloodstream, and support progressive outgrowth at a distant site. Studying these pathways will provide more chances to identify promising molecular targets for cancer therapy. However, only part of the metastatic processes has been modeled and only the end stages of the metastatic process could be observed. Therefore, successfully understanding the early processes, such as angiogenesis and the effect of the microenvironment will provide opportunities for study on metastasic signaling pathways and, in turn, eventually clinical research.[3]

Significance of VEGF during angiogenesis Cancer metastases are commonly found in the lymphatic system and circulatory system because stimulation of tumor lymphangiogenesis and tumor blood angiogenesis require the interplay of several tumor-derived growth factors.[1,4,5] The recruited blood and lymph associated cells then secrete growth factors (secretome), which stimulate motility and invasion of tumors (Fig. 4.1). Multiple growth factors: vascular endothelial growth factor (VEGF), basic fibroblast growth factor (bFGF), platelet-derived growth factor (PDGF), and transforming growth factor (TGF-β) interrupt angiogenic dormancy, promote neovascularization, and enhance the proliferation of tumor cells. Thus, monitoring the level of these secreted growth factors will provide an approach to understand tumor metastasis[3]. Among them, VEGF is considered a key mediator of tumor angiogenesis, including neovascularization in human breast cancer.

VEGF stimulated by estrodiole Being endocrine-dependent carcinoma, the development of breast cancer necessitates hormones, in particular, estrogen and progesterone.[6] Estrogen mediates its activities through nuclear receptors, so-called ERs, which activate transcription and, hence, up-regulate expression of genes that are important for cell growth. Therefore, estrogen regulates angiogenesis in MCF7 tumors by maintaining VEGF at levels sufficient for the generation of functional microcapillaries and consequently facilitates tumor growth.

6.3 DESIGN

Microenvironment with Microfluidics The microfluidic platform provides a controlled physiological environment to culture cells and supply complex stimuli that mimic dynamic cellular microenvironments. This miniaturized environment not only enables systematic characterization of cell responses in a highly parallel way but also prevents human errors associated with repetitive tasks. Therefore, creating a microenvironment with microfluidics will be an attractive way for massively parallel integration of cell culture and stimulus control for quantitative biomedicine (Fig. 6.2).

In this case, cancer environment is simulated in the presence of high concentration of estrodiole, which induces the VEGF over-expression from breast cancer cells, MCF7. The secretion of VEGF is detected by monitoring signal change of an integrated VEGF aptasensor in the microfluidic. For the detail, the scattered light from the GNP can enhance fluorescent signals (SEF: surface enhanced fluorescence) within the LSPR (local surface plasmon resonace) region in the absence of a target molecule, VEGF. However, once the aptamer is bound to the target, a conformational change occurs, leading to the subsequent detachement from the GNP surface. Its removal from the LSPR region results in no SEF effect and a loss in overall fluorescence intensity. Therefore, the concentration of VEGF can be directly estimated by measuring the decrease of the fluorescence signal.[7]

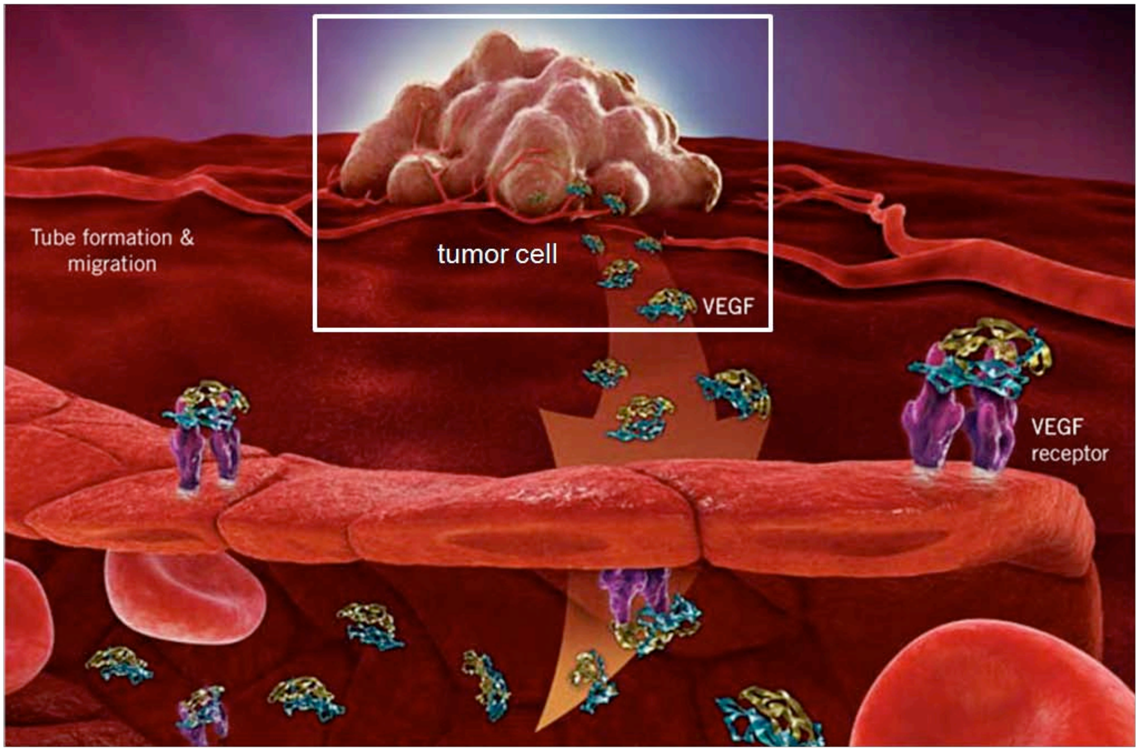

Figure 6.1 The process of angiogenesis is driven by the tumor's release of pro-angiogenic signals, such as VEGF. VEGF binds to receptors on the endothelial cells of nearby blood vessels stimulating mitogenesis and cell migration. The highlighted area indicates the growth factor secretion pathway that we want to quantify by mimicking the environment with microfluidics and monitoring the level of growth factors with integrated sensors. (Courtesy of Genentech Inc.).

Fabrication of Microfluidics An aptasensor substrate and a microfluidic channel are fabricated separately and then bonded together (Fig. 6.3). The aptasensor is prepared by fixing 80 nm GNPs (gold nanoparticles) on an APS (amino silane) coated glass slide and then additionally coating PLL (poly-L-lysine) on the GNPs. The microfluidic channel is fabricated by replicating SU-8 mold structure with PDMS, which is fabricated by a standard lithographic technique and then coated with bovine serum albumin (BSA) to avoid the non-specific binding of aptamer and VEGF to the PDMS channel. The aptasensor substrate and PDMS channel are treated with UV-ozone for 3 minutes and contact immediately for irreversible bonding. The aptamer-Cy3 complex is introduced to be immobilized on the PLL-coated GNP surface by an electrostatic force.

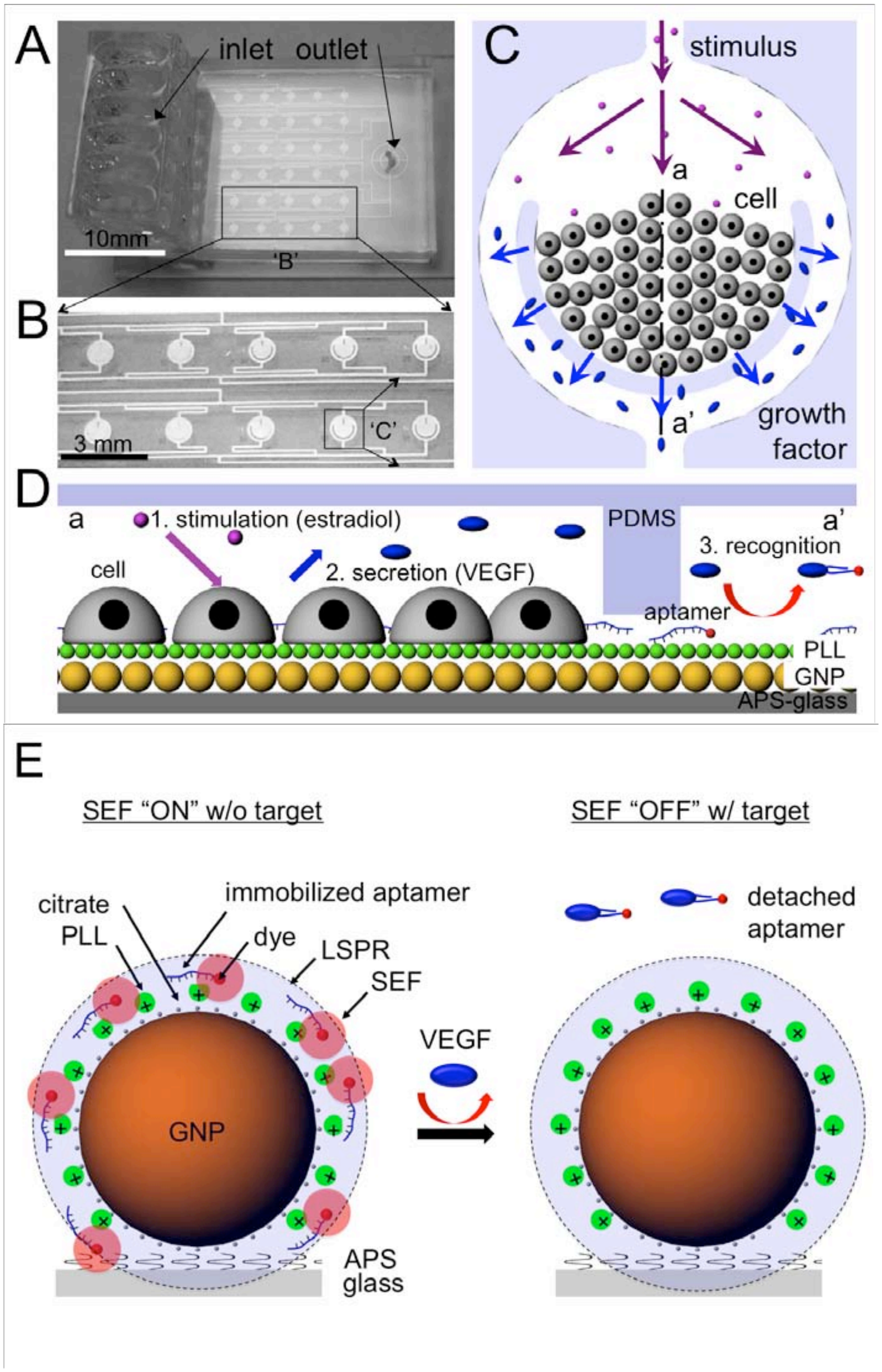

Figure 6.2 Schematics of an integrated platform. A and B provides photos of a fabricated microfluidic platform, and C and D illustrate a top and a cross-sectional view of an integrated chamber, respectively. E shows its detection scheme. When a VEGF-expression stimulus is added to the media, it induces over-expression of VEGF secretion by MCF-7 cells into the surrounding media. The secreted VEGF is captured by a VEGF-specific aptamer, which then detaches from the surface of the gold nanoparticles. The detachment is monitored by measuring the change in florescence signal from the culture chamber.

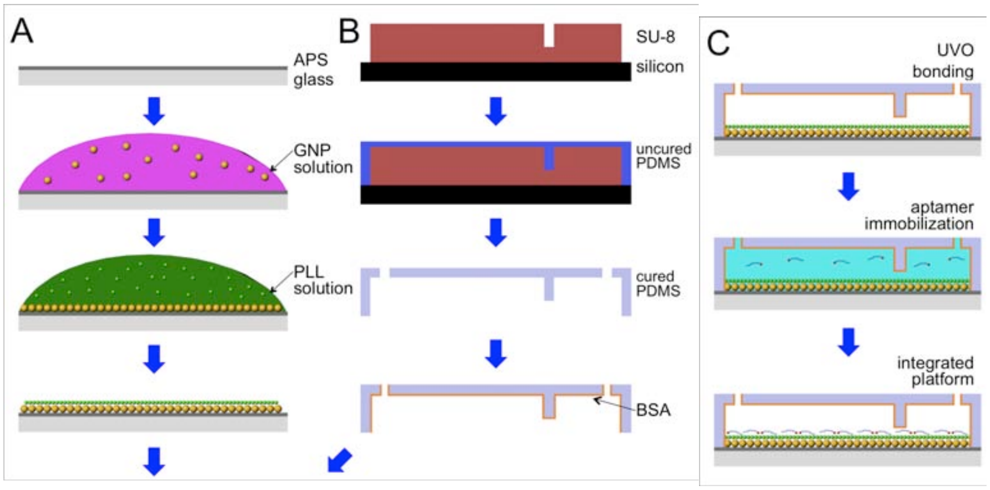

Figure 6.3 Fabrication steps of the integrated microfluidic platform. A. APS, GNP, and PLL are sequentially immobilized on a glass surface. B. Microfludic device is fabricated by replicating stucture made of SU-8 on a wafer using PDMS. C. After UVO treatment for assembly with 5% w/v BSA-coated microfluidics, aptamer is immobilized on the glass surface

6.4 CHARACTERIZATION

Simulation Cellular trapping and the distribution of stimulus/secreted growth factor were numerically confirmed (Fig. 6.4). Introduced cells flow along with pathlines and trapped by a C-shape blocking wall having a 2 μm gap underneath in an isolated chamber (Fig. 6.4A). However, perfused stimulus can enter into the chamber through streamlines, which pass through the wall and secreted VEGF from trapped cells are diffused out through the gap (Fig. 6.4B).

Kinetics and sensitivity Figure 6.5 showed the detection of VEGF at 100 nM within 30 min with a limit of detection of 1 nM in aptamer buffer solution. Fig. 6.5A compares a bright field image (left upper) and fluorescence images.

Detection of secreted VEGF from cells Over the entire experimental duration, a media (+10% FBS, 0.1mM estrodiol) was perfused at the flow rate of 0.5 µL/min. The fluorescence signals were measured every 12 hours. Figure 4.6 shows that the integrated platform could monitor VEGF present in culturing media containing 10% FBS and detect additional VEGF secreted from MCF-7 cells stimulated by 0.1 mM estrodiole during culturing up to 37 hrs. Fig. 6.6A compares a bright field image (left upper) and fluorescence images.

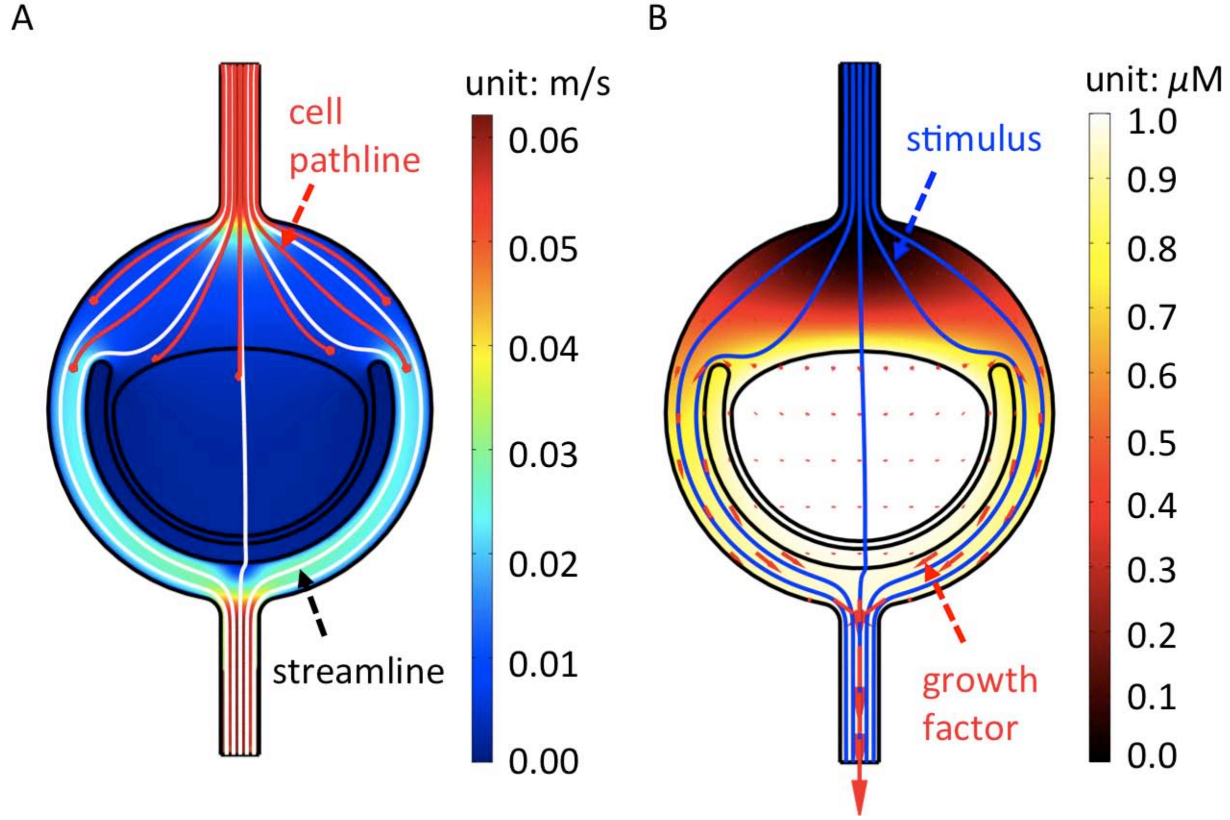

Figure 6.4 Simulation of cell trapping and secretome distribution. (A) Cells are introduced along pathlines and captured in the C-shape chamber. **(B)** Stimulus is introduced along streamline and growth factors are diffused out from the chambers.

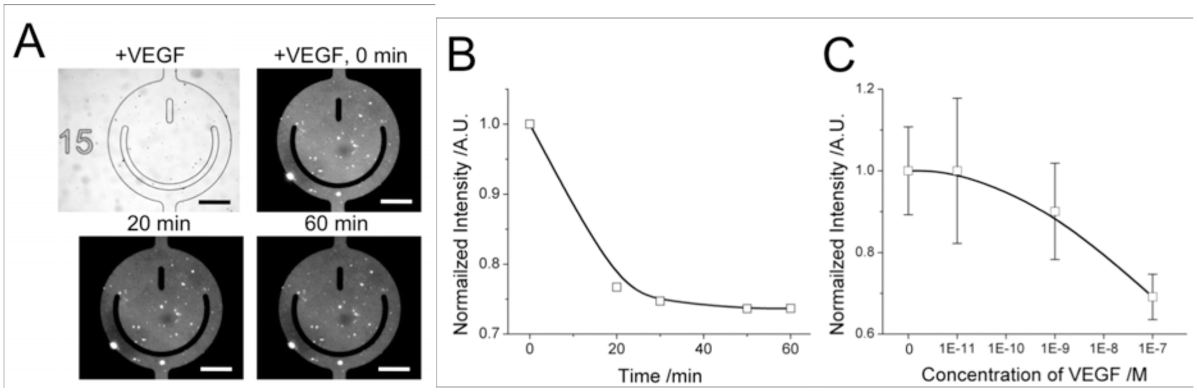

Figure 6.5 Kinetics and sensitivity of VEGF detection. A/B. The signal decrease was observed with time and then saturated at about a half hour in the case of 100 nM VEGF. C. Observed limit-of-detection for VEGF in buffer is 1 nM after an hour following the addition of VEGF. Scale bars are 500 μm.

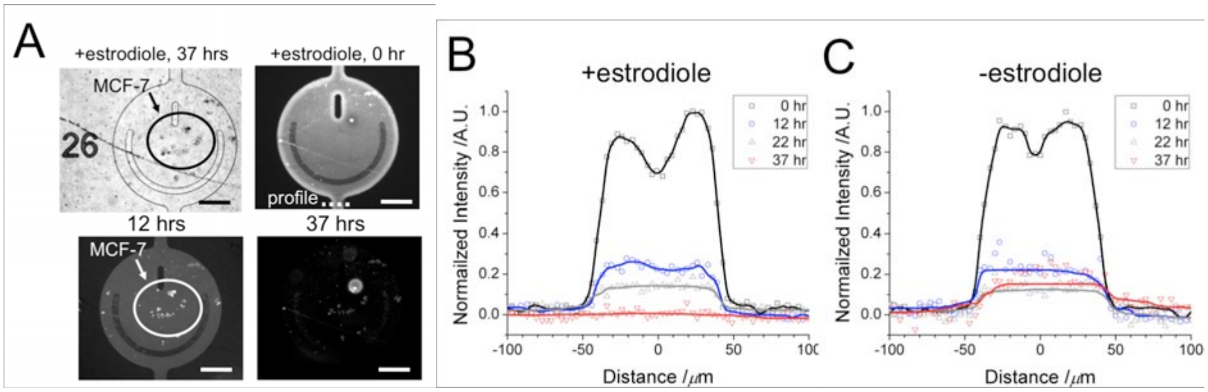

Figure 6.6 VEGF detection from MCF-7 cells under chemical stimulation. A and B. Signal intensity decreases to background levels when cells are stimulated by a continuous dose of 0.1 mM estrodiole for 37 hrs. C. In the absence of estradiol, signal remained significantly above backround levels. Scale bars are 500 µm.

6.5 CONCLUSIONS

Here we demonstrated development of a totally integrated platform for cancer research. So far, the platform has successfully demonstrated by detection of VEGF down to 1 nM within 1 hour. Also, we have demonstrated detection of VEGF secretion by estrodiole-stimulated MCF-7 cells.

References:

(1) Steeg, P. S., Tumor metastasis: mechanistic insights and clinical challenges, *Nature Medicine* **2006**, 12, 895-904.
(2) Aguirre-Ghiso, J. A., Models, mechanisms and clinical evidence for cancer dormancy, *Nature Reviews Cancer* **2007**, 7, 834-846.
(3) Sebolt-Leopold, J. S., English, J. M., Mechanisms of drug inhibition of signaling molecules, *Nature* **2006**, 441, 457-462.
(4) Duchek, P., Guidance of cell migration by the drosophila PDGF/VEGF receptor, *Cell* **2001**, 107, 17-26.
(5) Cao, Renhai *et al.,* PDGF-BB induces intratumoral lymphangiogenesis and promotes lymphatic metastasis, *Cancer Cell* **2004**, 6, 333-345.
(6) Bogin, L., Degani, H., Hormonal Regulation of VEGF in Orthotopic MCF7 Human Breast Cancer, *Cancer Research* **2002**, 62, 1948-1951.
(7) Liotta, L. A., Kohn E. C., The microenvironment of the tumour–host interface, *Nature* **2001**, 411, 375-379.

CHAPTER 7:
CONCLUSIONS AND FUTURE DIRECTION

7.1 CONCLUSIONS

In this dissertation, the novel building blocks for microsystem were presented.

Inspired by xylems in plant systems, microfludic diodes were systematically analyzed theoretically and experimentally. The functionality was shown by patterning droplets spontaneously in a large-scale microfluidic circuit and patterning two different cell lines in a 3D cell culturing microfluidic platform for the study on cell communication.

Inspired by target recognition in nature, aptamer-based nanoplasmonic sensors were presented by detecting a coagulation protein, human α-thrombin. The benefits of the aptamer sensor were demonstrated by detecting one of the most prodominent cancer markers, $VEGF_{165}$ and showing the higher level of measurement in serum from breast cancer patients.

The potential of the integration of a microfluidic platform and a nanobiosensor was shown by developing an integrated cell-culturing platform of breast cancer cells with $VEGF_{165}$ aptasensor.

7.2 FUTURE WORK

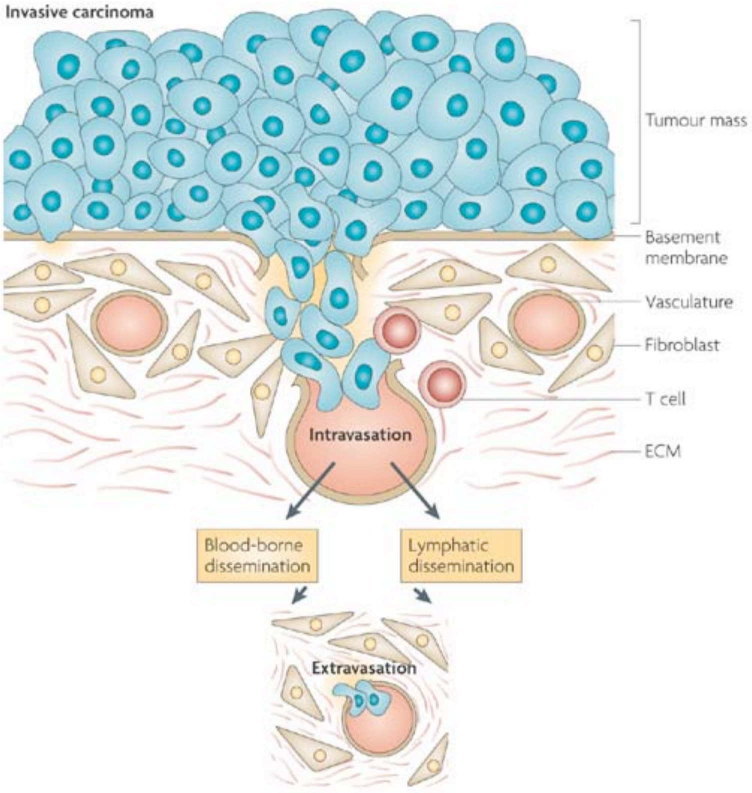

Figure 7.1 Progression of tumor metastasis.[1]

Tumor metastasis Metastatic cellular pathway is composed of series of multistep: the migration of individual tumor cells from a primary tumor in ECM, intravasation through endothelial cells, circulation in blood stream, extravasation at the secondary site, and growing at new sites (Fig. 7.1).[1-5] The steps are experimentally or theoretically studied, respectively. For example, the tumor migration is correlated with ECM, proteins, growth factors, and cytokines. Also, invasion involves tumor cell's adherence to cells and ECM, degradation of surrounding tissue, and the motility of tumor cells through the tissue. However, the experimental study in human is realized only at the end stage of the processes due to the complexity of monitoring until a lesion becomes large enough for imaging.

Co-culturing microfluidic platform for metastasis Developed microfluidic platform has the potentials of providing biologically relevant ex vivo cellular environments along with regulated stimuli for quantitative study on the metastasis. The tumor migration study can be analyzed under variation of the ECM properties: stiffness, porosity, and its composition. The invasion (intravasation and extravasation) can be systematically monitored with variation of endothelial cells: cellular density, number of layers, and kinds. It is further expected that the microfluidics can be integrated with aptamer-based sensor by combining with surface Plasmon-effective nanostructures, which allows monitoring the progression in real time.

References:

(1) Aguirre-Ghiso, J. A., Models, mechanisms and clinical evidence for cancer dormancy, *Nature Reviews Cancer* **2007***,* 7, 834-846.

(2) Steeg, P. S., Tumor metastasis: mechanistic insights and clinical challenges, *Nature Medicine* **2006**, 12, 895-904.

(3) Deryugina, E. I., Quigley, J. P., Matrix metalloproteinases and tumor metastasis, *Cancer Metastasis Rev* **2006**, 25, 9–34.

(4) Naora, H., Montell, D. J., Ovarian Cancer Metastasis: Integrating insights from disparate model organisms, *Nature Reviews Cancer* **2005**, 5, 355-366.

(5) Duchek, P., Somogyi, K., Jekely, G., Beccari, S., Rorth, P., Guidance of Cell Migration by the Drosophila PDGF/VEGF Receptor, *Cell* **2001**, 107, 17-26.